THE PROCEEDINGS OF
THE PHYSICAL SOCIETY

Section B

VOL. 64, PART 4 1 April 1951 No. 376 B

The Role of Convergence in Stereoscopic Vision

BY W. D. WRIGHT

Technical Optics Section, Imperial College, London

Read before the Optical Group, 25th January 1950; *MS. received* 12*th October* 1950

ABSTRACT. An apparatus for testing stereoscopic acuity has been constructed in which the distance of a reference aperture P is compared with that of a test aperture Q selected from one of a tapering series of aperture plates. The apertures are seen as illuminated discs in a black field and all monocular aids to depth perception are eliminated. The observer has to state whether Q is in front or behind P, and the acuity is derived by plotting the percentage estimates against the distance of Q. Observations have been made for condition A, in which the observer is allowed to look first at P and then at Q, and for condition B, in which the observer fixates on P and views Q extra-foveally. From a comparison of the acuity for the two conditions for various angular separations θ between P and Q, deductions can be made about the relative contributions to stereoscopic vision of convergence and retinal disparity. The results suggest that convergence makes a significant contribution and has become the predominant factor at $\theta=20°$. For $\theta=14°$, the acuity for condition A is due entirely to convergence, since the blind spot interferes with the retinal disparity. Tests with flash exposures suggest that small eye movements do not play any important part in depth perception. The presence of depth perception under conditions of gross diplopia was confirmed, indicating that fusion is not an essential item for three-dimensional vision.

§ 1. INTRODUCTION

VARIOUS theories of depth perception have been proposed from time to time and, in common with other aspects of vision, their popularity has waxed and waned. The theories have not necessarily been mutually exclusive, since it is apparent that a number of factors can contribute to three-dimensional vision, yet sometimes one, sometimes another, has been regarded as pre-eminent. Dispute has chiefly centred on the relative importance of convergence and retinal disparity. Some authorities (for instance, Javal 1866) have held that convergence was the primary factor, a near object being recognized as such through the influence of the extra-ocular muscles as they were tensed to converge the eyes on to the object; for distant objects, the visual axes are more nearly parallel and the muscles relaxed. Brücke (1841) considered that the perception of depth arose from foveal viewing and fusion of successive points round the contours of an object. The view generally held at the present time is that retinal disparity makes the main contribution. Since the right and left eyes view a scene from slightly different positions, the images on the two retinae have slightly different geometrical configurations, that is, there will be retinal disparity. The mental fusion of these dissimilar images is then assumed to evoke the sense of depth (see, for example, Duke-Elder 1932, p. 1064).

The evidence which is generally used to clinch the disparity argument is derived from tests on stereoscopic acuity under flash illuminations (for example, Langlands 1926, 1929). Doubts about the interpretation of Langlands' results, however, have been expressed (Wright 1948), and certainly in the case of extra-foveal vision, Langlands found no stereoscopic acuity under flash illuminations. Yet an excellent sense of depth can be appreciated between objects widely separated across the field of view, and it seems reasonable to suppose that this must largely result from the successive foveal convergence on the individual objects, since the poor resolving power of the peripheral retina makes it unlikely that retinal disparity in the outer parts of the field can make a very effective contribution to depth perception.

When stereoscopic vision was discussed in 1948 at the Optical Convention organized by the Spectacle Makers Company, the need for fresh experiments to provide a more decisive test of the relative contributions of convergence and disparity was apparent. The matter is not merely of academic interest but has a practical bearing in connection with certain aspects of orthoptic training, and with problems of space perception under abnormal conditions, for example when the observer or the target is moving at high velocity, when the illumination level is low, etc. The Spectacle Makers Convention has thus provided the stimulus for the present work.

§ 2. APPARATUS

In ordinary seeing, there are a number of subsidiary aids to the judgment of distance, such as size, perspective, parallax, etc., in addition to those derived from binocular vision. For the purpose of the present experiments, these aids had to be eliminated, and it was eventually arranged that the two objects whose distance was to be compared should consist of two illuminated, circular apertures seen against a black surround in a dark room. No structure of the surround could be resolved by the observer, hence he could gain no assistance in his judgment from the distance of the apertures relative to the background. This condition is difficult to satisfy except in tests with bright objects in a dark room, but this solution does impose some limitation on the state of adaptation under which the test can be applied.

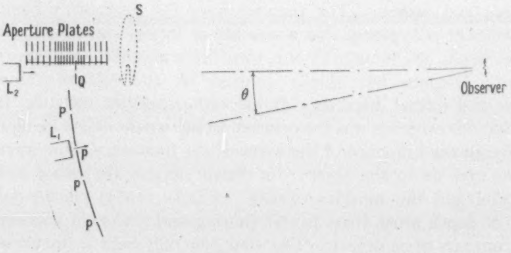

Figure 1. Experimental arrangement for testing stereoscopic acuity.

The reference object was provided by any one of four apertures P, Figure 1, located on an arc at a distance of 6 ft. from the observer. The test aperture Q was provided by any one of a battery of aperture plates mounted along a spindle so that they could be swung into position in front of an illuminated diffusing screen L_2. The apertures were spaced 1 in. apart over a distance of 14 in., except that intermediate plates at $\frac{1}{2}$ in. spacing were included in the central 5 in. The apertures formed a tapering series such that they all subtended the same angle (approximately 25 minutes of arc) when viewed by an observer 6 ft. from the mid-aperture. The illuminated screen at the far end of the apertures provided a structureless area of light, against which Q appeared as a uniform disc of light defined only by its bounding edge.

The observer's head was located and fixed by biting on a dental impression mounting which could be adjusted vertically and laterally. His head was positioned so that the point mid-way between his eyes was in alignment with the axis formed by the Q apertures when swung into their observing positions. This could be judged from the foreshortened appearance seen by each eye when the two extreme Q apertures were in position simultaneously. The angular separation θ between the Q axis and the four P apertures was 5°, 10°, 14° and 20° respectively. The P aperture selected for any particular experiment was illuminated by a light box and diffusing screen L_1, placed immediately behind it; the diameter of the P apertures was 7/16 in. thus having the same angular subtense of 25 minutes as the Q aperture.

The light sources in the two light boxes were 4-v. lamps whose intensity was controlled by a rheostat and voltmeter. The luminance of the apertures could be adjusted to suit the observer, but in most of the experiments it had a value of about 1·5 candles/ft^2. Flash exposure of the Q apertures could be arranged by introducing a rotating sector at S. The sector was mounted on a gramophone motor with its axis on the same horizontal level as the Q apertures and the observer's eyes; this ensured that the light into the two eyes was intercepted simultaneously.

It was considered that with the arrangements described, all monocular aids to distance perception other than accommodation had been eliminated. To confirm this, tests were made using one eye only (in this case the observing eye itself was brought into alignment with the Q axis), and no distance perception was found to exist over the range of 14 in. that could be studied with the apparatus. This also confirmed that accommodation was a negligible factor in the observations.

§ 3. METHOD OF OBSERVATION

The task of the observer was to state whether, for the particular conditions of the experiment, the aperture Q introduced by the operator appeared in front (plus), or behind (minus), the comparison aperture P. The reply was recorded by the operator in the column appropriate for that aperture, a new aperture was introduced and the observation repeated. A rapid sequence of observations could be maintained as the apertures were swung in in random order until 25 replies had been recorded for each aperture used. Only a few of the apertures were required in any given experiment, the range and spacing to be covered depending on the distance sensitivity under the conditions of the experiment, as determined by a few trial observations. The percentage of plus and minus replies at each distance was then calculated and plotted against the distance. If the aperture Q appeared to be level with P, the observer was not allowed to state this, but had to make a guess of plus or minus. The level position was then, at least in theory, indicated by a 50% plus, 50% minus, estimate.

Two conditions of observation, A and B, were employed. In condition A, the observer looked first at P and then at Q, so that both convergence and disparity contributed to his depth perception. The observer was asked to try to transfer his gaze from P to Q in one fixation jump, and certainly without any fixation pauses midway between P and Q. Eye movement studies (Lord and Wright 1949) suggest that in a quick movement, it is fairly easy to traverse most of the gap between two fixation targets in one jump, although a small residual correction may sometimes be necessary to complete the fixation on the new target. Ideally, the observer made his judgment of Q after a single switch from P to Q and he was definitely discouraged from looking backwards and forwards several times, otherwise the risk of a fixation pause between P and Q would have been too great.

In condition B, P was fixated continuously and the position of Q had to be judged solely by extra-foveal vision. Convergence thus played no part and, since the disparity contributions to depth perception were the same for the A and B conditions provided the observer made no intermediate fixation pauses in the A observation, any contribution to the stereoscopic sense from convergence changes would be revealed by an enhancement of the stereoscopic acuity for condition A. The results for the various angles θ enabled the relative contributions of convergence and disparity to be studied for increasing angular separations of the test objects.

At $\theta = 14^\circ$, however, a special situation arises since, when P is fixated, Q is imaged on the blind spot of the right eye, while when Q is fixated, P falls on the blind spot of the left eye. There is thus no possibility of retinal disparity making any contribution to the stereoscopic acuity, hence for condition A the acuity is due solely to the convergence factor, while for condition B, observation of Q reduces effectively to one-eyed vision. This value of θ was therefore chosen deliberately as a device to separate the convergence and disparity factors.

Tests on the flash acuity were restricted to condition B. Aperture P was fixated and seen continuously, and the observer was required to judge the position of Q as seen by extra-foveal viewing during one, or at most two, flash exposures.

§ 4. RESULTS AND DISCUSSION

Typical results are shown in Figure 2, in which the percentage estimates are plotted against the position of the Q apertures for A and B observations at $\theta = 10^\circ$.

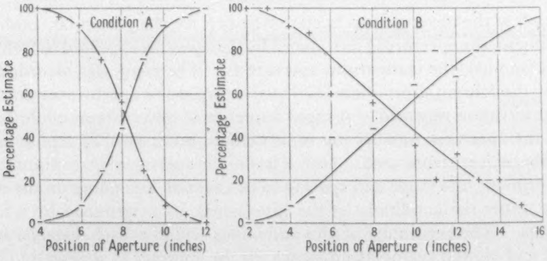

Figure 2. Stereoscopic acuity curves for $\theta = 10^\circ$. Percentage estimates of location of aperture plotted against aperture position for conditions A and B.
+ test aperture reported in front of reference aperture.
— test aperture reported behind reference aperture. Observer: W. D. W.

Curves as smooth as those in Figure 2, A, were quite common, but under conditions where the acuity was poor, as in Figure 2, B, the points were sometimes more irregular. Some 150 or 200 observations were required for each curve, but the apparatus could be operated so quickly that these could be recorded in 15 or 20 minutes. More extended observations, which might have been justified on statistical grounds, were undesirable visually if fatigue were to be avoided.

One method of specifying the stereoscopic acuity from the percentage curves would have been to give the displacement of the apertures necessary to pass from a 50% to, say, an 80% estimate. This might correspond to the displacement needed for the aperture Q to be just noticeably in front or behind P. A measure which is in some ways to be preferred is obtained from the slopes of the curves at the 50% level, as measured by the percentage change per inch, since this gives a very direct indication of the sensitivity of the observer to change in distance of Q. Using the latter measure, Figure 3 shows the variation of the acuity with θ for both conditions A and B and for a number of repeat experiments. While the slope of the percentage curves should be regarded as measuring the acuity, it has been convenient in Figure 3 to use a logarithmic scale, since this gives a better idea of the spread of the observations. The spread is in fact fairly considerable, as must be expected from the nature of the observations.

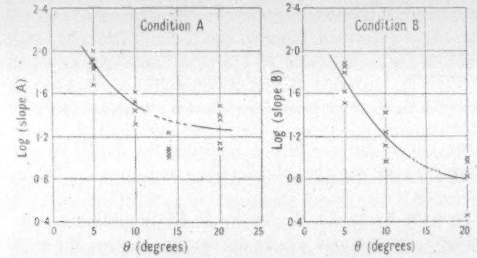

Figure 3. Variation of stereoscopic acuity with θ. Acuity measured by slope of percentage estimate curves. Log (slope) plotted against θ, for conditions A and B. Observer: W. D. W.

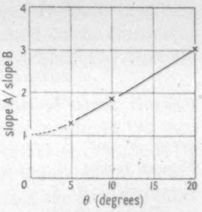

Figure 4. Comparison of stereoscopic acuity for conditions A and B at different values of θ. Slope A/Slope B plotted against θ.
Observer: W. D. W.

At $\theta = 14°$, the slope was zero for condition B, since the observation was effectively monocular; this is indicated by a break in the curve. A discontinuity is also shown in the A curve because, while observations could still be made, the judgment had a different basis from that at the other three positions.

Both the A and B curves show a decrease in the stereoscopic acuity with increase in θ. The decrease is more severe for condition B, no doubt because, for this condition, depth perception is more directly dependent on the resolving power of the peripheral retina.

Some stereoscopic acuity could be recorded for condition A at $\theta = 14°$, and it would seem that this must be attributed to the convergence factor. The average slope value lies about 0·3 log units below the dotted portion of the curve, so that the stereoscopic acuity as measured by the slope is roughly halved by the removal of the disparity factor. It might then be deduced that, in the absence of the blind spot, convergence and disparity would make approximately equal contributions to the acuity at $\theta = 14°$.

This can also be seen from Figure 4, in which the ratio of slope A to slope B has been plotted against θ. Except at $\theta = 0°$, slope A is always greater than slope B, indicating that convergence is always making a significant contribution to the acuity and, since the ratio increases with θ, it would seem that convergence becomes steadily more important the greater the lateral separation of the objects, until at $\theta = 20°$ it has become the dominant factor. The extrapolation of the curve to show a slope ratio of 1·0 at $\theta = 0°$ is reasonable, since as the targets approach very close to each other, conditions A and B become virtually identical.

The results shown so far have all been recorded by the author, who has repeated each set of observations some four or five times. Two other observers have also made a single complete series of experiments, giving results of the same general character, although differing in absolute sensitivity. Thus Figure 5 gives A and B percentage curves for $\theta = 20°$ as recorded by R. N. W. and Figure 6 the A percentage curves for the blind spot condition, $\theta = 14°$, as recorded by E. T.

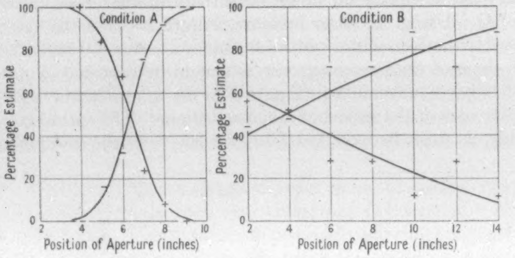

Figure 5. Stereoscopic acuity curves for $\theta = 20°$, for conditions A and B. Observer: R. N. W.

Flash acuity tests were made by W. D. W. for $\theta = 5°$ for condition B only. The main purpose of the flash observations was to determine whether the small eye movements that may occur during apparently steady fixation make any important contribution to fusion and depth perception, on the lines suggested by Marshall and Talbot (1942). As shown in Figure 7, no significant deterioration in stereoscopic acuity occurred for the flash condition, and this result was confirmed for flash durations between 0·10 sec. and 0·01 sec. This conclusion is in apparent disagreement with Langlands' results, but in the present

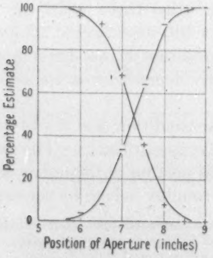

Figure 6. Stereoscopic acuity curves for $\theta = 14°$, blind-spot angle; condition A. Observer: E. T.

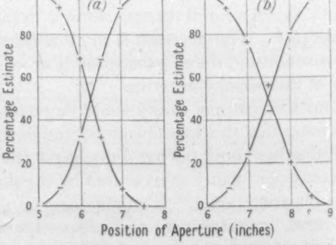

Figure 7. Stereoscopic acuity curves for $\theta = 5°$, for condition B, (a) with continuous illumination and (b) for flash exposure. Duration of flash 0·02 sec. Observer: W. D. W.

experiments the reference aperture P was being fixated all the time and this, no doubt, made the observer's task easier. Nevertheless, the present arrangement appears to provide a legitimate test of the part played by small eye movements in the development of the retinal disparity contribution. The absence of any deterioration under flash conditions suggests that eye movements are not necessary to produce fusion of disparate retinal images and do not enhance stereoscopic perception.

One effect experienced by W. D. W. during the blind spot experiment should be put on record. After a few minutes' observation, the ability to locate the distance of Q relative to P sometimes disappeared almost completely, but after a minute or two's rest, including looking round the room, depth perception was restored. Possibly some adaptation process occurs in the sensory fibres of the extra-ocular muscles, but the effect at least confirms that the depth perception recorded was not an artefact arising from fixation pauses intermediate between P and Q.

§ 5. DEPTH PERCEPTION IN DIPLOPIA

Discussions on stereoscopic vision in terms of the retinal disparity theory generally seem to imply that fusion is an integral part of the depth perception. Yet experiments have been reported (Auerbach and v. Kries 1877, Tschermak and Höfer 1903) in which it was claimed that fusion is not required for the creation of the depth sensation; a spark, for example, seen as a double image could be correctly located in front or behind a reference object.

Under ordinary conditions of seeing it is almost impossible to test whether crossed diplopia can be distinguished from uncrossed diplopia without the subsidiary clues of parallax, perspective, etc., which nearly always exist, or without the assistance of momentary changes in convergence which affect the amount of crossed and uncrossed diplopia in opposite directions. Nevertheless, the possibility that the two types of diplopia can be distinguished in their own right, as it were, through their influence on depth perception, seemed so remarkable and so fundamental to an adequate theory of stereoscopic vision, that it seemed worth while to extend the present experiments to confirm this claim.

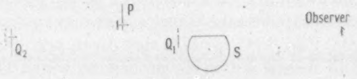

(a) Side Elevation

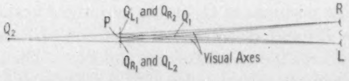

(b) Plan

Figure 8. Arrangement for testing depth perception in the presence of diplopia. (*a*) Side elevation. (*b*) Plan, showing location of double images.

For this purpose, the apparatus illustrated in side elevation in Figure 8(*a*) was constructed. An illuminated reference aperture P was located at a distance of 2 ft. 8 in. from the observer and $1\frac{1}{4}$ in. vertically above the line of the test apertures Q_1 and Q_2. Q_1 and Q_2 were located at a distance of 2 ft. and 4 ft. respectively from the observer, but any one of five apertures of different sizes could be inserted at either Q_1 or Q_2. The angular subtense of P at the observer's eye was about 27 minutes of arc, while the Q apertures subtended angles ranging from 18 minutes to 36 minutes. No attempt was thus made to maintain a constant apparent size of the Q apertures; instead, size was eliminated as a factor by having both small and large apertures at both the nearer and farther positions.

In the experiment, P was fixated continuously, but Q_1 and Q_2 were only seen momentarily and for a single flash as the sector S rotated. This sector consisted of a cylindrical drum with a flat segment, which exposed the Q aperture when the segment crossed the line of sight. Suitable screening was provided so that, as before, the observer saw only the illuminated apertures in a black field. When the operator introduced either aperture Q_1 or Q_2 in random sequence both of size and distance, the observer had merely to indicate whether the aperture he saw in a single flash was the one in front or behind P.

From the plan view of the arrangement in Figure 8(*b*), it is evident that when Q_1 is introduced, it will be seen as a double image projected at Q_{R_1} (right eye) and Q_{L_1} (left eye) in the plane through P. When Q_2 is introduced, the corresponding double images will be projected at Q_{R_2} and Q_{L_2}. From the dimensions of the system, Q_{R_1} will be coincident with Q_{L_2}, and Q_{L_1} with Q_{R_2}, so that the visual patterns are identical whether Q_1 or Q_2 is inserted. Since the apparent angle separating the double images was about $1\frac{1}{2}°$ and they were viewed only about 2° below the fovea, fusion was manifestly impossible; the short duration flash (about 0·02 sec.) prevented convergence changes giving any clue as to whether Q_1 or Q_2 had been inserted; the observer's head was fixed, hence parallax effects were eliminated; and no subsidiary aids from perspective, shadows, size, etc., were present. Yet the observer never had the slightest difficulty in deciding whether Q was in front or behind P and indeed the double image was seen clearly projected in front of, or lying behind, P with a true three-dimensional effect.

Evidently, therefore, fusion is not an essential item in depth perception. While the observer cannot consciously tell which eye is seeing which of the double images (a matter of considerable interest and referred to by many writers, e.g. Helmholtz 1866, English translation 1925 p. 458) the information must nevertheless be available to the brain and be utilized to give the position of the object in space. The experiment supports the theory sometimes encountered in the literature (see, for example, Carr 1935, p. 223) that depth perception, in part at least, results from a kind of mental surveying process in which Q_1 is located at the intersection of the lines RQ_{R_1} and LQ_{L_1} (Figure 8(*b*)) mentally projected from the right and left eyes to their respective disparate images, and Q_2 at the intersection of RQ_{R_2} and LQ_{L_2}. The positions of Q_1 and Q_2 as judged in this way would clearly have to be related in absolute distance to the position of P as determined by the convergence angle between the visual axes PR and PL. The theory could then be integrated very satisfactorily with the idea of convergence as a significant factor in depth perception.

§ 6. CONCLUSION

Certain fairly definite conclusions emerge from these experiments:

(i) The condition B observations indicate that retinal disparity, accompanied by fusion, contributes to a sense of depth.

(ii) The diplopia experiments indicate that retinal disparity, even in an extreme form unaccompanied by fusion, contributes to a sense of depth.

(iii) Whether fusion as such makes a contribution to stereopsis additional to that arising from the disparity itself cannot be decided from the present experiments. No doubt arguments for and against this possibility could be advanced.

(iv) The flash experiments indicate that small eye movements are not a necessary item for fusion and do not enhance depth perception.

(v) The blind spot experiments suggest that convergence by itself is an important factor in stereoscopic acuity.

(vi) The relative values of stereoscopic acuity for conditions A and B at various separations of the targets suggest that convergence and disparity both contribute to the stereoscopic sense, and that the wider the field of view, the more important does the convergence factor become.

Reference has been made at one or two points in this paper to the need to eliminate from the experiments subsidiary clues such as parallax, perspective, size, etc. This elimination was necessary to reduce the number of variables in the experiment, but there is no suggestion that these aids are not genuine factors in three-dimensional vision. It may well be true that the sensation of depth was first acquired through binocular perception, but, either by association or otherwise, the monocular factors have come to be important items as well, and can by themselves give rise to three-dimensional seeing. Under ordinary conditions of viewing, stereoscopic vision is therefore the result of a mental analysis and synthesis of a quite complicated array of visual data.

ACKNOWLEDGMENTS

The author wishes to acknowledge the help of Miss G. M. Frowde in recording his observations and for general assistance with the experiments, and to thank Miss E. Tadros and Mr. R. N. Wilson for acting as observers. Thanks are also due to the Medical Research Council for their continued financial support.

REFERENCES

AUERBACH, F., and v. KRIES, J., 1877, *Arch. Anat. Physiol., Physiol. Abt.*, 297.

BRÜCKE, E., 1841, *Müllers Arch. Anat. Physiol.* (Berlin: Veit), p. 459.

CARR, H. A., 1935, *An Introduction to Space Perception* (London : Longmans Green).

DUKE-ELDER, W. S., 1932, *Textbook of Ophthalmology*, Vol. I (London : Kimpton).

HELMHOLTZ, H., 1866, *Handb. d. Physiologischen Optik*, Vol. III; English translation, 1925, *Physiological Optics*, Vol. III, translated by J. P. C. Southall (New York : Optical Society of America).

JAVAL, E., 1866, in de Wecker's *Traité des maladies des yeux* (Paris: Delahoye).

LANGLANDS, N. M. S., 1926, *Trans. Opt. Soc., Lond.*, **28,** 45; 1929, *Med. Res. Counc., Spec. Rep. Ser.*, No. 133.

LORD, M. P., and WRIGHT, W. D., 1949, *Nature, Lond.*, **163,** 803.

MARSHALL, W. H., and TALBOT, S. A., 1942, *Biological Symposia*, Vol. III, *Visual Mechanism* (Lancaster, U.S.A. : Cattell Press).

TSCHERMAK, A., and HÖFER, P., 1903, *Arch. ges. Physiol.*, **98,** 299.

WRIGHT, W. D., 1948, *Trans. Opt. Conv. Worsh. Comp. Spect. Makers* (London: Hatton Press), p. 58.

Penetration by High-Velocity ('Munroe') Jets: I

By D. C. PACK* and W. M. EVANS
Armament Research Establishment, Fort Halstead, Kent

Communicated by N. F. Mott; MS. received 19*th July* 1950,
and in amended form 10*th November* 1950

ABSTRACT. By means of certain simplifying assumptions a formula is developed for the penetration into a ductile target by a high-velocity (' Munroe ') jet. The action of the jet is divided into two stages, each making its contribution to the total penetration. In the first stage a hole is formed by the lateral compression of the target as the jet penetrates it; the second stage begins when the last particle of the jet has ceased to act, the hole continuing to deepen until the residual energy in the target has been spent. At the high pressures set up by a Munroe jet the strength of the target plays only a subsidiary part in the phenomenon.

§ 1. INTRODUCTION

EXPERIMENTS were carried out by Munroe (1888) in which gelatinous cartridges, each with a conical indentation in the end, were placed against a steel target and exploded. It was observed that these cartridges produced indentations in the target which were similar in form to those in the original cartridge. The discovery was not entirely new; at the end of the eighteenth century it had been known that the existence of a hollow in the forward end of a blasting charge led to an enhancement of the explosive effect along the axis. The 'hollow charge' was used to some extent in mining in Europe during the early part of the nineteenth century, but it appears to have fallen into disuse, and Munroe's later work led to little research of interest until recent years.

Payman and Woodhead (1937) showed the importance of solid particles, carried in the detonation products, in producing and prolonging the intense 'end effects'. It is now known that these effects become even more remarkable when the indentation or hollow is lined with material; a pronounced jet is formed, and the stream of material from the lining which acts as the penetrating agent has been called the 'Munroe jet'. A considerable amount of pioneer research on phenomena associated with the detonation of an explosive charge with a lined hollow at the end away from the detonator was carried out by Evans and Ubbelohde (1950 a, b). A general summary of work on the formation of Munroe jets has been given in a paper by Birkhoff, MacDougall, Pugh and Taylor (1948). Experiments have provided valuable information concerning the behaviour of the Munroe jet, but many questions on the origin and manner of action of the jet remain unanswered.

The purpose of the present paper is to investigate, from a theoretical point of view, the penetration by Munroe jets into solid targets. The mechanism of formation of the jet will not be discussed. It has been necessary to make some very sweeping simplifications and approximations in the formulation and solution of the problem, but it should be borne in mind that formulae which give only approximate answers may be of great assistance in practical work: it is well known by experimental workers that explosive charges made carefully to the same specifications and from the same materials usually give results which exhibit an appreciable amount of scatter.

---

* Now at University College, Dundee, University of St. Andrews.

Since the measurement of the actual physical conditions in a jet, even when possible, is a difficult experimental task, the object of the theoretical work has been to express results in such a form that the performance of a jet against different combinations of targets may be calculated from the values of certain parameters of the jet, these parameters being easily determined from the results of an initial small number of simple firings. This application will be discussed in a later paper.

§ 2. DEPTH OF PENETRATION

Evans and Ubbelohde (1950 b) measured the velocity of the jet from hollow charges lined with metal. The velocity of the head of the jet is of the order of 10,000 feet per second, so that the pressure exerted by the jet, on any material which it penetrates, must normally be large compared with the plastic yield stress of the material. It follows that the velocity of penetration will be determined by the inertia of the target rather than by its plastic properties. On the other hand, the resultant deformation in the target will depend directly on the yield stress. The exact physical state of the metal in a Munroe jet is not yet known, but Evans and Ubbelohde speak of two types of jet, 'fluid' and 'fragment' jets, depending upon the nature of the metal (or other material) in the lining of the hollow.

We assume, therefore, as the basis for a theory of penetration, that (*a*) the material in a Munroe jet is either liquid or solid for which the flow stress is negligible, or it is a jet of fragments which break up on impact; (*b*) the yield stress of the target material may be neglected, to a first approximation, in comparison with the pressures set up by the penetrating jet.

It may be mentioned here (Evans and Ubbelohde 1950 a) that a metallurgical examination of steel blocks attacked by the Munroe jet from a hollow charge lined with steel showed that penetration was achieved by lateral expansion of the target material, the main displacement of the material being in a radial direction. Further, the diameter of the final crater produced in a target by a jet is larger than the diameter of the jet itself, indicating that the very high velocities of penetration lead to cavitation of the target material, as shown in Figure 1.

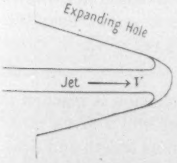

Figure 1.

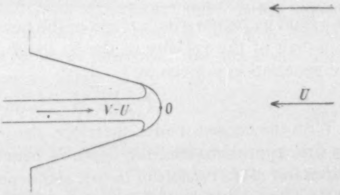

Figure 2.

Suppose (Figure 1) that the material in a Munroe jet moves with uniform velocity V and that it makes a hole in the target of diameter greater than its own. The material of the jet, which breaks up on hitting the bottom of the hole, is pushed away; in the metallurgical examination referred to above, particles of the steel lining were observed adhering in places to the walls of the cavity. Let U be the rate of increase of the length of the hole. Let the whole motion be in a steady state. If the jet has length L the time during which pressure is exerted on the bottom of the hole is $L/(V-U)$. The depth p of the penetration is therefore given by

$$p = LU/(V-U). \qquad \ldots\ldots(1)$$

If O is the point in the axis of the jet at the bottom of the hole, U may be determined by equating the pressure of the jet at O to the pressure required to drive a hole with velocity U into the target. Axes are taken through O along and perpendicular to the axis of the jet; relative to these axes the jet moves with velocity $V-U$, and the material of the target with velocity U at infinity (see Figure 2).

When U is very large, the material of the target may be treated as an inviscid fluid; the pressure that it exerts at O (the stagnation point) will then be $\frac{1}{2}\rho_T U^2$, assuming incompressibility; ρ_T is the density of the target.

The pressure exerted at O by the jet will depend upon its structure.

For a liquid jet or a solid jet of negligible flow stress the pressure will be $\frac{1}{2}\rho_j(V-U)^2$, where ρ_j is the density of the jet.

For a fragment jet, at the high velocities observed, it cannot make any difference whether the fragments are of a hard or soft metal, liquid or solid; they will, in any case, shatter on whatever surface they hit and cause penetration by the momentum transferred. A fragment jet, for which the metal occupies only a part of the volume, will, under these conditions, exert a mean pressure equal to $\bar{\rho}_j(V-U)^2$, $\bar{\rho}_j$ being the mass per unit volume of the jet.

Since for the opposite extreme (a fluid or solid jet where mass occupies the whole volume) the pressure at the stagnation point is half the above, it is reasonable to suppose that, for all jets of a *given* density ρ_j, the mean pressure at the stagnation point will lie between the limits $\frac{1}{2}\rho_j(V-U)^2$ and $\rho_j(V-U)^2$. The pressure may therefore be written as $\frac{1}{2}\lambda\rho_j(V-U)^2$, where $1 \leqslant \lambda \leqslant 2$, or $\frac{1}{2}\rho_j'(V-U)^2$, where $\rho_j' = \lambda\rho_j$, the effective density of the jet. Equating the pressure in the jet to that in the target at the stagnation point O, we have

$$\rho_T U^2 = \rho_j'(V-U)^2. \qquad \ldots\ldots(2)$$

The velocity of penetration is thus

$$U = V/\{1 + \sqrt{(\rho_T/\rho_j')}\}. \qquad \ldots\ldots(3)$$

For a fluid jet penetrating a target of the same material, the velocity of penetration is one-half of the velocity of the jet itself.

The penetration is given by*

$$p = LU/(V-U) = L\sqrt{(\rho_j'/\rho_T)}. \qquad \ldots\ldots(4)$$

With the chosen model, therefore, the interesting conclusion is reached that, to a first approximation, the depth of penetration by a jet into a given target is *independent of the velocity of the jet*, and depends only upon its length and density. For a given jet against different targets, the depth of penetration varies inversely as the square root of the density of the target attacked.

It should be noted that these formulae apply only if the target is made of a substance of low compressibility; for the very high pressures concerned, rubber

---

[*] This result was published by R. Hill, N. F. Mott and D. C. Pack in a Ministry of Supply Report, January 1944.

or paraffin could not be treated as incompressible. Furthermore, the pressures exerted by the jet must be very high compared with the yield stress of the target material. This condition is usually fulfilled; if ρ_j is put equal to the density of steel and $V = 10{,}000$ ft/sec., $\frac{1}{2}\rho_j V^2 \simeq 2{,}400$ tons/in^2, while the yield stress of steel is of the order 40 tons/in^2.

§ 3. LIMITATIONS OF PRECEDING THEORY

There are three important cases for which the simple theory outlined above is insufficient to account fully for the penetration observed.

From (4) it would be expected that penetration into armour would be the same as into steel, since their densities are equal, but it is an experimental fact that the depth achieved is definitely less. The difference must arise from strength considerations; in obtaining (4) the yield stress of the target was neglected in comparison with the pressures set up by the high-velocity jet.

The second difficulty arises when penetration into lead is measured. By equation (4) the penetration by a given jet is inversely proportional to the square root of the density of the target, and should therefore be less for lead than for steel; experiments on lead, however, have resulted in penetrations approximately double those which would have been predicted on theoretical grounds.

Lastly, the formula gives a value for the penetration which is independent of the distance between the base of the cavity charge and the face of the target (the 'stand-off'), while it is known from experiment that there is a marked dependence upon this distance. The effect of stand-off is due principally to a velocity gradient which exists in a Munroe jet, by virtue of which the jet elongates as it travels. The authors have shown however (in an unpublished paper) that if the assumption be made that there is a linear velocity gradient in the jet, then for targets of steel, armour, lead and aluminium, provided the stand-off is not too small, results taken at a *given* stand-off may be analysed sufficiently accurately by means of the simple formulae developed in the present paper.

§ 4. THE EFFECT OF TARGET STRENGTH

To obtain the fundamental equation (4) it is assumed that the yield stress of the target may be neglected in comparison with the pressure developed by a Munroe jet during penetration; that is, $Y/\rho_j V^2$ is neglected in comparison with unity, where Y denotes the dynamic yield stress of the target and V is the velocity of the jet. To make a correction for the effect of strength, one may suppose that the penetration is expanded in a series of powers of the non-dimensional parameter $Y/\rho_j V^2$, the first approximation being

$$p = L(\rho_j'/\rho_T)^{1/2}(1 - \alpha_1 Y/\rho_j V^2) \qquad \ldots\ldots(5)$$

where α_1 is a function of the densities of the jet and the target.

Estimates made by Evans and Pack (1951) show that for armour, which has a very high yield stress, the correction term $\alpha_1 Y/\rho_j V^2$ can be as much as 0·3. The effect of strength in such a case is to reduce the penetration given by (4) by 30 per cent. In lead the correction term is negligible for the same jets. The adjustment in the ratios of penetration in lead and armour caused by the strength correction is however, not sufficiently large to account for the relative excess of penetration observed in lead.

§ 5. SECONDARY PENETRATION

Secondary penetration is defined as that which occurs after the main jet penetration is ended.

It is known experimentally that a Munroe jet makes a wide hole in a target of lead, and this is attributable to the low yield stress of this metal. The jet sets the lead in motion laterally, and the final width of the hole represents the diameter at which the energy of the motion has been expended against the resistance of the target to the flow. This being so, we may consider what is the position in the target when the last particle of the jet has been consumed. A high pressure has been applied to the bottom of the hole, and suddenly ceases to act. The hole continues to expand until the motion begun by the pressure has been damped out by the resistance to the flow. If the previous pressure be uniformly distributed over the bottom of the hole, the latter, expanding freely, adopts a hemispherical shape. This has been found to be roughly the shape of the bottom of the crater made by Munroe jets in general, when plug effects are not present (Evans and Pack 1951), so that the increment in penetration due to the free afterflow of the target is approximately equal to the radius of the hole made by the jet.

Under these conditions the penetration of a Munroe jet into a ductile target may now be written in a form which allows for the effect of strength and for the secondary penetration. Denoting by p the *total penetration* into a target and defining the *elementary penetration* p' as the quantity given by the equation $p' = L\sqrt{(\rho_j'/\rho_T)}$, then

$$p = p'(1 - \alpha_1 Y/\rho_j V^2) + r, \qquad \text{.....(6)}$$

where r is the *secondary penetration*, which will be put equal to the radius of the hole made by the jet. The quantity $p'(1 - \alpha_1 Y/\rho_j V^2)$ will be called the *primary penetration*.

In another paper it will be shown how the two phases of the penetration may be separated experimentally, and how the formulae developed above may be used for practical purposes.

ACKNOWLEDGMENTS

The work presented above was carried out in the Armament Research Establishment of the Ministry of Supply and originally published in Ministry of Supply reports during 1944–1946. Professor N. F. Mott, Dr. R. Hill and one of the authors (D. C. P.) worked together on the earliest theoretical developments, resulting in the publication of the conclusions of § 2 in January 1944.

The authors are indebted to Professor Mott for his kind advice and encouragement throughout. Acknowledgment is also made to the Chief Scientist, Ministry of Supply, and to the Controller, H.M. Stationery Office, for permission to publish this paper.

REFERENCES

Birkhoff, G., MacDougall, D. P., Pugh, E. M., and Taylor, G. I., 1948, *J. Appl. Phys.*, **19**, 563.

Evans, W. M., and Pack, D. C., 1951, *Proc. Phys. Soc.* B, **64**, 303.

Evans, W. M., and Ubbelohde, A. R., 1950 a, *Research*, **3**, 331; 1950 b, *Ibid.*, **3**, 376.

Munroe, C. E., 1888, *Amer. J. Sci.*, **36**, 48.

Payman, W., and Woodhead, D. W., 1937, *Proc. Roy. Soc.* A, **163**, 575.

Penetration by High-Velocity ('Munroe') Jets: II

By W. M. EVANS and D. C. PACK*
Armament Research Establishment, Fort Halstead, Kent

*Communicated by N. F. Mott; MS. received 19th July 1950,
and in amended form 10th November 1950*

ABSTRACT. Work is described in which the two stages of penetration by a high-velocity ('Munroe') jet were separated experimentally. The large penetrations measured in lead targets are shown to result from the flow which takes place in the metal after the jet itself has been consumed. For a given jet at a given stand-off it is possible to predict the penetration into a combination of targets from the results of a very small number of standard experiments. The method depends upon the calculation of a certain quantity which is constant for a given jet at a given stand-off, and examples are given of the determination of this quantity from experimental data.

§ 1. INTRODUCTION

In a previous paper (Pack and Evans 1951, to be referred to as I) is given a theory of penetration by Munroe jets in which the penetration observed in a ductile target is divided into two parts: (i) the primary penetration, which depends chiefly upon the density of the target, and (ii) the secondary penetration, which takes place after the jet has ceased to act, and which represents the expenditure of the energy left in the target at the time the last particle of the jet has been consumed. In the present paper work is described in which the factors involved have been separated experimentally, and an analysis of the results provides reasonable confirmation of the proposed theory, making it possible to predict the penetration of a high-velocity jet into any combination of ductile targets, using the results obtained from a very small number of standard experiments.

It is known that when a conical metal lining is used for a hollow charge, the metal divides into two parts, the high-velocity Munroe jet in front and a slower, much wider (and often solid) piece of metal, usually called the 'plug', behind. The plug is capable of increasing the penetration, acting after the jet has been consumed, and our experiments have thrown some light upon its behaviour.

§ 2. THE RELATION BETWEEN ENERGY AND VOLUME DAMAGE

It has already been mentioned (I) that a Munroe jet displaces the target material almost laterally during penetration. The work done is therefore approximately equal to that required to make a cylindrical hole. It has been shown by Bishop, Hill and Mott (1945) that, for static punching, R, the work per unit volume required to form a hole deep in an infinite block, is, to a good approximation, independent of the shape of the hole. For materials which do not harden appreciably R is of the order of 3·5 to 4 times Y, where Y is the initial yield stress. For annealed metals R may be between $5Y$ and $6Y$. When a hole is made dynamically R depends also upon the mean rate of strain. For large strain rates, however, R will not vary between wide limits of the velocity of penetration, on account of the logarithmic dependence of yield stress upon rate of strain. Thus, neglecting surface effects,

---

* Now at University College, Dundee, University of St. Andrews.

work done per unit length of hole $= R \times$ area of cross section of hole ...(1)

This relationship is presumably also valid for the dynamic penetration by a Munroe jet, as long as we are sufficiently far from the surface of the target. The latter restriction is not very important for Munroe jet penetrations, since they are usually deep compared with the radius of the surface crater. The equation therefore provides a connection between the energy given up by the jet and the volume damage in a target.

The equation for the penetration due to a cylindrical jet of mean density ρ_j and length L entering a target of density ρ_T and yield stress Y was given as

$$p = L(\lambda\rho_j/\rho_T)^{1/2}(1-\alpha_1 Y/\rho_j V^2) + r = L(\lambda\rho_j/\rho_T)^{1/2}(1-kR) + r, \text{ using (1)}, \quad \ldots(2')$$

where λ is a factor between 1 and 2 depending upon the nature of the jet, k is a factor depending upon the properties of the jet and the density of the target, and r is the radius of the crater (measured near the bottom of the hole). r is the *secondary* penetration; $L(\rho_j'/\rho_T)^{1/2}$, where $\rho_j' = \lambda\rho_j$, is the *elementary* penetration obtained by neglecting both target strength and secondary effects.

For the sake of abbreviation, (2′) is written

$$p = p'(1-kR) + r. \quad \ldots\ldots(2)$$

$p'(1-kR)$ is called the *primary penetration.*

The ratio of the values of R for two targets may be found, by virtue of (1), by comparing the ratio of the volumes of the craters made by a standard jet. For steel and armour, which, having equal density, have the same factor k in (2) and the same elementary penetration, the effect of the strength on the penetration may therefore be calculated, without the assumption of any numerical details concerning the jet, by solving two equations of the type (2) for the unknowns p' and kR, the equations being supplied by experimental observation of p, r and the volumes of the holes made by a given jet.

§ 3. PREVENTION OF AFTER-FLOW: EXPERIMENTAL WORK

It follows from what has already been said that the penetration would be wholly primary if 'after-flow' or secondary penetration could be prevented. The most simple test of this theory is to back the target in which secondary penetration is considered to be of importance with a second metal, such as steel or armour, for which the resistance to flow is very high. We may then analyse the results of the combined penetrations and compare them with those observed in massive blocks of the individual metals.

A series of experiments on combined targets has been carried out to examine these hypotheses. Charges were made up consisting of 60 gm. of explosive confined in $1\frac{3}{8}$ in. internal diameter mild steel tubing of $\frac{1}{10}$ in. wall thickness, and lined at the base by (i) 80° pressed mild steel cones 0·032 D thick, and (ii) pressed caps of tin of 0·73 D radius of curvature and 0·044 D thick, where D is the internal diameter of the charge. The targets used consisted of massive blocks of mild steel, homogeneous armour plate and lead, various thicknesses of lead backed with mild steel, and various combinations of armour and mild steel. For the conical type of charge the stand-off (i.e. the distance at which the base of the charge is placed from the target) was D, and for the tin caps 2·3 D.

The results are given in Tables 1 to 5.

Table 1

	Mean penetration (mm.)	Mean volume of hole (cm^3)	Mean radius of bottom of crater (mm.)
Mild steel cones			
(allowing for effect of plug)			
Massive mild steel	66·5	11	8·5
Massive homogeneous armour	61·5	7	6
Massive lead	83	382	37·5
Mild steel laminae stacked together	66	10·5	8·5
Tin caps			
Massive mild steel	65	10	5
Massive homogeneous armour	55	6	3
Massive lead	97	472·5	40

Table 2. Mild Steel Cones

	Thickness of lead penetrated (mm.)	Penetration of steel underneath (mm.)	K	K'
Lead backed with mild steel plates	10	49	155	180
	10	49	155	180
	15	35	130	155
	37	18	153	179
	37	25	174	200
	39	19	163	188
	49	7	165†	186
	54·5	2	*	
	60	2	*	
	62·5	0	*	
Stack of mild steel plates			172	197
Massive lead			154	280
Mean			158	
Standard deviation			12	

† Assuming zero primary penetration into steel.
* Values omitted for reasons given on page 309.

Table 3. Mild Steel Cones

	Thickness of armour penetrated (mm.)	Penetration of steel underneath (mm.)	K	K'
Armour backed with mild steel plates	19·5	37	145	171
	19·5	40	154	180
	39·5	22	163	188
	39·5	25	172	197
	39·5	20	157	182
Stack of mild steel plates			172	197
Massive armour			172	190
Mean			162	
Standard deviation			10	

Table 4. Tin Caps

	Thickness of lead penetrated (mm.)	Penetration of steel underneath (mm.)	K	K'
Lead backed with mild steel block	14	44	177	194
	27	38	201	218
	38	27	201	218
	51	12	195	212
	56	6·5	194	211
	75	0	*	
Massive steel			199	216
Massive lead			192	328
Mean			194	
Standard deviation			8	

* Value omitted for reasons given on page 310.

Table 5. Tin Caps

	Thickness of mild steel penetrated (mm.)	Penetration of armour underneath (mm.)	K	K'
Mild steel backed with armour block	35	26·5	206	218
	39	25	214	225
	50	12·5	203	214
	62	0	*	
	63	0	*	
Massive armour			199	210
Massive steel			199	216
Mean			204	
Standard deviation			6	

* Values omitted for reasons given on page 310.

§ 4. PENETRATION PHENOMENA

It will be of interest at this point to remark on some of the observations made during this series of experiments, which bring to light characteristics of the behaviour of the plug from a conical lining, the plug being the more slowly moving but larger mass of metal which follows the high-velocity jet. No plug is found when caps of tin are used.

It has been observed, by means of x-ray flash photographs, that the plug from a conical lining is much wider than the jet. In consequence, it often happens that, with a steel target, in which the jet bores a hole of only 4–5 times its own radius, the plug becomes trapped in the hole, particularly if it is not well aligned with the jet. In penetration of lead, however, the width of the hole is so much greater that the plug is enabled to travel freely until the jet has ceased to act. The plug is then to be considered as a projectile, and its penetration has been measured in the way outlined below.

For a massive lead target, attacked by the jet from a conical steel lining, the shape of the bottom of the crater was found by partially filling the hole with paraffin wax in which a T-shaped handle was inserted. On cooling of the wax, the cast was removed by pulling the handle. A photograph of the cast is given in Figure 1 (*b*)*. By rounding off the contour at the discontinuity, the extent of the total jet penetration could be judged, and it was then found that the plug penetration was approximately 30 mm. For a lead block of critical thickness (i.e. of thickness equal to the *total penetration* for lead alone), backed with steel, it was observed that there was a sudden constriction of the hole at the bottom of the lead block, together with a penetration of 5 mm. into the steel. The latter measures the penetration of the plug into steel, and due allowance for this factor has been made in the calculations on cones.

---

* See Plate at end of issue.

The resistance offered by a target to the passage of a projectile is dependent to a high degree on the shape of the projectile and upon its deformability; for the plug we may perhaps prescribe limits by consideration of the laws found by Hill (1944) for resistance to ogival-shaped heads. For a given projectile there is a critical velocity above which cavitation sets in, i.e. the target ceases to maintain contact with the projectile along the whole of its length. Below the critical velocity resistance is proportional to Y, the dynamic yield stress of the target, and an easy calculation shows that penetration is inversely proportional to Y. At velocities which are very high compared with the critical velocity, the resistance is proportional to ρV^2, where ρ is the target density and V is the velocity. Under these conditions penetration is inversely proportional to density. Comparing steel and lead, we see that we should expect the penetrations by the plug to lie between near-equality (corresponding to the density law) and an excess in lead of proportion equal to the ratio of dynamic yield stresses of steel and lead; in fact, the observed penetration of the plug in lead is about six times what is observed in steel, so that the ratio lies between the limits prescribed.

The contour of the hole in a massive lead block caused by a tin cap is given (Figure 1 (*a*)) for the sake of comparison with that caused by a coned charge.

§ 5. SURFACE CHARACTERISTICS IN A COMBINED TARGET ATTACKED BY A PROJECTILE

Interesting as further experimental evidence on the behaviour of a plug as a projectile is the fact that for coned charges against critical thickness of lead resting on steel (or more generally where the thickness of lead lies between this value and—a lesser value—that of the primary penetration) the steel shows an upward lipping. The latter is well known as a characteristic of projectile penetration. When the jet itself succeeds in penetrating into the steel backing, the front face characteristic in the steel is a depression.

Dr. G. O. Baines, of the Armament Research Department, kindly verified that the upward lipping of the lower plate occurs in projectile penetration when lead rests upon steel, just as for plug penetration. He fired bullets of hard steel with 4 calibres radius head, coated with copper on the body, with velocities 1,500 and 1,900 ft/sec. into lead blocks, 1½ in. thick, standing upon steel plates. Two different hardnesses of steel plate were used. As far as could be seen, there was no difference in the front surface of the steel plates with or without lead, due allowance being made for the loss of velocity in the lead and the skew penetration of the bullet after passing through it. The lead was found to have been pressed hard against the steel plates AA (Figure 2), and a cavity BB was formed which accommodated the front lip of the steel.

It is seen that, as the head of the projectile penetrates the steel, the tendency to lip succeeds on account of the pressure of the steel against the softer lead, maintained by the presence of the projectile. We know, also, that lipping occurs if the lead is moved away by cavitation before the steel is attached (plug penetration). It appears, then, that for *jet* penetration the velocity of free expansion of steel must be greater than that of lead, or at least of the same order, and that the motion of the steel is then inclined to be in the direction of motion of the jet, as is observed in the interior of a block. In other words, the jet does not meet a free steel surface.

§ 6. MULTIPLE TARGETS

The laws which hold when a Munroe jet penetrates a series of targets of varying densities and strengths may be derived as follows:

Suppose the jet to penetrate *completely* $(n-1)$ targets of thicknesses p_1, p_2 . . . , p_{n-1}, densities ρ_1, ρ_2, . . ., ρ_{n-1}, the strengths of which involve terms k_1R_1, k_2R_2 . . . , $k_{n-1}R_{n-1}$ in equation (2). Let the jet penetrate only partially, a distance p_n, into the nth target, of density ρ_n and strength correction k_nR_n. Let the secondary penetration in the last target be r_n and suppose that the targets are so arranged that there will be no secondary penetration in the first $(n-1)$ targets. Then if successive lengths L_1, L_2, . . . , L_n of the jet are used up in penetrating successive targets, the whole jet length being L, we have the following series of equations:

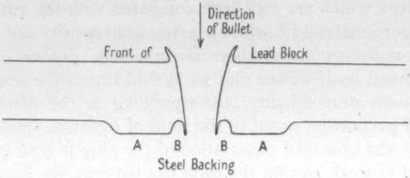

Figure 2.

$$p_1 = L_1(\rho_j'/\rho_1)^{1/2}(1-k_1R_1),$$
$$p_2 = L_2(\rho_j'/\rho_2)^{1/2}(1-k_2R_2),$$
$$. \quad . \quad . \quad . \quad . \quad . \quad . \quad . \quad . \quad . \quad . \quad .$$
$$p_{n-1} = L_{n-1}(\rho_j'/\rho_{n-1})^{1/2}(1-k_{n-1}R_{n-1}),$$
$$p_n = L_n(\rho_j'/\rho_n)^{1/2}(1-k_nR_n)+r_n,$$

from which it is easy to see that

$$\sum_{m=1}^{n} \frac{p_m\sqrt{\rho_m}}{1-k_mR_m} = L\sqrt{\rho_j'} + \frac{r_n\sqrt{\rho_n}}{1-k_nR_n}, \qquad \ldots\ldots(3)$$

or

$$\sum_{m=1}^{n} \frac{p_m\sqrt{\rho_m}}{1-k_mR_m} - \frac{r_n\sqrt{\rho_n}}{1-k_nR_n} = K, \qquad \ldots\ldots(4)$$

where K is an absolute constant for a given jet at given stand-off.

For the double targets used in the experiments of this paper we use the form

$$\frac{p_1\sqrt{\rho_1}}{1-k_1R_1} + \frac{p_2\sqrt{\rho_2}}{1-k_2R_2} - \frac{r_2\sqrt{\rho_2}}{1-k_2R_2} = K$$

and evaluate K in order to assess the reliability of the theory. The values obtained (after allowance for the plug in the case of the steel cones) are included in the

Tables, and cover the range from a semi-infinite block of the front material to zero thickness. The effect of the removal of the backing is clearly seen in the values of the expression

$$K' = \frac{p_1\sqrt{\rho_1}}{1-k_1R_1} + \frac{p_2\sqrt{\rho_2}}{1-k_2R_2},$$

which would be constant in the absence of secondary penetration. The leap in K' accompanying the transition from a block of a certain limiting thickness in lead backed by steel to a massive block of lead is striking evidence of the secondary effect (Tables 2, 4).

§ 7. EXPERIMENTS WITH MILD STEEL CONES

The method of application of the formulae may best be seen by means of an example.

The appropriate values of kR are found from the results on massive targets. It is seen, for example (Table 1), that the jet from the mild steel cone penetrates 66 mm. of mild steel plates, with crater volume 10·5 cm³ and mean radius 8·5 mm.; in homogeneous armour plate the respective values are 61·5 mm., 7·0 cm³, 6·0 mm. Since the densities are the same, k is the same for each. The ratio of R_S (steel) to R_A (armour) is inversely proportional to the volumes; thus $R_A/R_S=1{\cdot}5$. Hence we have, using (2),

$$66=p_S'(1-k_SR_S)+8{\cdot}5;\ \ 61{\cdot}5=p_A'(1-1{\cdot}5\,k_SR_S)+6{\cdot}0$$

with $p_A'=p_S'$, on account of the equality of the densities of armour and steel, from which we deduce that $p_S'=p_A'=61{\cdot}5$ mm., $k_SR_S=0{\cdot}065$. Thus, in the mild steel plates for example, we see that the elementary penetration is 61·5 mm., the primary penetration is 57·5 mm. and the secondary penetration is 8·5 mm., the last two combined giving the total observed penetration of 66 mm.

The strength of lead is so small compared with that of mild steel that the term kR may be neglected in this case. Hence the expected penetration into a massive lead block will be

$$p=p_S'(\rho_{\text{steel}}/\rho_{\text{lead}})^{1/2}+\text{radius of crater in lead}=50{\cdot}9+37{\cdot}5=88{\cdot}4\text{ mm.}$$

The observed mean penetration was 83 mm. (Table 1).

It is to be noted from the Tables that the mean value of K is practically the same for the two sets of experiments, and that the standard deviation is 8% and 6% of the mean respectively. Certain values are omitted in the computation of the means, since they correspond to thicknesses of lead greater than the primary penetration; that is, there is some secondary penetration in the lead in these cases. The standard deviation lies well within the experimental consistency obtainable; it is possible to find as much as 20% variation in the measure of a penetration between two identical rounds under identical conditions. The tables of K can, then, be taken as satisfactory evidence in favour of the theory.

§ 8. EXPERIMENTS WITH TIN CAPS

The reason for the use of the tin caps was to obtain a set of results which would be free from the liability of error introduced by the presence of a plug. It has already been remarked that the contours of the holes made by these jets had no discontinuities; the results of the experiments were therefore much easier to interpret correctly. Furthermore, it was possible to use blocks of the backing material instead of plates, as in the previous case, since it was no longer necessary to check the true position of the plug; this avoided errors due to discontinuities which might occur in a stack of plates, though from Table 1 this error is seen to be small.

Denoting the effective resistances to flow of steel and armour by R_S, R_A, as before, we have $R_A/R_S \simeq 1{\cdot}7$, $p_S' = 71{\cdot}4$ mm., $k_S R_S = 0{\cdot}16$, $k_A R_A = 0{\cdot}27$. We see, then, that the primary penetration of the tin cap was 84% of the elementary penetration into mild steel, and 73% of it into armour.

The corresponding penetration expected theoretically in lead is 99 mm., and the mean observed penetration (Table 1) was 97 mm. The mean value of K is somewhat higher for the steel–armour combination than for the lead–steel, but again the difference and the standard deviations are small.

As before, certain results have been omitted in the calculations since the target thickness of the front material exceeded the primary penetration for the material. It is of interest to observe here, as confirmation of the hypothesis that afterflow occurs after the jet process has ceased, and is not a simultaneous phenomenon, that for the above targets, although the upper material was completely penetrated, there was no effect on the backing material—this, too, despite the fact that the thickness of the front target was not as great as the total observed penetration in a massive block of the same material.

ACKNOWLEDGMENTS

The authors wish to acknowledge the kind advice and encouragement given to them by Professor N. F. Mott during these investigations, and the assistance given by Mr. W. W. Rees in the experimental work. They are also indebted to the Chief Scientist, Ministry of Supply, and to the Controller of H.M. Stationery Office for permission to publish this paper.

REFERENCES

Bishop, R. F., Hill, R., and Mott, N. F., 1945, *Proc. Phys. Soc.*, **57**, 147.
Hill, R., 1944, *Ministry of Supply Report.*
Pack, D. C., and Evans, W. M., 1951, *Proc. Phys. Soc.* B, **64**, 298.

An Electromechanical Source of Elastic Waves in the Ground

By F. F. EVISON*
Geophysics Department, Imperial College, London

Communicated by J. M. Bruckshaw; MS. received 22nd September 1950

ABSTRACT. In order to extend the study and use of the elastic properties of geological bodies to include effects involving the amplitude and frequency of elastic radiation, a new source of energy is needed.

A large moving-coil transducer is described which, when attached rigidly to the rock, radiates sinusoidal vibrations of controllable amplitude, frequency and duration. The operation of the vibrator is analysed in detail by the method of electromechanical analogy.

For experiments in a chalk-mine, energy at each of the frequencies 300, 600 and 1,000 c/s. was radiated in the form of a square-enveloped pulse, of 20 msec. duration. Vibrations were detected in the rock by means of a piezoelectric microphone, amplifiers and an oscillograph, with an overall magnification of about 10^9. Oscillograms show the complex disturbances produced by the arrival of direct and reflected energy, at distances out to the limit of the mine at 450 ft. Measurements of amplitude at 130 ft. are used to examine the mechanism of the transfer of energy from the vibrator to the rock.

The power radiated was about 0·05 watt at 600 c/s., of which about one-sixth was in the compressional mode and five-sixths in the shear mode; but this power may readily be increased.

---

§ 1. INTRODUCTION

Our present knowledge of the phenomena involved in the propagation of elastic energy in the ground has been gained from the study of natural and artificial earthquakes, and is limited to such aspects as are revealed by energy in the form produced by these catastrophic sources. Seismic and explosive waves are characterized by a high intensity, rapidly established, followed by a complex of vibrations of indeterminate form. From measurements of the time at which the impulse, defined by its onset, reaches known points of observation its path may be calculated, and hence the geological structures traversed may be accurately mapped. Thus seismology explores the earth's deep interior, and seismic prospecting the outermost few miles of the crust.

Since no such precise information is conveyed by other features of the impulse, phenomena involving the frequency and intensity of the propagated energy have been used only qualitatively, or studied as disturbing effects. Sufficient concerning these phenomena has already been discovered, however, to encourage a special study of them. For such a study the frequency content of the radiated energy must be brought under control and much simplified. Efforts to control the frequency of explosive waves have had little success; an essentially more refined source is clearly required. At the same time, to dispense with the well-defined onset of the seismic impulse would be to abandon the means of determining the path followed, upon the knowledge of which the study of many aspects of propagation depends. For some purposes, on the other hand, continuous vibrations are useful. The apparatus described here radiates sinusoidal vibrations at various audio frequencies, either continuously or in the form of a square-enveloped pulse.

---

* Now at Geophysics Department, D.S.I.R., Wellington, New Zealand.

§2. PREVIOUS EXPERIMENTS AND APPARATUS

The most successful published work on the radiation of elastic energy into the ground from a mechanical source was that of Howell, Kean and Thompson (1940). A moving-coil apparatus, weighing some 300 lb., was used to generate vibrations of frequency 400 c/s., which were detected out to a distance of 1,200 ft. at the surface and down to 100 ft. in a borehole. More general interest is attached to the measurements in depth than to the surface waves. The borehole measurements were extended to a depth of 400 ft. with a magnetostriction tube source, set into resonance at 900 c/s. by means of a condenser discharge. The experiments were carried out below the water-table in ground consisting mainly of water sands (Howell, private communication), and since water also provided the connection between the vibrators and the ground, the medium probably resembled water itself rather than solid rock.

In experiments on a smaller scale two different methods of coupling a vibrator rigidly to rock have been used. Haskell (private communication) achieved a range of 165 ft. in limestone, using a small magnetostriction rod furnished with a tapered brass end, which fitted tightly into a cylindrical hole in the rock. The magnetostriction rods used by Bradfield (1947), on the other hand, had flat ends, to give contact with the medium over a circular surface, but it was found more convenient to cement suitably designed metal seatings into the rock than to grind the surface of the rock itself. Both these workers were concerned with frequencies of several kilocycles per second.

At very low frequencies vibrating devices, such as the eccentric flywheel, have been widely used to test the ground as a foundation for engineering structures. A measurement is usually made of the frequency of maximum ground displacement; this is often called the ‘ natural frequency of the ground ’ (Crockett and Hammond 1949), although it is determined by the stiffness of the ground together with the mass of the machine. In general, the propagation of energy is of no significance to the measurements. In some cases, however, a kind of resonance may arise in a layer of rock of appropriate thickness, or perhaps from a complex set of reflected waves arriving from various depths and directions (Byerly, private communication).

Sharpe (private communication) has attempted to study the transmission properties of surface rocks, at frequencies of 10 to 200 c/s., by means of a variable-reluctance steady-state vibrator. Severe attenuation and the difficulty of coupling the detector to the rock limited the range of measurement to 12 ft. In seeking a method for measuring the thickness of overburden, Northwood (private communication) tried various electromechanical vibrators, the largest of which was an array of rochelle-salt units, about 1 ft. in diameter. For this problem, however, blasting caps proved satisfactory, though success was confined to waterlogged ground.

Little progress has evidently been made towards a general study of elastic propagation by means of electromechanical vibrators. In the work described above, special difficulties have usually arisen out of the particular objects in view. Surface rocks, though of obvious importance to practical methods of prospecting, are notoriously poor elastic media, and work at the surface has been diverted from the main task by the convenient use of water. A preference for portable apparatus has tended to limit the power of sources or to encourage the use of excessively high frequencies. Thus the major preliminary problems have remained: to generate a large mechanical energy at suitable frequencies and to impart a useful fraction of this energy to rock so that it will be radiated as elastic waves.

§ 3. THE VIBRATOR

In order to radiate elastic energy in rock, by contrast with fluid media, a relatively large force must be developed, since the displacement is necessarily very small. The frequency of vibration for the present experiments was chosen to give a wavelength of the order of ten feet, so that discontinuities at ranges of a few hundred feet could be adequately resolved without incurring too great attenuation. Thus a reasonably transportable apparatus was required, capable of producing large pressures at frequencies around 500 c/s. A convenient nucleus for such an apparatus was provided by an Admiralty Fessenden oscillator, of the type formerly in service for underwater signalling and depth-sounding. This device was suggested by Dr. A. B. Wood, and a machine was kindly made available by Messrs. de Havilland Propellers, Ltd.

The Fessenden oscillator (Figure 1) is a transducer of the moving-coil type, with the special feature, of great advantage for the present work, that the moving part is a large, robust cylinder of copper. The cylinder is suspended in the air-gap of an annular electromagnet, on the core of which is wound an A.C. coil only slightly smaller than the copper cylinder. Close inductive coupling is thus achieved between the A.C. coil and the cylinder, in which large currents may be induced, and, since the cylinder lies in the D.C. field, a corresponding mechanical force is set up between the cylinder and the electromagnet.

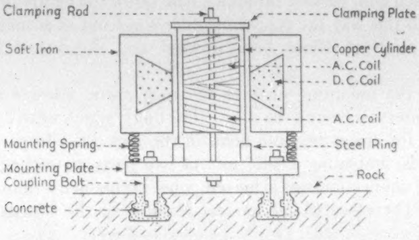

Figure 1. The vibrator.

For use in water the oscillator had incorporated a massive diaphragm, some 30 in. in diameter. With this diaphragm, and its mounting-flange removed, the bulk of the oscillator was reduced virtually to that of the electromagnet alone, consisting of a steel cylinder 8 in. high, 20 in. in diameter and weighing some 600 lb. The weight of the enclosed copper cylinder was about 6 lb. The mechanical problem was to connect these masses to each other and to the rock so that a considerable part of their energy of motion would be communicated to the ground and radiated.

The analysis given below leads to three practical conclusions: first, the copper cylinder should be rigid with the rock; secondly, the magnet mass should be supported by springs of suitable compliance; thirdly, the force should be distributed over as wide an area of the rock as practicable. The first and third requirements are somewhat contradictory, and called for a compromise in the design. To specify the best conditions with any accuracy would involve the calculation of every effective compliance present, an excessively complicated task in a system of such high mechanical impedance. The simple precaution was therefore taken of using massive steel members wherever rigidity was desired, while the diameter of the coupling system was made only double that of the copper cylinder. Measurements will be quoted later to show that the coupling system, constructed in this way, possessed adequate rigidity and effected a satisfactory transfer of energy.

The magnet mass was mounted, by means of three springs, upon a circular steel plate, 1½ in. thick and 18 in. in diameter. In order to leave room between magnet and mounting plate for the springs, and also for the power leads, a steel ring of length 3 in. and wall-thickness ⅝ in. was inserted between the lower end of the copper cylinder, which protruded slightly from the ends of the magnet, and the mounting plate. This ring fitted tightly to the mounting plate, and accommodated the copper cylinder in a shallow groove in its upper end. The copper cylinder could then be clamped between the mounting plate below and a ⅝-in.-thick steel disc above, by means of a steel rod of diameter 1¼ in., fitted with a nut at each end, passing through a hole down the centre of the iron core of the magnet. In this way the copper cylinder was fixed as securely as possible to the mounting plate, to which both upward and downward forces could be transmitted.

To anchor the mounting plate to the rock, three massive steel bolts were fitted at equal intervals around the edge. The bolts, which were 2½ in. in diameter, were designed for cementing into holes in the rock 3 in. deep. With the holes tapered upwards, and using a fluid mix of two parts of washed sand to one of cement, a good connection was achieved, which remained sound throughout the experiments. The essential mechanical features of the vibrator may be seen in Figure 1.

Electrically the Fessenden oscillator consists of an iron-cored transformer with a single turn for secondary, together with a D.C. magnet. The A.C. was derived from an alternator driven by an electric motor. Both the motor and the D.C. supply were operated from 230 V. A.C. mains.

§4. MECHANICAL ANALYSIS

Theoretical formulae have been calculated for the radiation impedance, in a solid medium, of various ideal types of small radiator (Bradfield 1947). Since the present experiments were carried out in the narrow galleries of underground quarries, where surface waves could not arise, the vibrator may be regarded as an oscillating sphere immersed in the rock, but coupled over the lower half of its surface only. Halving each term of the formula, quoted by Bradfield, for a completely immersed sphere, the radiation impedance of the vibrator becomes

$$Z_r = 8\pi^3 r^4 f^2 (2/V_s^3 - 1/V_c^3) V_c V_s d/3 + j(2\pi^2 r^3 f d/3 - 4 r V_c V_s d/f), \qquad \ldots\ldots(1)$$

where r is the effective radius of the vibrator, f is the frequency, V_s is the velocity of shear waves in the rock, V_c that of compressional waves, and d is the density of the rock. Here the positive reactive term clearly involves the mass of rock set bodily into motion, the negative reactive term indicates the stiffness of the rock, and the resistive term represents the ability of the rock to dissipate energy by radiation. Expressed in terms of mechanical elements, the formula may be written

$$Z_r = 1/G_r + j(\omega M_r - 1/\omega C_r), \qquad \ldots\ldots(2)$$

where G_r, M_r, C_r are respectively the effective leakance, mass and compliance of the rock and $\omega = 2\pi f$. Some opportunity is given by measurements on the propagated energy, as described later, to test the validity of formula (1) in the present work.

A mechanical analysis of the vibrator has been carried out, with the help of electrical circuit theory, by means of a formal analogy between mechanical force and electric current and between relative velocity and electric potential difference. This analogy, which compares electrical impedance with mechanical admittance, defined as the ratio of velocity to force, is preferable to the more usual analogy comparing impedances in both cases for two reasons. First, the mechanical system is much more readily represented as an admittance diagram than an impedance diagram (Gehlshøj 1947); secondly, the analogy conforms with the fundamental electromechanical relations for a moving conductor.

The stages in the analysis are shown in order in Figure 2. Figure 2(*a*) represents the essential mechanical components of the vibrator and their physical arrangement, as may be seen by comparison with Figure 1. In Figure 2(*b*) the mechanical elements—masses, compliances and leakances—are abstracted, and the source of motional energy is represented as a generator G. The mechanical admittance diagram is now easily constructed (Figure 2(*c*)), on the principle that all masses are considered to move relative to a certain frame of reference, which may be taken as the ground itself at a distance sufficiently great to be completely unaffected by the radiated energy. At this stage the electromechanical analogy emerges, and the mechanical elements are represented by their electrical analogues.

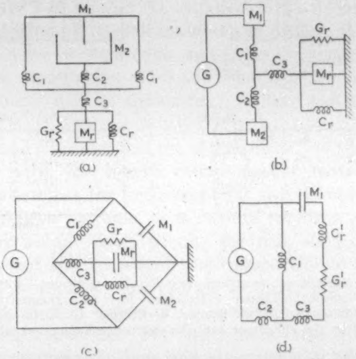

Figure 2. Analogical analysis of the mechanical system. M_1 is the mass of the magnet, M_2 the mass of the copper cylinder, M_r the radiation mass, C_1 the compliance of the mounting springs, C_2 the compliance of cylinder and clamping rod, C_3 the compliance of the coupling system, C_r the radiation compliance, G_r the radiation leakance, $G_r' = G_r\omega^2 C_r^2/(G_r^2+\omega^2 C_r^2)$, $C_r' = C_r G_r^2/(G_r^2+\omega^2 C_r^2)$ and G is the electrical system regarded as a source of energy.

It will be noted that the masses of the mounting plate and coupling bolts have been omitted as negligible. The mass of the copper cylinder M_2 has been included to clarify the analysis, although both this mass and the effective mass of the rock M_r are eventually negligible (Figure 2(*d*)). That the compliance C_3

of the coupling system was significant, and that, on the other hand, all leakance due to friction could be neglected, were deduced from the measurements to be described later. For convenience in the calculations the radiation leakance and radiation compliance have been represented in Figure 2(*d*) as a series combination, consisting of a leakance G_r' and a compliance C_r', the formulae for these two quantities being given in the captions to Figure 2.

§ 5. THE ELECTROMECHANICAL CIRCUIT

The complete vibrator, except for the D.C. circuits and the driving motor, is represented by a single electrical network in Figure 3. In its electrical aspects the Fessenden oscillator has been analysed as a transformer of negligible leakage inductance.

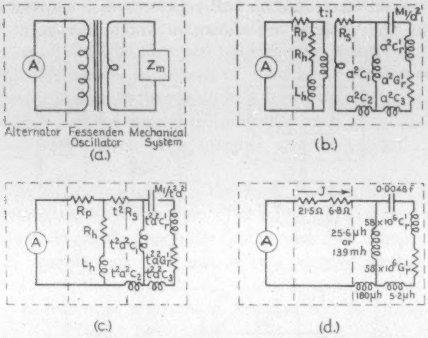

Figure 3. Complete equivalent electrical circuit. Z_m=motional impedance, R_p=A.C. coil resistance, R_s=copper cylinder resistance, R_h=A.C. magnetizing circuit resistance, L_h=A.C. magnetizing circuit inductance, t=number of turns in A.C. coil, J=constant current supplied by the alternator and a^2=electromechanical transformation factor.

The electromechanical relations for the copper cylinder are

$$F=10^{-1}BLJ \qquad \ldots\ldots(3) \qquad \text{and} \qquad U=10^{-8}BLv, \qquad \ldots\ldots(4)$$

where F dynes is the mechanical force on the cylinder, B gauss is the magnetic flux-density in the air-gap, L cm. is the circumference of the cylinder, J amp. is the current flowing in the cylinder, U volt is the back E.M.F., and v cm/sec. is the velocity of the cylinder. The equivalent electrical impedance, or motional impedance, of the mechanical system is thus given by

$$Z_m=U/J=10^{-9}B^2L^2v/F=a^2y, \qquad \ldots\ldots(5)$$

where y is the mechanical admittance and $a^2=10^{-9}B^2L^2$. Hence, by incorporating the factor a^2, in the appropriate way, in each element of the mechanical admittance diagram of Figure 2(*d*), the mechanical system has been represented in its equivalent electrical form in Figure 3(*b*).

Numerical values have been inserted in Figure 3(*d*) for the various electrical properties of the vibrator that are substantially independent of frequency. Laboratory measurements showed that the air-gap flux-density approached a saturation value of 7,250 gauss for an energizing current of 3·0 amp. D.C. Since the circumference of the copper cylinder is 64 cm., the value of the electromechanical transformation factor a^2 is found to be 215 c.g.s. units. By open-circuited transformer tests the parallel branch of Figure 3 (*c*) representing the A.C. magnetizing circuit was found to have an impedance of the order of $100(1+j)$ ohms; this branch may therefore be regarded as an open circuit, and has been omitted in Figure 3 (*d*). The A.C. coil consisted of 520 turns, with a resistance 21·5 ohms; the resistance of the copper cylinder may be calculated as $25{\cdot}5 \times 10^{-6}$ ohm.

The effects of the mechanical elements of Figure 3 (*c*) depend essentially on frequency, and, as regards the radiation elements, on the properties of the rock as well. From Figure 3 (*c*) two general features of the mechanical system may, however, be appreciated. First, since the maximum current is desired through the radiation elements, the compliances C_2 and C_3 should be as small as possible—that is, the copper cylinder should be rigid with the rock. By using the stoutest possible members to clamp the cylinder, as described above, the compliance C_2 was reduced to an unavoidable minimum, comprising the compliance of the clamping rod together with that of the cylinder itself. From the dimensions of these members, and Young's moduli for steel and copper, the compliances may be calculated as $24{\cdot}0 \times 10^{-13}$ cm/dyne and $7{\cdot}0 \times 10^{-13}$ cm/dyne, respectively; altogether, C_2 was thus about $31{\cdot}0 \times 10^{-13}$ cm/dyne. The compliance C_3 of the coupling system will be shown later to have had the very low value $0{\cdot}9 \times 10^{-13}$ cm/dyne.

Secondly, Figure 3 (*c*) shows that the compliance C_1 of the mounting springs appears in parallel with the branch containing the radiation elements, and therefore largely determines the performance of the vibrator. There are three cases of interest. At one extreme, as is obvious mechanically, if these springs were very stiff they would 'short circuit' the rock altogether. At the other extreme very compliant springs would admit practically no force, and the force applied to the ground would be that exerted by the cylinder. In between these extremes there is a range of values of C_1 for which the reactances of the two branches are of comparable size. For such values force will be applied to the ground through the mounting springs, and advantage may be taken of mechanical resonance to increase the force.

Two sets of mounting springs were used in the experiments. One set, consisting of three coil springs of parallel compliance $2{\cdot}4 \times 10^{-9}$ cm/dyne, provided a virtual open circuit in Figure 3 (*c*). The other set consisted of three steel rods, each 3 in. long and $\frac{3}{4}$ in. in diameter; the parallel compliance of these rods may be calculated as $4{\cdot}4 \times 10^{-13}$ cm/dyne, giving a reactance comparable with that of the branch containing the radiation elements. With the exception of the radiation elements, which in most conditions were relatively small, the mechanical properties of the vibrator are evaluated, in terms of the equivalent electrical properties, in Figure 3 (*d*).

A third general feature of the vibrator is now apparent, that, largely as a result of the rigid construction, the equivalent electrical impedance of the mechanical side is of a smaller order of magnitude than the impedance of the electrical side. At the frequency 600 c/s., for example, the reactance of the 600-lb. magnet mass M_1 is $-0{\cdot}06j$ ohm, whereas the resistance R_p of the A.C. coil is 21·5 ohms. This contrast gives some measure of the difficulty of communicating the motion of a vibrator to rock and, in particular, of the very low efficiency to be expected of such a machine. For purposes of analysis it is concluded that the electrical side will appear from the mechanical side, in Figure 3, as a source of constant current.

§ 6. THE VIBRATOR IN CHALK

The experiments to be described were carried out in an old chalk mine at Chislehurst, Kent, popularly known as the Chislehurst Caves. From observations of direct waves the velocities of propagation in the chalk were found to be $V_c = 7{\cdot}0$ ft/msec. and $V_s = 4{\cdot}1$ ft/msec. The density of the chalk is about $1{\cdot}8\,\text{gm/cm}^3$. The effective radius of the vibrator was taken as 20 cm., the actual radius to the centres of the coupling bolts. From these values the radiation impedance given by equation (1) has been calculated for the frequencies 300 c/s. and 600 c/s. Table 1 gives the values of the radiation elements defined by equation (2) and of the corresponding series elements of Figure 2(*d*).

Table 1. Values of Radiation Elements in the Chalk at Chislehurst (C.G.S. units)

f (c/s.)	$1/G_r$	ωM_r	$1/\omega C_r$	G_r'	C_r'
300	$5{\cdot}2 \times 10^7$	$2{\cdot}8 \times 10^7$	$12{\cdot}9 \times 10^9$	$3{\cdot}18 \times 10^{-13}$	$0{\cdot}41 \times 10^{-13}$
600	$20{\cdot}8 \times 10^7$	$5{\cdot}7 \times 10^7$	$6{\cdot}4 \times 10^9$	$50{\cdot}8 \times 10^{-13}$	$0{\cdot}41 \times 10^{-13}$

Here the positive reactive term ωM_r is clearly negligible.

The equivalent electrical properties of the vibrator at Chislehurst are fully evaluated, for the frequencies 300 c/s. and 600 c/s., in Figure 4(*a*) and (*b*), respectively. It will be noticed that the equivalent radiation resistance increases rapidly with frequency as the dimensions of the vibrator become more comparable with the wavelength of the radiated energy.

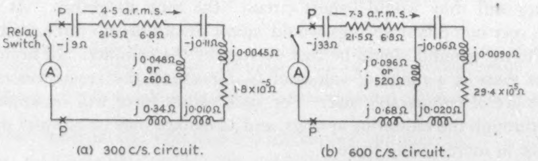

(a) 300 c/s. circuit. (b) 600 c/s. circuit.

Figure 4. Equivalent electrical circuit in chalk.

Figure 4 shows that, provided the coupling compliance is kept small enough, mechanical resonance may be achieved by a proper choice of mounting compliance. To obtain a large magnification, however, it would be necessary to reduce the magnet mass; or a similar effect could be gained by mounting the copper cylinder on springs and fixing the magnet mass to the rock. But such a modification would increase the selectivity of the apparatus at the expense of its ability to produce a well-formed pulse of vibrations. Further, in proportion as the moving mass is diminished, its amplitude of vibration for a given force is increased, and with it the intensity of sound radiated into the air. Even with the minute displacements occurring in the present apparatus, special care was sometimes necessary, particularly in working with continuous vibrations, to avoid airborne interference in the receiver.

The alternator, which was rated to deliver 2 kw. at the frequency 500 c/s., with an output voltage of 180 v. r.m.s., was driven by a 3-H.P. motor. Frequencies from 300 c/s. to 1,000 c/s. were obtained by varying the size of pulley on the alternator shaft; at each frequency suitable condensers were inserted in the A.C. circuit, as shown in Figure 4.

The A.C. circuit could be closed, for precisely 20 msec., by a relay switch actuated from the receiver. The pulse of voltage thus applied to the vibrator, measured for convenience between the points marked P in Figure 4, is shown, for the frequencies 300 c/s. and 1,000 c/s., in the oscillograph records of Figure 5 (Plate *). In the photographs the lower time-base carries an oscillation of frequency 50c/s. as a time-scale. In contrast with the form of an explosive impulse, the pulse is seen to consist of substantially sinusoidal oscillations of equal amplitude. (The high-frequency distortion produced by the alternator is of no importance.) At the same time, both the onset and the end of the pulse are abrupt. By measurements from these records the current flowing during the pulse has beencalculated and is given in Figure 4.

§7. THE RECEIVED VIBRATIONS

Vibrations in the rock were detected by a Rothermel pickup, Model VP-5, which is essentially an inertia-operated rochelle-salt crystal microphone. Constant sensitivity was obtained by using a patent clamping device, the ‘Rawlplug’, to make the microphone fast to the rock. The microphone voltage was amplified about 10^4 times by a two-stage circuit of low noise characteristic, and a further 900 times by the oscillograph amplifier. The oscillograph was a Cossor Double-Beam Model 339, with camera attachment. Comparing the oscillograph deflection with the ground displacement, the maximum available magnification in the receiver was about 10^9. In the records the amplitude of deflection was adjusted to a suitable level by means of a calibrated gain-control.

The time-base of the oscillograph was non-repetitive, and was triggered by operating a switch which at the same time actuated the relay switch in the vibrator circuit. Thus the initiation of the radiated pulse and commencement of the time-base were connected in a constant time relation; it can be shown that the onset of vibrations at the source occurred at a time 6 ± 1 msec. along the time-base.

Vibrations were recorded at intervals of distance out to the limit of the mine, 450 ft. from the vibrator. At each point of observation, and for each frequency, the disturbance produced by a single transmitted pulse was found to be protracted and complex, resulting from the arrival of a succession of compressional and shear vibrations, some propagated directly, others reflected from depths down to several hundred feet in the chalk. Some records are shown in Figure 6 (Plate). Figure 6 (*a*) and (*b*), taken at the same point in identical conditions, are included to demonstrate the high degree of repeatability achieved in the experiments. It will be seen that the vibrations recorded on these two occasions were similar down to minute details, the most noticeable difference between the records being in the phase of the time-scale, which was random.

The observed disturbances are analysed in terms of the travel-time of each separate arrival, and various geological conclusions are drawn (Evison, to be published elsewhere). On the basis of the travel-time analysis deductions are also made from an examination of the amplitude of the various arrivals. No detailed study of frequency effects has yet been attempted, although it is clear from the records that the apparatus offers access to such effects.

---

* For all Plates see end of issue.

§8. INFERRED PROPERTIES OF THE VIBRATOR

The finer mechanical details of the vibrator may be deduced from comparative measurements of the vibrations appearing at a convenient point, with the vibrator in various conditions of adjustment. Figure 7 shows records made 130 ft. from the vibrator, at the frequencies 300 c/s. and 600 c/s., with the magnet mass mounted first on the steel rods and then on the coil springs. Since only the amplitude of the radiated energy is to be observed, no prior analysis of the received vibrations into separate arrivals is necessary. For each record the peak-to-peak amplitude of the maximum deflection was measured, from the photographic negative, to the nearest quarter-millimetre. The gain of the amplifier was the same for the two 300 c/s. records; at 600 c/s., the gain was 50% higher for the coil springs than for the rods. In Table 2 the relative ground displacement is derived for each frequency, taking account of the relative receiver gain.

Table 2. Performance of Vibrator with Spring Mountings, relative to Performance with Rod Mountings

Frequency (c/s.)	Relative oscilloscope deflection	Relative receiver voltage gain	Relative ground displacement
300	16·75 mm/15·5 mm. = 1·08	1·00	1·08
600	17·5 mm/16·5 mm. = 1·06	1·50	0·71

According to Figure 4, the ground displacement at the vibrator is proportional to the current flowing in the substantially capacitive branch of a parallel circuit. As a first approximation it will be assumed that this branch contains only the magnet mass M_1, for the radiation elements are small, and the coupling compliance C_3 was revealed only by the present calculations. For simplicity the transformation factor a^2 will be omitted from the calculations, which may then be referred to Figure 2 (*d*), the generator G being regarded as a source of constant current.

If Z be the equivalent parallel impedance of the rod compliance C_1 and the mass M_1, and I the current in the arm containing M_1 and the radiation elements, and if the corresponding quantities for the circuit involving the spring compliance be Z', C_1' and I', then

$$I'/I = Z'/Z = (1/j\omega C_1 + j\omega M_1)/(1/j\omega C_1' + j\omega M_1). \qquad \ldots\ldots(6)$$

But C_1' is known to be very large, so that, simplifying,

$$I'/I = 1 - 1/\omega^2 C_1 M_1. \qquad \ldots\ldots(7)$$

It may be assumed that the ratio I'/I is given numerically by the ratio of ground displacements in Table 2; but the sign of the latter ratio is left undetermined by the measurements. Rewriting equation (7) in the form

$$1/C_1 M_1 = \omega^2(1 - I'/I), \qquad \ldots\ldots(8)$$

it is easily shown that, for the measurements to be approximately consistent, I'/I is to be taken as negative at 300 c/s. and positive at 600 c/s. The two values of $1/C_1M_1$ are then $7{\cdot}4 \times 10^6$ and $4{\cdot}1 \times 10^6$ respectively. Evidently the minor mechanical elements, so far neglected, are not without significance to the measurements of Table 2.

The possibility of significant resistive elements appearing in the circuit, to represent frictional or mechanical hysteresis losses in the vibrator, or a very much greater radiation of energy, has been investigated. The appropriate formulae developed for these cases have led to impossible values for the various elements if they are to satisfy the above observations as well. It follows that the dissipation of energy in the form of heat has negligible effect upon the mechanical operation of the vibrator.

The simplest circuit that can be postulated, consistent with the measurements, includes a compliance C_M in series with the mass M_1. For such a circuit,

$$C_1(1-I'/I)+C_M=1/\omega^2 M_1.$$

Inserting the known values of I'/I, ω and M_1, two simultaneous equations are obtained:

$$2{\cdot}08C_1+C_M=10{\cdot}4\times 10^{-13}, \text{ at } 300\,\text{c/s.}$$

and

$$0{\cdot}29C_1+C_M=\ 2{\cdot}6\times 10^{-13}, \text{ at } 600\,\text{c/s.}$$

Hence C_1, the compliance of the steel rods, is found to be $4{\cdot}4\times 10^{-13}$ cm/dyne, the same value as that already calculated from the Young's modulus and dimensions of the rods; it is thus clear that the only significant compliance in the mounting arrangement is that of the rods themselves. Completing the solution, C_M is found to be $1{\cdot}3\times 10^{-13}$ cm/dyne. Reference to Figure 2 shows that this compliance represents the sum of the effective compliance of the rock C_r' and the compliance C_3 of the coupling system. The theoretical value of C_r' is given in Table 1 as $0{\cdot}41\times 10^{-13}$ cm/dyne; the corresponding value of C_3, namely $0{\cdot}9\times 10^{-13}$ cm/dyne, will be largely accounted for by the coupling bolts.

The calculations show that a satisfactory degree of rigidity was achieved in the coupling system; there was evidently no slip in the metal joints between the coupling bolts and the concrete or between the concrete and the rock. Upper limits have also been established for the values of the radiation elements, and to this extent formula (1) is verified. Further, particularly in giving an independent derivation of the compliance of the mounting rods, the calculations have shown the mechanical analysis of the vibrator to be sound. It is of wider importance that precise information has been gained from measurements of the amplitude of radiated vibrations, for such measurements should also be capable of providing data on propagational phenomena, and on the geological formations traversed, with similar accuracy.

§ 9. POWER AND EFFICIENCY

From the relative recorded amplitudes of the direct waves and certain reflected waves it was found that the radiation pattern of the vibrator in chalk was consistent with that shown in Figure 8, for which there is some theoretical basis. The vertical pattern for the shear energy is a pair of equal semicircles with diameters at the level of the floor of the mine, and, for the compressional

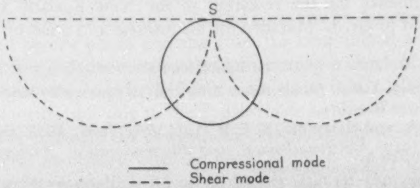

Figure 8. Vertical radiation pattern of the vibrator, showing loci of equal displacement amplitudes. The continuous curve refers to the compressional mode and the broken curve to the shear mode. S is a point on the surface at the centre of the vibrator.

energy, a circle of radius one-half that of the semicircles, touching the floor of the mine at the vibrator. The three-dimensional pattern is obtained by revolving Figure 8 about the vertical axis of symmetry. Integrating the absolute amplitude, as measured, over the radiation pattern, the power radiated during the pulse may be calculated. At 600 c/s., with rod-mountings, the power is found to be 0·012 watt in the compressional mode and 0·060 watt in the shear mode, making 0·072 watt in all. The proportion of energy radiated in the compressional mode is thus about 17 per cent. As would be expected, this value is rather greater than the theoretical value for an oscillating sphere, which is about 11 per cent for the condition $2\pi rf/V_c=0{\cdot}35$, as in the present case (Bradfield 1947).

The total radiated power may be independently calculated from the theoretical equivalent radiation resistance and the measured current supplied from the alternator, as shown in Figure 4 (*b*). Taking account of the current magnification effected in the mechanical circuit, the power so calculated is 0·031 watt. The discrepancy between the two values is less than 4 db., lending support both to the measurements of amplitude and to the use of equation (1) as an expression of the radiation impedance.

The total power dissipated in the apparatus during the 600 c/s. pulse was about 2 kw. Thus the efficiency of the vibrator as a radiator has the extremely low value of about $0{\cdot}025\times10^{-3}$. The efficiency of a dynamite explosion near the surface of the ground is of the order $1{\cdot}0\times10^{-3}$ (Willmore 1949). It is worth noting, however, that the energy radiated from the vibrator is in precisely the form desired, whereas only a small fraction of the elastic energy generated by an explosive source is turned to use.

§ 10. CONCLUSION

The vibrator radiates elastic energy in rock in a form that can be accurately controlled as to frequency, amplitude and duration. The power radiated is small, but sufficient to be detected, in favourable conditions, through many hundreds of feet of rock. Much greater power could be obtained without difficulty, by increasing the area of coupling to the rock, by reducing the electrical resistance of the vibrator coil and by using an alternator of higher voltage. In providing a more versatile means of studying the phenomena of elastic propagation in rocks the apparatus should assist fundamental research, particularly within the shallower strata of the crust, the domain of mining and engineering geology.

ACKNOWLEDGMENTS

The author wishes to thank Dr. J. McG. Bruckshaw for his valuable advice and encouragement throughout the work.

Appreciation is also gratefully expressed to the Anglo-Iranian Oil Company for providing finance for the research, to the New Zealand Government for financial aid, and to Dr. E. Marsden for his interest and good offices.

REFERENCES

Bradfield, G., 1947, *T.R.E. Memorandum* Z/M 120/GB (quoted by kind permission of the National Coal Board).

Crockett, J. H. A., and Hammond, R. E. R., 1949, *Proc. Instn. Mech. Engrs.*, **160,** 512.

Gehlshøj, B., 1947, *Electromechanical and Electroacoustical Analogies* (Copenhagen: Academy of Technical Sciences).

Howell, L. G., Kean, C. H., and Thompson, R. R., 1940, *Geophysics*, **5,** 1.

Willmore, P. L., 1949, *Phil. Trans. Roy. Soc.* A, **242,** 123.

Contour Modes of Square Plates excited Piezoelectrically and Determination of Elastic and Piezoelectric Coefficients

By R. BECHMANN
Post Office Research Station, Dollis Hill, London

MS. received 19th June 1950

ABSTRACT. The suitability of square plates, vibrating in contour modes, for the determination of piezoelectric coefficients is considered. Piezoelectric measurements on such plates provide checks for the theoretical solution of the various modes and in particular for the distribution of displacement. The recently published solutions for square plates form a basis for this work and the reliability of these solutions is discussed. The materials used were sodium chlorate, sodium bromate, quartz, ammonium dihydrogen phosphate and ethylene diamine tartrate (EDT). New determinations of the elastic and piezoelectric coefficients of these materials have been made, with the exception of EDT, the data for which were published in a previous paper.

§ 1. INTRODUCTION

DURING recent years, the vibrations of crystalline bodies have been widely studied. Rough approximations for the solution of free vibrating plates of anisotropic materials were obtained by Mason (1934) for the face shear mode of square plates and by the author (Bechmann 1941, 1942) for the contour modes of vibration of square and rectangular plates. More systematic studies made by Ekstein (1944), Mähly (1945), Mähly and Trösch (1947) on thin square plates have resulted in better approximations for the solution of both the frequency and the distribution function of the displacement. The author's (1941) approximate solution describes the shear mode and two longitudinal modes of vibration; a third observed longitudinal mode (Bechmann 1942) (the frequency constant denoted by N_4) was not explained. The solution of this mode has been derived by Ekstein (1944).

The form of vibration can be studied from lycopodium patterns and by various optical methods. The solutions can also be verified from results of electrical measurements of frequency and of the elements of the equivalent electric circuit of plates with known elastic and piezoelectric constants, since the elements of the equivalent electric circuit are functions of the distribution of displacement. Once the solutions have been so checked, they can be used to derive, dynamically, unknown constants of other materials. In some cases, the same coefficient of a crystal can be obtained from different modes. For example, the piezoelectric coefficient d_{14} of a crystal belonging to a cubic class can be determined from four different modes of square plates and also from the longitudinal mode of narrow bars, thus giving five independent results and forming a check of the theory on which the formulae were based. Differences in these values, after allowing for errors in measurements, are due to the approximate nature of the solution.

With the recent extended use of synthetic crystals as piezoelectric resonators, one of the problems associated with the investigation is the production of cuts with small temperature coefficients of frequency and of the elements of the equivalent electric circuit. This necessitates a knowledge of elastic and piezoelectric constants and their behaviour with temperature. Some of these constants can be determined using the results on the various modes of vibrating square plates mentioned above.

§ 2. CONTOUR MODES OF VIBRATION OF THIN SQUARE PLATES AND LONGITUDINAL MODE OF NARROW BARS

In the following, using a Cartesian coordinate system, a thin square plate of the thickness t is assumed to have its normal parallel to the Z axis and its sides of length l parallel to the X and Y axes, with the centre of the plate at the origin. The axes of the coordinate system do not necessarily coincide with any of the natural axes of a crystal but the usual ' dashes ' denoting arbitrary orientations are omitted. The three longitudinal modes of vibration will be denoted modes 1, 2, 3 as introduced by Ekstein (1944), who describes them in detail with diagrams. For comparison, the equations for a narrow bar are included, where a narrow bar is defined as having its length l along the X axis, its breadth b along the Y axis and its thickness t along the Z axis, the centre at the origin of the coordinate system.

The solutions for the different modes of vibration for free and undamped plates vibrating in the fundamental frequencies are considered. The conditions of these plates are $X_z=0$, $Y_z=0$, $Z_z=0$ on the surfaces, and also throughout the plate (Voigt 1910, Ekstein 1944) and the strain–stress relations reduce to the equations

$$\left.\begin{aligned} -x_x &= s_{11}X_x+s_{12}Y_y+s_{16}X_y,\\ -y_y &= s_{12}X_x+s_{22}Y_y+s_{26}X_y,\\ -x_y &= s_{16}X_x+s_{26}Y_y+s_{66}X_y.\end{aligned}\right\} \qquad \ldots\ldots(1)$$

X_x, Y_y, X_y are the average values of the stresses taken over the thickness of the plate. Solving equations (1) by determinants:

$$\left.\begin{aligned} X_x &= \gamma_{11}x_x+\gamma_{12}y_y+\gamma_{16}x_y,\\ Y_y &= \gamma_{12}x_x+\gamma_{22}y_y+\gamma_{26}x_y,\\ X_y &= \gamma_{16}x_x+\gamma_{26}y_y+\gamma_{66}x_y,\end{aligned}\right\} \qquad \ldots\ldots(1\,a)$$

where $\gamma_{ik}=\gamma_{ki}$ are elastic moduli (stiffness factors) first derived by Voigt (1910). For quasi-isotropic conditions $s_{11}=s_{22}$, $s_{16}=0$, $s_{26}=0$ $\qquad \ldots\ldots(2)$
the expressions for γ_{ik} become:

$$\left.\begin{aligned} \gamma_{11}=\gamma_{22} &= \frac{s_{11}}{s_{11}{}^2-s_{12}{}^2}=\frac{E}{1-\sigma^2},\\ \gamma_{12} &= -\frac{s_{12}}{s_{11}{}^2-s_{12}{}^2}=\frac{E\sigma}{1-\sigma^2},\\ \gamma_{66} &= \frac{1}{s_{66}}, \quad \gamma_{16}=\gamma_{26}=0,\end{aligned}\right\} \qquad \ldots\ldots(3)$$

where $E=1/s_{11}$ is Young's modulus and $\sigma=-s_{12}/s_{11}=\gamma_{12}/\gamma_{11}$ is Poisson's ratio. For the more general conditions, when

$$s_{11}=s_{22} \text{ and } s_{16}=s_{26} \qquad \ldots\ldots(4)$$

these expressions are:

$$\left.\begin{aligned}\Pi\gamma_{11}&=\Pi\gamma_{22}=s_{11}s_{66}-s_{16}{}^{2},\\ \Pi\gamma_{12}&=s_{16}{}^{2}-s_{12}s_{66},\\ \Pi\gamma_{66}&=s_{11}{}^{2}-s_{12}{}^{2},\\ \Pi\gamma_{16}&=\Pi\gamma_{26}=(s_{12}-s_{11})s_{16},\\ \Pi&=(s_{11}{}^{2}-s_{12}{}^{2})s_{66}-2(s_{11}-s_{12})s_{16}{}^{2}.\end{aligned}\right\}\qquad\ldots\ldots(5)$$

Under conditions (2) and (4) the relationship $(s_{11}-s_{12})(\gamma_{11}-\gamma_{12})=1$ holds. The γ_{ik} $(i, k=1, 2, 6)$ are only applicable for the Z plane; for the other coordinate planes similar expressions hold, but the indices i, k are changed in a cyclic order. For each coordinate plane, the six expressions γ_{ik} transform in a similar manner to the corresponding elastic moduli c_{ik}. The transformation can also be made using the transformed s_{ik} in the expressions (3) or (5) defining γ_{ik}. In the more general case of oblique planes the second method is the simplest.

The frequency $\nu=\omega/2\pi$ of the different modes of vibration considered can be calculated from the general equation,

$$\rho\omega^{2}/k^{2}=\gamma,\qquad\ldots\ldots(6)$$

where ρ is the density, k the wavelength constant and γ the elastic modulus, which assumes different forms for the different modes of vibration. Table 1 contains expressions for γ for the three longitudinal modes of square plates, the longitudinal mode of narrow bars and the contour shear mode of square plates, all under conditions (2). All values for the elastic coefficients s_{ik} used to calculate the expressions for γ are the isagric values s_{ik}^{E}. The expressions for the components of displacement u, v for these modes are also included.* For the longitudinal modes $k=\pi/l$, and for the shear mode k is defined by equation (8). A_i $(i=1\ldots5)$ is a small arbitrary constant expressing the amplitude of displacement.

The following remarks may be made with respect to the different modes:

(i) *Longitudinal mode* 1 *of square plates.* Identical solutions have been derived by different methods by Petrzilka (1935), Bechmann (1941) and Ekstein (1944). The solution is exact for plates fulfilling conditions (2) and the more general conditions (4).

(ii) *Longitudinal mode* 2 *of square plates.* The solution for this mode was first derived by Ekstein (1944) for conditions (2), but is valid for both conditions (2) and (4). The expression for γ corresponds with that given by Petrzilka (1935) for his modes A and B, but his equations for the displacement do not agree with Ekstein's. Increasing differences between observed values for frequency and values calculated with γ given in Table 1 are found for increasing values of $\tau=(\gamma_{12}{}^{2}+\gamma_{16}{}^{2})^{1/2}/\gamma_{11}$ (§ 5.2 (ii)). In the case of cuts fulfilling conditions (2), $\tau=\sigma$.

(iii) *Longitudinal mode* 3 *of square plates.* The solution quoted in Table 1 was given by Ekstein (1944). An isolated mode can only be obtained under conditions (2) or under the more general conditions when $s_{11}=s_{22}$ and $s_{26}=-s_{16}$, and there is no coupling with the shear mode. In the author's earlier approximation (Bechmann 1942), the frequency is determined by the elastic modulus

$$\gamma=1/(s_{11}+s_{12})=E/(1-\sigma).\qquad\ldots\ldots(7)$$

---

* The argument $e^{i\omega t}$ is omitted from Tables 1 and 2.

Table 1. Solution of various Modes of Vibration

	γ	Components of displacement
Longitudinal mode 1	$\gamma_{11}-\gamma_{12}$	$u=A_1 \sin kx \cos ky$ $v=-A_1 \cos kx \sin ky$
Longitudinal mode 2	γ_{11}	$u=A_2(\cos ky-\frac{1}{4}\pi)\sin kx$ $v=-A_2(\cos kx-\frac{1}{4}\pi)\sin ky$
Longitudinal mode 3	$\gamma_{11}+\frac{8}{\pi^2}\gamma_{12}$	$u=A_3 \sin kx$ $v=A_3 \sin ky$
Longitudinal mode narrow bar	$\frac{1}{s_{11}}$	$u=A_4 \sin kx$
Contour shear mode	γ_{66}	$u=A_5 \sin ky+\ldots$ $v=A_5 \sin kx+\ldots$

The more rigorous expression given in Table 1 can be written as:

$$\frac{E}{1-\sigma}\left[1-\frac{\sigma}{(1+\sigma)}\left(1-\frac{8}{\pi^2}\right)\right].$$

This differs from the expression (7) only by the term in square brackets which depends on σ, but the author's formula for the displacement has a different form from Ekstein's. Mähly (1945) criticized Ekstein's formula for γ and also formula (7). He mentioned a better approximation for the solution of this mode, which has not been published, and gave his results for the frequency in the form of a curve plotted against σ. Also on the same graph are curves of results derived from Ekstein's expression for γ (Table 1) and from (7) providing a comparison of the accuracy of these solutions. In addition, he gave a graph showing the distribution of the displacement for $\sigma=0{\cdot}3$, which differs slightly from the distribution given in Table 1.

(iv) *Longitudinal mode of narrow bars.* Line 4 of Table 1 contains the corresponding expressions for longitudinally vibrating narrow bars, which are included for comparison and for the determination of the appropriate elastic coefficients s_{ik}.

(v) *Contour shear mode of square plates.* Approximate solutions for shear vibrating square plates have been given by Mason (1934), Bechmann (1941), and Ekstein (1944). Recently a closer approximation has been derived by Mähly and Trösch (1947) which takes into account longitudinal effects in order to fulfil the boundary conditions. The expression for γ and the main terms of the expressions for the components of displacement* are given in Table 1, but the terms covering the longitudinal effects are omitted as they only influence areas near the edges and do not affect the considerations in the following sections. The wavelength constant for this mode is

$$k=2\kappa/l \qquad \ldots\ldots(8)$$

where

$$\tan\kappa+\kappa=0. \qquad \ldots\ldots(9)$$

The first root of equation (9) is $\kappa=2{\cdot}0288$. But to determine the frequency from equation (6), a corrected expression for k should be used:

$$k=2\kappa\Delta/l \qquad \ldots\ldots(10)$$

where

$$\Delta=1-\frac{1}{2\kappa}\left(\frac{\kappa^2-2}{\kappa^2+2}\right)^{3/2}\mu^{1/2}, \quad \mu=\frac{s_{11}}{s_{66}}. \qquad \ldots\ldots(10\,a)$$

Mähly and Trösch discuss the accuracy of the frequency solution in their paper.

---

[*] The author has been informed of the displacement expression by a private communication from Mähly, and details will be seen in his Thesis (Zürich).

§ 3. ELEMENTS OF THE EQUIVALENT ELECTRIC CIRCUIT

The properties of any piezoelectrically excited mode of a lightly damped mechanically vibrating system having many degrees of freedom can be represented, near resonance of the operating frequency, by an electric circuit consisting of a series combination of capacitance, inductance, and resistance, shunted by a capacitance approximately equal to the static capacitance of the electrode arrangement. The dynamic capacitance and inductance are the stiffness and effective mass of the mechanical oscillator transformed into electrical terms by the piezoelectric effect. Since the mechanical and electrical systems are equivalent, the energy at any instant due to the piezoelectric excitation is equal to that of the mechanical system. This relationship is given by equations for frequency, and kinetic, potential and dissipated energy, but only those for frequency and kinetic energy T are used:

$$\omega = 2\pi\nu = k\left(\frac{\gamma}{\rho}\right)^{1/2} = \left(\frac{1}{L_k C_k}\right)^{1/2}, \qquad \ldots\ldots(11)$$

$$T = \frac{\rho}{2}\int_V \left\{\left(\frac{\partial u}{\partial t}\right)^2 + \left(\frac{\partial v}{\partial t}\right)^2\right\} dV = \frac{1}{2} L_k I_p^2 \qquad \ldots\ldots(12)$$

the integral being taken over the volume V of the vibrating plate, where L_k and C_k are the inductance and capacitance of the equivalent electric circuit and I_p, the total current due to the piezoelectric polarization.

From equations (11) and (12), the inductance and capacitance are

$$L_k = \frac{2T}{I_p^2}, \quad \ldots\ldots(13) \qquad C_k = \frac{I_p^2}{2\omega^2 T}. \qquad \ldots\ldots(14)$$

It is assumed that the faces of the plates normal to the Z axis are covered with a thin conducting layer. The component of the piezoelectric polarization P_z is produced by the mechanical stress and, therefore, the current I_p is obtained from the integral over the covered area a,

$$I_p = \int_a \frac{\partial P_z}{\partial t}\, da = \int_a \frac{\partial}{\partial t}(d_{31}'X_x + d_{32}'Y_y + d_{36}'X_y)\, da, \qquad \ldots\ldots(15)$$

Primes are introduced here for the piezoelectric coefficients to emphasize the use of an arbitrary coordinate system. Equation (15) can also be used to study the effects of partial plating.

Since piezoelectric crystals of practical interest are generally lightly damped; the solutions for free and undamped vibrations, given in § 2, can be used without introducing any appreciable error.

The following assumptions for the piezoelectric coefficients are made for the various modes considered in § 2:

$$\left.\begin{array}{lll} \text{longitudinal modes 1 and 2:} & d = d_{31}' = -d_{32}', & d_{36}' = 0 \\ \text{longitudinal mode 3:} & d = d_{31}' = d_{32}', & d_{36}' = 0 \\ \text{longitudinal mode for bars:} & d = d_{31}' \neq 0, & d_{32}' = 0,\ d_{36}' = 0 \\ \text{shear mode:} & d = d_{36}' \neq 0. & d_{31}' = 0,\ d_{32}' = 0 \end{array}\right\} \ldots\ldots(16)$$

All other piezoelectric coefficients are assumed zero. The primed symbols with the same suffixes for the piezoelectric coefficient are different for the various modes.

Table 2. Energy, Current and the Constant β for various Modes of Vibration

	T	I_p	β
Longitudinal mode 1	$\frac{A_1^2}{4}\rho\omega^2 V$	$8A_1\gamma d\frac{\omega}{k}$	$\frac{512}{\pi^4}$
Longitudinal mode 2	$\frac{A_2^2}{4}\rho\omega^2\left(\frac{\pi^2}{8}-1\right)V$	$8A_2\gamma d\frac{\omega}{k}\left(1-\frac{\pi^2}{8}\right)$	$\frac{512}{\pi^4}\left(\frac{\pi^2}{8}-1\right)$
Longitudinal mode 3	$\frac{A_3^2}{2}\rho\omega^2 V$	$4A_3\gamma d\frac{\omega}{k}\pi$	$\frac{64}{\pi^2}$
Longitudinal mode narrow bar	$\frac{A_4^2}{4}\rho\omega^2 V$	$2A_4\gamma d\omega b$	$\frac{32}{\pi^2}$
Contour shear mode	$\frac{A_5^2}{2}\rho\omega^2(1+\cos^2\kappa)V$	$4A_5\gamma d\omega l\sin\kappa$	$\frac{4\pi^2}{\kappa^2(\kappa^2+2)}$

From equations (12) and (15), using the formulae given in Table 1, the expressions for kinetic energy T and electric current I_p can be calculated, since $X_i=\gamma x_i$. The results, assuming the faces are fully plated, are given in Table 2, where γ and d are abbreviations for the resultant elastic moduli and piezoelectric coefficients as defined in Table 1 and in equations (16). The dynamic capacitance C_k can be obtained from T and I_p, using equation (14). By eliminating γ, using equation (6), and introducing the capacitance constant $\Gamma=C_k t/a$, and the frequency constant $N=\nu l$, a general expression is obtained for the capacitance constant, which holds for all the cases considered:

$$\Gamma=\rho\beta d^2 N^2, \qquad \ldots\ldots(17)$$

where β is a constant, dependent only on the distribution of displacement, having the form given in Table 2 for fully plated crystals.* Equation (17) also holds for a first approximation of the effects of partial plating and β, then, depends on the arrangement of the electrodes. Solving equation (17) for d:

$$d=\left(\frac{1}{\rho\beta}\frac{\Gamma}{N^2}\right)^{1/2}. \qquad \ldots\ldots(18)$$

The frequency constant N is obtained from equation (6),

$$N=\nu l=\frac{kl}{2\pi}\left(\frac{\gamma}{\rho}\right)^{1/2}, \qquad \ldots\ldots(19)$$

where γ is taken from Table 1 and k is as previously defined.

For the shear mode, if the earlier solution for the distribution of displacement given by Mason (1934) and the author (1941):

$$u=\cos kx\sin ky, \quad v=\sin kx\cos ky \quad (k=\pi/l)$$

is used, then $\beta_1=128/\pi^4$ and, comparing with the value in Table 2, the ratio $\beta/\beta_1=\pi^6/32\kappa^2(\kappa^2+2)=1{\cdot}19$; substituting the value of β_1 in equation (18), values of d about 9·27% higher would be obtained. Similarly, if the author's (1941) distribution formula for mode 3: $u=\sin kx\cos ky$, $v=\cos kx\sin ky$ is used, then $\beta_1=512/\pi^4$ and, comparing with Table 2, the ratio $\beta/\beta_1=\pi^2/8=1{\cdot}23$, which results in a value for d which is 11·1% higher.

---

* Equation (17) can also be applied to the case of flexurally vibrating narrow bars with two pairs of electrodes. For a bar with identical orientation to that of the longitudinal bar considered $(d=d_{31}')$: $N=\nu l^2/b$. For the fundamental mode, $\beta=(9\pi^2\tan^2\epsilon)/\epsilon^6$, where $\tan\epsilon+\tanh\epsilon=0$ $(\epsilon=2{\cdot}8650)$.

The solution of any mode comprises the distribution of the displacement and the resultant elastic modulus γ. If measured values of N and Γ are substituted in equation (18), the value of the piezoelectric coefficient d depends only on β and, provided d is known, the distribution of displacement can be checked. Similarly, equation (19) tests the accuracy of the approximation of γ, if the appropriate values of s_{ik} are known. Since equations (18) and (19) are only related by N, if the measured value of N is used, equation (18) still holds, even if the approximation of the solution for γ is not very close, or if the solution is affected by piezoelectric secondary effects.

§4. SELECTION OF SPECIMENS USED EXPERIMENTALLY

In order to check experimentally the formulae for the various modes on different crystals, particular orientations of plates and bars must be chosen, which fulfil the assumed conditions. Table 3 contains the orientations of plates and bars of sodium chlorate, sodium bromate, quartz, ammonium dihydrogen phosphate (ADP) and ethylene diamine tartrate (EDT), which were measured. Isolated vibrations of mode 3, excited by a field parallel to the thickness of a plate fulfilling the conditions (2) and (16), can only be obtained with crystals belonging to the cubic system.

Table 3. Materials and Specimens used for Measurement

Crystal system	Cubic	Trigonal	Tetragonal		Monoclinic	
Symmetry symbol	T	D_3	V_d		C_2	
Piezoelectric coefficient	d_{14}	d_{11}, d_{14}	d_{14}	d_{36}	d_{14}	d_{36}
Long. mode 1, 2 plate	$X_{0°, 45°}$	$Y_{\theta, 45°}$	$X_{0°, 45°}$	$Z_{0°, 45°}$	$X_{0°, 45°}$	$Z_{0°, 45°}$
Long. mode 3 plate	$P_{45°, 55°}$	—	—		—	
Long. mode bar	X_ψ	X_ψ	X_ψ	Z_ψ	X_ψ	Z_ψ
Shear mode plate	$X_{0°, 0°}$	$Y_{\theta, 0°}$	$X_{0°, 0°}$	$Z_{0°, 0°}$	$X_{0°, 0°}$	$Z_{0°, 0°}$
Crystal measured	sodium chlorate sodium bromate	quartz	ADP		EDT	

(i) *Explanation of the symbols of specimens used in Table* 3. Square plates $X_{0°, 0°}$ $Z_{0°, 0°}$, refer to plates, perpendicular to the X, Z axis with sides parallel to the other axes; square plates $X_{0°, 45°}$, $Z_{0°, 45°}$ are similar plates to the above with their diagonals parallel to the other axes. The symbols $Y_{\theta, 0°}$, $Y_{\theta, 45°}$ refer to square plates similar to the above, but rotated about the X axis through an angle θ in the notation of Bechmann (1942). The square plates $P_{45°, 55°}$ (used in the cubic system only) are plates which lie in the crystallographic plane (111), having one side in the coordinate plane. Narrow bars are denoted by X_ψ, Z_ψ, meaning that the length of the bar is in a plane perpendicular to the X, Z axis and rotated about this axis through an angle ψ, measured in an anticlockwise direction.

(ii) *Elastic and piezoelectric coefficients of the specimens.* The elastic and piezoelectric coefficients, determining the vibrational properties of the defined square plates, belonging to the cubic, tetragonal and monoclinic systems are given in Table 4 for shear modes and in Table 5 for longitudinal modes 1 and 2. In Table 5 the elastic coefficient s_{11}', which equals s_{22}', is obtained using the positive sign, and s_{12}' using the negative sign in the expressions in the third column. Thus it is obvious that $s_{11}'-s_{12}'=\frac{1}{2}s_{ii}$ ($i=4$ or 6). Primed symbols, used in the headings of Tables 4 and 5, distinguish the rotated cuts from the cut $Z_{0^\circ,\,0^\circ}$, on which Table 1 was based. For the rotated cuts, the symbols of the elastic constants in Table 1 should be read as primed and the expressions in Tables 4 and 5 are the corresponding transformation equations. The transformation equations for the plate $P_{45^\circ,\,55^\circ}$ in the cubic system are:

$$\left.\begin{array}{ll} s_{11}'=s_{22}'=\frac{1}{4}[2(s_{11}+s_{12})+s_{44}], & s_{16}'=s_{26}'=0, \\ s_{12}'=\frac{2}{3}s_{12}+\frac{1}{12}[2(s_{11}+s_{12})-s_{44}], & d=d_{31}'=d_{32}'=-\sqrt{3}\,d_{14}/6, \\ s_{66}'=\frac{2}{3}(s_{11}-s_{12}+s_{66}), & d_{36}'=0. \end{array}\right\} \quad \ldots\ldots(20)$$

Table 4. Transformation for Elastic and Piezoelectric Coefficients for Shear Mode

Symmetry	Cut	s_{11}'	s_{22}'	s_{12}'	s_{66}'	$d=d_{36}'$
T	$X_{0^\circ,0^\circ}$	s_{11}	s_{11}	s_{12}	s_{44}	d_{14}
V_d	$X_{0^\circ,0^\circ}$	s_{11}	s_{33}	s_{13}	s_{44}	d_{14}
	$Z_{0^\circ,0^\circ}$	s_{11}	s_{11}	s_{12}	s_{66}	d_{36}
C_2	$X_{0^\circ,0^\circ}$	s_{22}	s_{33}	s_{23}	s_{44}	d_{14}
	$Z_{0^\circ,0^\circ}$	s_{11}	s_{22}	s_{12}	s_{66}	d_{36}

$s_{16}'=s_{26}'=0;\quad d_{31}'=d_{32}'=0$

Table 5. Transformation for Elastic and Piezoelectric Coefficients for Longitudinal Modes 1 and 2

Symmetry	Cut	s_{11}' using + sign s_{12}' using − sign	s_{66}'	$s_{16}'=s_{26}'$	d $d_{31}'=-d_{32}'$
T	$X_{0^\circ,45^\circ}$	$\frac{1}{4}[2(s_{11}+s_{12})\pm s_{44}]$	$2(s_{11}-s_{12})$	0	$\frac{1}{2}d_{14}$
V_d	$X_{0^\circ,45^\circ}$	$\frac{1}{4}[s_{11}+s_{33}+2s_{13}\pm s_{44}]$	$s_{11}+s_{33}-2s_{13}$	$\frac{1}{2}(s_{33}-s_{11})$	$\frac{1}{2}d_{14}$
	$Z_{0^\circ,45^\circ}$	$\frac{1}{4}[2(s_{11}+s_{12})\pm s_{66}]$	$2(s_{11}-s_{12})$	0	$\frac{1}{2}d_{36}$
C_2	$X_{0^\circ,45^\circ}$	$\frac{1}{4}[s_{22}+s_{33}+2s_{23}\pm s_{44}]$	$s_{22}+s_{33}-2s_{23}$	$\frac{1}{2}(s_{33}-s_{22})$	$\frac{1}{2}d_{14}$
	$Z_{0^\circ,45^\circ}$	$\frac{1}{4}[s_{11}+s_{22}+2s_{12}\pm s_{66}]$	$s_{11}+s_{22}-2s_{12}$	$\frac{1}{2}(s_{22}-s_{11})$	$\frac{1}{2}d_{36}$

$d_{36}'=0$

The long expressions for the elastic coefficients of plates $Y_{\theta,\,0^\circ}$, $Y_{\theta,\,45^\circ}$ belonging to the trigonal system, symmetry class D_3 have not been included as they can be found in the author's paper (1942), but the piezoelectric coefficients as function of the angle θ in equations (16) are

$$\left.\begin{array}{l} \text{shear mode:} \\ \qquad d=d_{36}'=-2d_{11}\sin\theta\cos\theta+d_{14}\sin^2\theta, \\ \text{longitudinal modes 1 and 2:} \\ \qquad d=d_{31}'=-d_{32}'=-d_{11}\sin\theta\cos\theta+\frac{1}{2}d_{14}\sin^2\theta. \end{array}\right\} \quad \ldots\ldots(21)$$

The formulae for s_{11}' for longitudinally vibrating bars are well known; the values for s_{11}' for bars X_{45° and Z_{45° for the crystal classes T, V_d and C_2 are identical with those of plates $X_{0^\circ,\,45^\circ}$ and $Z_{0^\circ,\,45^\circ}$ as given in Table 5. The piezoelectric coefficients for these classes are

$$X_\psi\ \text{cut}: d=d_{31}'=d_{14}\sin\psi\cos\psi;\quad Z_\psi\ \text{cut}: d=d_{31}'=d_{36}\sin\psi\cos\psi \quad \ldots\ldots(22)$$

and for class D_3

$$X_\psi\ \text{cut}:\ d=d_{31}'=-d_{11}\cos^2\psi+d_{14}\sin\psi\cos\psi. \quad \ldots\ldots(23)$$

The values for γ_{ik} can be determined from Table 5, for example, these values for plates $Z_{0°,45°}$ symmetry class V_d (conditions (2)) can be written using equations (3)

$$\left.\begin{aligned} \gamma_{11}' = \gamma_{22}' &= \frac{1}{2}\,\frac{1}{s_{11}+s_{12}} + \frac{1}{s_{66}}, \qquad & \gamma_{66}' &= \frac{1}{2(s_{11}-s_{12})}, \\ \gamma_{12}' &= \frac{1}{2}\,\frac{1}{s_{11}+s_{12}} - \frac{1}{s_{66}}, \qquad & \gamma_{16}' &= \gamma_{26}' = 0, \end{aligned}\right\} \quad \ldots\ldots(24)$$

and for plates $Z_{0°,45°}$ symmetry class C_2 (conditions (4)) using equations (5)

$$\left.\begin{aligned} \gamma_{11}' = \gamma_{22}' &= \frac{1}{4}\,\frac{s_{11}+s_{22}-2s_{12}}{s_{11}s_{22}-s_{12}^2} + \frac{1}{s_{66}}, \qquad & \gamma_{12}' &= \frac{1}{4}\,\frac{s_{11}+s_{22}-2s_{12}}{s_{11}s_{22}-s_{12}^2} - \frac{1}{s_{66}}, \\ \gamma_{66}' &= \frac{1}{4}\,\frac{s_{11}+s_{22}+2s_{12}}{s_{11}s_{22}-s_{12}^2}, \qquad & \gamma_{16}' = \gamma_{26}' &= \frac{1}{4}\,\frac{s_{11}-s_{22}}{s_{11}s_{22}-s_{12}^2}. \end{aligned}\right\} \quad \ldots\ldots(25)$$

Similar expressions can be obtained for the other cuts mentioned in Table 5.

§ 5. EXPERIMENTAL RESULTS

Measurements of frequency and capacitance were made on a large number of specimens, as described in § 4, due heed being paid to remarks in § 6 of the author's previous paper (Bechmann 1950), which deals with the experimental technique. All specimens were silver plated on the main faces by evaporation and were held by spring clamps at their nodal points. The accuracy of the measurements is within the order of 0·2% for the capacitance and 0·02% for the frequency. All values given are average values based on sets of measurements on several specimens of various dimensions for each cut and are adjusted for 20° c.

The dimensions and units of the quantities in the following tables are: frequency constant N in kc/s. mm., elastic coefficient s_{ik} in 10^{-13} cm^2 dyne^{-1}, elastic modulus γ_{ik} in 10^{10} dyne cm^{-2}, piezoelectric coefficient d_{ik} in 10^{-8} C.G.S., E.S.U., and temperature coefficient of d_{ik}, (Td_{ik}) in 10^{-4}/°c.

5.1. *Piezoelectric Coefficients*

The piezoelectric coefficients derived from these measurements by formula (18) using the values for β in Table 2 are given in Table 6 which also includes the values for the density ρ in gm. cm^{-3}.

Table 6. Values of Piezoelectric Coefficients d_{ik} in 10^{-8} E.S.U. dyne^{-1} derived from Different Modes and their Temperature Coefficients Td_{ik} in 10^{-4}/° c.

Material	d_{ik}	Mode 1	Mode 2	Mode 3	Longitudinal mode, bar	Shear mode	Td_{ik}
$NaClO_3$ $\rho = 2{\cdot}490$	d_{14}	5·23	5·37	5·19	5·24	5·22	+80
$NaBrO_3$ $\rho = 3{\cdot}339$	d_{14}	7·77	7·97	7·75	7·77	7·68	+26·5
Quartz	d_{11}	6·93	6·88	—	6·95	6·78	−2·15
$\rho = 2{\cdot}654$	d_{14}	−2·18	−2·21	—	−2·20	−2·11	+12·9
ADP	d_{14}	5·27	5·43	—	5·44	5·20	−180
$\rho = 1{\cdot}803$	d_{36}	−145	−149	—	−145	−144	−28
EDT	d_{14}	−30·1	−29·8	—	−30·5	−29·9	−7·5
$\rho = 1{\cdot}538$	d_{36}	−55·1	−56·5	—	−55·6	−54·6	−15·2

(i) *Longitudinal mode* 1 *of square plates.* The solution for mode 1 is exact and as previously mentioned (Bechmann 1950) it is thought that the correct values of the piezoelectric coefficients are most likely to correspond with the results of this mode. The values obtained from the other modes are compared with them. The piezoelectric coefficients d_{11} and d_{14} for quartz are derived from formula (21) using various combinations of different orientations. The coefficients derived from this mode are independent of the orientation of the specimens. The observed values of CT cut quartz plates ($\theta = 128°$) and DT cut ($\theta = 38°$) are $d_{31}' = 2{\cdot}685 \times 10^{-8}$ and $d_{31}' = -3{\cdot}775 \times 10^{-8}$ respectively. The coefficients d_{14} and d_{36} for ADP have opposite signs as obtained from oblique cuts $X_{\theta,\,45°}$.

(ii) *Longitudinal mode* 2 *of square plates.* The values of the piezoelectric coefficients from mode 2 are about 2 to 3% higher than those from mode 1 with the exception of those of quartz plates which are 0·7 and 1·7% lower for DT and CT cuts respectively. The value for τ (defined in § 2 (ii)) for quartz CT cut is 0·07 and for DT cut 0·3; for all other measured plates τ is between 0·35 and 0·63 (see Table 8). The deviation appears to be slightly dependent on τ. Table 8 shows that the frequency constant N varies greatly with τ and differences between observed and calculated values for N are as large as 25% for the measured specimens, but the distribution function appears to be only slightly affected by τ. The values for the piezoelectric coefficients of quartz obtained from mode 2 depend to a small extent on the angles used for solving the combinations.

(iii) *Longitudinal mode* 3 *of square plates.* The values for the piezoelectric coefficients from mode 3 agree very well with those from mode 1. However, since for both materials, $\sigma = 0{\cdot}25$ (see Table 9) and according to Mähly (1945) the distribution of displacement appears to be slightly dependent on σ, it cannot be deduced that this good agreement holds for other values of σ. The results from the two measured crystals confirm Ekstein's distribution formula.

(iv) *Shear mode of square plates.* A comparison between the shear mode and mode 1 shows that the values of the piezoelectric coefficients from the shear mode are 0·5 to 2% lower. This difference appears to be a function of $\sqrt{\mu}$ and increases with increasing $\sqrt{\mu}$ (defined in § 2 (v)). For ADP plate $Z_{0°,\,0°}$, μ is 0·1 (see Table 11) and the difference between the shear mode and mode 1 is only 0·6%. As for mode 2, the values for the piezoelectric coefficients of quartz determined from this mode depend to a small extent on the angles of the specimens.

(v) *Longitudinal mode of narrow bars.* As can be seen from equations (22) the same piezoelectric coefficient can be determined from bars at different angles. For bars $X_{45°}$ of sodium chlorate and sodium bromate and bars $Z_{45°}$ of ADP a complete agreement exists with mode 1. These are the values given in Table 6, and the figures quoted for the other piezoelectric coefficients from this mode are average values. The value for d_{11} for quartz was obtained from narrow bars $X_{0°}$ (bars parallel to the Y axis). Observations have shown that values for the piezoelectric coefficients obtained from the longitudinal mode of narrow bars are slightly higher than those from mode 1.

For comparison, Table 7 contains values for the piezoelectric coefficients obtained dynamically by Mason for sodium chlorate and bromate (1946 b), for quartz (1943) and for ammonium dihydrogen phosphate (1946 a) and the static values for these crystals measured by Spitzer (1938).

(vi) *Temperature coefficients of piezoelectric coefficients.* Table 6 contains the temperature coefficients Td_{ik} of the piezoelectric coefficients d_{ik} obtained from

Table 7. Comparison of some Recently Published Values of Piezoelectric Coefficients d_{ik} in 10^{-8} E.S.U. dyne^{-1}

Material	d_{ik}	Spitzer	Mason	New values
$NaClO_3$	d_{14}	$-5{\cdot}23$	$6{\cdot}1$	$5{\cdot}23$
$NaBrO_3$	d_{14}	$-7{\cdot}27$	$8{\cdot}2$	$7{\cdot}77$
Quartz	d_{11}	$6{\cdot}94$	$6{\cdot}76$	$6{\cdot}93$
	d_{14}	—	$-2{\cdot}56$	$-2{\cdot}18$
ADP	d_{14}	$4{\cdot}53$	$5{\cdot}0$	$5{\cdot}27$
	d_{36}	$-136{\cdot}7$	148	-145

mode 1. They are average values in the temperature range 15 to 45°C. A summary of previous measurements of the temperature coefficient Td_{11} for quartz can be found in Cady (1946).* No published values for Td_{14} are known.†

The dependence of the temperature coefficients Td on the angle θ for quartz plates $Y_{\theta,45°}$ and on the angle ψ for narrow bars X_{ψ} is of practical interest as they determine the temperature coefficients of the elements of the equivalent electric circuit. The temperature coefficients, Td_{31}' for mode 1 of square plates derived from equation (21) and Td_{31}' for longitudinal mode of narrow bars, derived from equation (23) are shown in Figures 1 and 2 respectively. Zero points occur at $\theta = 47°$ for plates $Y_{\theta,45°}$ and at $\psi = 28°$ for bars X_{ψ}. For the DT cut ($\theta = 38°$) Td_{31}' is $-0{\cdot}5 \times 10^{-4}$ and for the CT cut ($\theta = 128°$) Td_{31}' is -6×10^{-4}. The values are also small for Td_{31}' for X_{ψ} cut quartz bars, near $\psi = 0$.

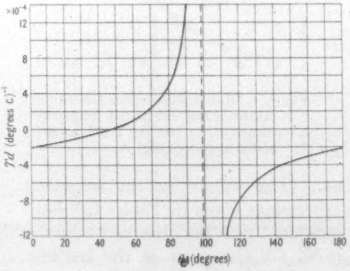

Figure 1. Temperature coefficient of the piezoelectric coefficient of square quartz plates $Y_{\theta,0°}$ and $Y_{\theta,45°}$ as function of the angle θ.

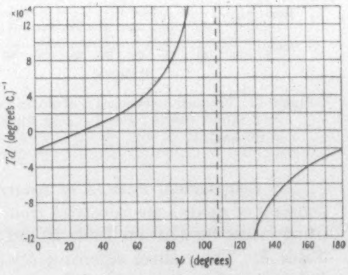

Figure 2. Temperature coefficient of the piezoelectric coefficient of narrow quartz bars X_{ψ} as function of the angle ψ.

5.2. *Frequencies of the Modes considered*

The frequencies of the various modes calculated from expressions in §2, in particular from Table 1, are compared with the measured values.

(i) *Longitudinal mode* 1 *of square plates.* From observed frequency constants of mode 1, the elastic shear coefficients s_{44}, s_{66} are determined and given in Table 8.

---

* The value for Td_{11} derived from Clay and Karper (1937) should be read as $-1{\cdot}1 \times 10^{-4}$ instead of -7×10^{-6}/°c.

† *Note added in proof.* Since this paper was written two papers have been published (*a*) by A. C. Lynch (*Proc. Phys. Soc.* B, 1950, **63,** 890) of this laboratory describing earlier work and (*b*) by R. V. Cook and P. G. Weissler (*Phys. Rev.*, 1950, **80,** 712) of the Bureau of Standards. The values for Td_{14} derived from the data given in the latter seem rather high.

But for quartz as plates rotated at angles $\theta=38°$ and $128°$ are used, the coefficients $s_{66}'=s_{66}\cos^2\theta+s_{44}\sin^2\theta-4s_{14}\sin\theta\cos\theta$ are given. Since the solution for mode 1 is exact and the conditions (2) or (4) are fulfilled for the measured specimens, the values for s_{44} and s_{66} are regarded as correct and the following calculations for the other modes are based on these values. Measured frequency constants for mode 1 for square quartz plates $Y_{\theta, 45°}$ as function of the angle θ have been published by the author (Bechmann 1942, Figure 5). In this paper, the frequency constant of mode 1 is denoted by N_2. The variation of frequency constant with θ for mode 1 has been recalculated with improved values for s_{ik} (see Table 10) and is plotted in Figure 3. The earlier observed values for the frequency constant have been taken from the paper mentioned and are shown in Figure 3 by circles. The agreement is very good and the earlier discrepancy between calculated and observed values has vanished. At the angles $\theta=91°$ and $153°$ the elastic coefficient s_{12}' is zero and changes its sign between these angles.

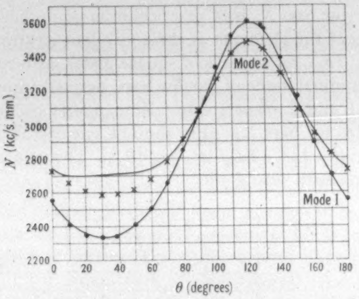

Figure 3. Frequency constants N of modes 1 and 2 of square quartz plates $Y_{\theta, 45°}$ as function of the angle θ.

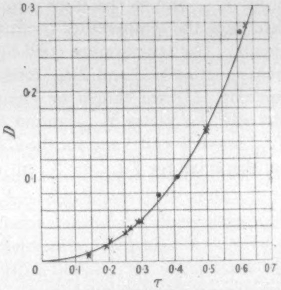

Figure 4. Relative difference D between observed and calculated frequency constants of mode 2 of square plates as function of τ.

(ii) *Longitudinal mode 2 of square plates.* The values for the frequency constant of mode 2 are calculated from the expressions given in Tables 1, 5 and 8 using values for s_{ik} from Table 10 and are compared with the observed values in Table 8. The relative difference $D=(N_{\mathrm{calc}}-N_{\mathrm{obs}})/N_{\mathrm{obs}}$ is given in the last line. It has been found that this difference D increases rapidly with increasing τ (see §2(ii)) as shown in Figure 4, where D is plotted against τ. The curve is an empirical approximation of the form $D=0{\cdot}5(\tau^2+\tau^4)$, which agrees with the observed values very well. The points marked by circles refer to values obtained from plates fulfilling conditions (2) and the crosses to values from plates fulfilling conditions (4). Earlier measurements of the frequency constant for square quartz plates $Y_{\theta, 45°}$ made by the author (Bechmann 1942, Figure 5) for mode 2 and denoted by N_4 are also included in Figure 3 and are shown by crosses. The frequency constant for mode 2 for these quartz plates has been calculated as a function of the angle θ with the given formula, using values of s_{ik} from Table 10 and is also plotted in Figure 3. The agreement for this mode with the observed values is very satisfactory for small values of τ ($\tau<0{\cdot}1$). Between $\theta=90°$ and $160°$, τ is less than 0·075. Between 10° and 60° there is a deviation which has its maximum at about $\theta=38°$ coinciding with the maximum of $\tau=0{\cdot}303$ the deviation at this point is 4·79%. The differences D for these quartz plates in the range 10° to 70° are included in Figure 4. Between $\theta=90°$ and 150° the frequency constant curves for mode 1 and 2 are interchanged, as s_{12}' changes its sign (§ 5.2, (i)).

Table 8. Data for Longitudinal Modes 1 and 2 of Square Plates
(N in kc/s. mm., s_{11} in $10^{-13}\,\mathrm{cm}^2\,\mathrm{dyne}^{-1}$, γ_{ik} in $10^{10}\,\mathrm{dyne\,cm}^{-2}$)

Material	NaClO$_3$	NaBrO$_3$	Quartz		ADP		EDT	
Cut	$X_{0°,45°}$	$X_{0°,45°}$	$Y_{38°,45°}$	$Y_{128°,45°}$	$X_{0°,45°}$	$Z_{0°,45°}$	$X_{0°,45°}$	$Z_{0°,45°}$
$2/(\gamma_{11}'-\gamma_{12}')=s_{ii}$	s_{44}	s_{44}	s_{66}'	s_{66}'	s_{44}	s_{66}	s_{44}	s_{66}
N_{obs} mode 1	1533	1510	2340	3572	1550	1298	1302	1303·$_5$
s_{ii} (i=4 or 6)	85·40	65·65	34·41	14·77	115·3	164·6	191·8	191·3
N_{obs} mode 2	1818	1746	2587	3459	1881	1636	1491	1595
γ_{11}'	39·72	47·28	78·15	127·3	41·54	31·08	18·17	20·91
γ_{12}'	16·30	16·82	19·93	−8·22	24·19	18·93	7·74	10·46
γ_{16}'	0	0	12·78	2·76	−9·80	0	−4·78	−0·64
τ	0·410	0·356	0·303	0·068	0·628	0·609	0·500$_7$	0·500$_8$
N_{calc} mode 2	1997	1882	2713	3463	2400	2074	1718	1843
D	0·0985	0·0776	0·0487	0·0012	0·276	0·268	0·152	0·156

(iii) *Longitudinal mode* 3 *of square plates.* Table 9 contains the values for s_{11}', s_{12}' and σ' for sodium chlorate and bromate for mode 3, derived from formulae (20), together with the frequency constants calculated from (*a*) expressions for γ given by Ekstein (Table 1) and (*b*) the author's expression (equation (7)), using the values of s_{ik} from Table 10. Also included are the observed values of N and the relative differences D compared with both calculated values (*a*), (*b*). From Mähly's Figure 1 (1945) these differences D are 0·95 and 2·9% respectively, giving a good agreement with the values in Table 9.

Table 9. Data for Longitudinal Mode 3 of Square Plates,
s_{ik} in 10^{-13} cm² dyne^{-1}. N in kc/s. mm.

Material	N_{obs}	s_{11}'	s_{12}'	σ'	N_{calc} (*a*)	N_{calc} (*b*)	D_a	D_b
$NaClO_3$	2040	30·28	−7·51	$0·248_0$	$2060._9$	$2100._0$	0·010	0·029
$NaBrO_3$	1970	24·21	−6·07	$0·250_7$	$1992._6$	$2031._6$	0·012	0·031

(iv) *Longitudinal mode of narrow bars.* The longitudinal mode of narrow bars was used for a new determination of the appropriate elastic coefficients s_{ik}; the results are given in Table 10. The values of s_{44} and s_{66} were derived from mode 1 and taken from Table 8. A comparison of these values with the other recently published values would lengthen this paper unnecessarily. The values of s_{ik} of EDT are given by Bechmann (1950).

Table 10. Summary of the New Values of Elastic Coefficients s_{ik} in 10^{-13} cm² dyne^{-1}

Material	s_{11}	s_{33}	s_{12}	s_{13}	s_{44}	s_{66}	s_{14}
$NaClO_3$	22·9	—	$-5·0_5$	—	85·4	—	—
$NaBrO_3$	20·4	—	−4·8	—	65·65	—	—
Quartz	12·77	9·60	−1·79	−1·22	20·00	29·13	−4·48
ADP	18·10	43·5	1·9	−11·8	115·3	164·6	—

(v) *Contour shear mode of square plates.* The observed values for the frequency constant N for the defined square plates are shown in Table 11. From these values s_{44}/Δ^2 or s_{66}/Δ^2 can be calculated using equations (10) and (19), where μ is the correction (10 *a*) stated by Mähly and Trösch. As the value of μ can be deduced from Table 10, Δ can be calculated and hence s_{44} or s_{66}. These values agree very well with the corresponding values obtained from mode 1 given in Table 8, showing that Mähly's formula gives a very close approximation to the solution.

Table 11. Data for Shear Mode of Square Plates, s_{ii} in 10^{-13} cm² dyne^{-1}
N in kc/s. mm.

Material	Cut	s_{ii}	$N_{\text{obs.}}$	s_{ii}/Δ^2	μ	Δ	s_{ii} corrected
$NaClO_3$	$X_{0°,0°}$	s_{44}	1362	90·29	0·2681	0·9740	85·66
$NaBrO_3$	$X_{0°,0°}$	s_{44}	1340	69·56	0·3107	0·9720	65·72
Quartz	$Y_{38°,0°}$	s_{66}'	2073	36·56	0·2984	0·9726	34·59
	$Y_{128°,0°}$	s_{66}'	3080	16·56	0·8155	0·9547	15·09
ADP	$X_{0°,0°}$	s_{44}	1383	120·9	0·2671	0·9741	114·7
	$Z_{0°,0°}$	s_{66}	1166	170·1	0·100	0·9841	164·8
EDT	$X_{0°,0°}$	s_{44}	1150	205·0	0·3564	0·9701	192·9
	$Z_{0°,0°}$	s_{66}	1166	199·5	0·1826	0·9786	191·0

ACKNOWLEDGMENTS

The author wishes to thank Mr. P. L. Parsons for carrying out measurements of capacitance on a large number of specimens, and Miss S. Rodwell for general measurements and assistance in composing the manuscript.

Acknowledgment is made to the Engineer-in-Chief of the General Post Office for permission to make use of the information contained in this paper.

REFERENCES

Bechmann, R., 1941, *Z. Phys.*, **117**, 180; 1942, *Ibid.*, **118**, 515; 1950, *Proc. Phys. Soc.* B, **63**, 577.
Cady, W. G., 1946, *Piezoelectricity* (New York : McGraw-Hill), p. 222.
Clay, J., and Karper, J., 1937, *Physica*, **4**, 311.
Ekstein, H., 1944, *Phys. Rev.*, **66**, 108.
Mähly, H., 1945, *Helv. phys. Acta*, **18**, 248.
Mähly, H., and Trösch, A., 1947, *Helv. phys. Acta*, **20**, 253.
Mason, W. P., 1934, *Bell Syst. Tech. J.*, **13**, 405; 1943, *Ibid.*, **22**, 178; 1946 a, *Phys. Rev.*, **69**, 173; 1946 b, *Ibid.*, **70**, 529.
Petrzilka, V., 1935, *Z. Phys.*, **97**, 436.
Spitzer, F., 1938, *Thesis*, Göttingen.
Voigt, W., 1910, *Lehrbuch der Kristallphysik* (Leipzig : Teubner).

An Absolute Measurement of the Susceptibility of Tantalum and other Metals

By F. E. HOARE and J. C. WALLING
Physics Laboratories, University of Leeds

MS. received 25*th August* 1950, *and in amended form* 6*th December* 1950

ABSTRACT. The magnetic susceptibility of tantalum has been determined absolutely, the value obtained for the mass susceptibility being $\chi_{\mathrm{Ta}}\times 10^6=0\cdot 8490\pm 0\cdot 0006$ at 20° c. Small specimens of tantalum have been used to determine, by a comparative method, the susceptibilities of specimens of platinum, palladium and rhodium at 20° c. The values obtained are : $\chi_{\mathrm{Pt}}\times 10^6=0\cdot 9712\pm 0\cdot 0007$, $\chi_{\mathrm{Pd}}\times 10^6=5\cdot 231\pm 0\cdot 004$, $\chi_{\mathrm{Rh}}\times 10^6=0\cdot 9903\pm 0\cdot 0008$. All specimens were prepared from spectrographically standardized materials.

§ 1. INTRODUCTION

In connection with an investigation of the susceptibility variation with temperature of the transition metals it was necessary to determine the absolute susceptibilities of small specimens approximately 7·5 mm. long and 4 mm. in diameter. With such small specimens it was advisable to adopt a comparative method rather than to attempt to determine the variation of field strength over a very limited range and thus evaluate the absolute force on a specimen in terms of susceptibility.

A search of the literature showed that tantalum was a suitable metal for comparative work over the range required, especially as it is relatively cheap even in a highly purified state. This metal has an additional advantage as a standard in that it possesses a very small temperature coefficient of susceptibility.

The only measurements on tantalum hitherto made appear to be those of Honda (1910) and Owen (1912) neither of whom was particularly concerned with absolute accuracy. Their results are quite widely different, Honda giving $\chi(18^\circ \text{c.}) = 0{\cdot}93 \times 10^{-6}$ and Owen $\chi(18^\circ \text{c.}) = 0{\cdot}81 \times 10^{-6}$. It was, therefore, necessary to make an accurate investigation of the susceptibility of this metal at room temperature.

§ 2. METHOD OF INVESTIGATION

A rod of spectrographically standardized tantalum 10 cm. long and 4·5 mm. in diameter was obtained from Messrs. Johnson, Matthey Ltd. The major impurities are given in the Appendix. The dimensions of the rod made the Gouy method the obvious choice for an absolute determination. The field distribution of the available magnet had, therefore, to be investigated as accurately as possible. The method of field measurement adopted was a modification of that employed by Nettleton and Sugden (1939). Field strengths were obtained ultimately in terms of an inductance, an electric current, and the absolute dimensions of a search coil. All the electrical apparatus was standardized at the National Physical Laboratory at the conclusion of the work. The measurements of search coil dimensions were made with standardized gauges. The magnetic field was held constant by regulation of the magnet current which was maintained constant to one milliampere by means of an automatic regulator designed and built by Mr. J. C. Matthews.

The remanent magnetism of the electromagnet used was rather high and an elaborate process of demagnetization was necessary between successive observations to obtain reliable results. The experimental criterion of satisfactory demagnetization was that the residual field should be less than three gauss between the pole pieces.

The field was measured along a symmetrical axis perpendicular to the line of the pole pieces for various excitation currents, the maximum being 5 amperes. Two search coils were used, it being found that the results thus obtained agreed to about one part in a thousand. The final results for the maximum field strengths were of the order of 10,000 gauss with a probable error (least squares) of ± 3 gauss. The smallness of the probable error indicates the internal consistency of the measurements.

§ 3. SUSCEPTIBILITY MEASUREMENTS

The Gouy method employed for the susceptibility measurements requires no detailed description. Weighings were made in terms of calibrated weights standardized against N.P.L. certified weights. A Sartorius balance was employed, the ratio of the arms being determined. The tantalum rod was very slightly tapered towards the centre of its length, necessitating a small correction in evaluating the susceptibility from the weighings. No variation of susceptibility with field strength was observed, indicating absence of ferromagnetic impurities. The mean of twenty-two independent measurements gave the volume susceptibility as $K \times 10^6 = 14{\cdot}171 \pm 0{\cdot}009$*.

To convert this to mass susceptibility an accurate value of the density is required. This was carefully measured using standard procedure and found to be $\rho(20^\circ \text{c.}) = 16{\cdot}691 \pm 0{\cdot}003$ gm.cm^{-3}. The value found by Keesom and Desirant (1941) is $\rho(17^\circ \text{c.}) = 16{\cdot}566 \pm 0{\cdot}01$ gm. cm^{-3}. The wide divergence in these results is not understood: the higher value is in close agreement with that from X-ray data.

---

[*] All errors quoted are by least squares, and where the result is dependent upon a previous result the error has been computed by a combination of errors in the standard manner.

With $\rho = 16{\cdot}691$ and atomic weight 180·88 the volume, mass and gramme atomic susceptibilities at 20° c., correcting by Honda's (1910) result are: $K \times 10^6 = 14{\cdot}171 \pm 0{\cdot}009$, $\chi \times 10^6 = 0{\cdot}8490 \pm 0{\cdot}0006$, $\chi_A \times 10^6 = 153{\cdot}57 \pm 0{\cdot}10$.

§ 4. THE MAGNETIC SUSCEPTIBILITIES OF PLATINUM, PALLADIUM AND RHODIUM

Measurements were also made on small cylinders (0·75 cm. long, 0·4 cm. diameter) of platinum, palladium and rhodium which had previously been used in an extensive series of measurements on the low-temperature variation of susceptibility of these metals. Each of these had been prepared from spectrographically standardized material. The major impurities are given in an Appendix. Values of their susceptibilities at room temperature were obtained by a direct comparison with tantalum. Two cylinders were turned off the tantalum rod, one from the middle and one from the end, to the same dimensions as the cylinders of the metals to be compared. No difference in the magnetic behaviour of these two tantalum specimens was detected.

Using a specially constructed holder the specimens were suspended in an inhomogeneous magnetic field and the force exerted on the specimen by the field was measured by direct weighing. A number of values of χ at different temperatures was obtained and corrected to 20° c. using unpublished results on temperature variation previously obtained in these laboratories. The following results were obtained, all at 20° c.: platinum, $\chi = (0{\cdot}9712 \pm 0{\cdot}0007) \times 10^{-6}$, palladium, $\chi = (5{\cdot}231 \pm 0{\cdot}004) \times 10^{-6}$, rhodium, $\chi = (0{\cdot}9903 \pm 0{\cdot}0008) \times 10^{-6}$. For none of these metals was there any evidence of variation of susceptibility with field strength, and it may be concluded that there was no ferromagnetic contamination. The palladium specimen was outgassed prior to the measurements by heating it *in vacuo* at 100° c. for several hours and then at 450° c. for a few minutes, the glass enclosure then being sealed off and allowed to cool. The actual measurements were made as quickly as possible and there was no evidence of any absorption of hydrogen during the weighing.

§ 5. COMPARISON WITH PREVIOUS WORK

To facilitate the comparison with the values obtained by other observers a number of results are summarized in the Table. The figures in brackets are the values at 20° c. computed by taking the variation of susceptibility per centigrade degree as $-0{\cdot}0007$, $-0{\cdot}010$ and $+0{\cdot}0003$ for platinum, palladium and rhodium respectively.

It is seldom that any statement of accuracy is made and hence in the Table the significant figures quoted are the same as those given in the original papers. In view of the wide scatter of the results it would be unprofitable to attempt to assign limits of accuracy to the published values.

Finke, Honda, Owen, Guthrie and Bourland all used torsional methods for susceptibility measurements, the first three making absolute measurements in terms of the field and its gradient. The determination of field gradient with a high degree of precision is difficult and consequently the order of agreement in the results of these investigators is not unsatisfactory. Guthrie and Bourland calibrated in terms of the susceptibility of water.

Onnes and Oosterhuis investigated the variation of susceptibility of platinum and palladium with temperature using what is essentially a weighing method. They state that in the case of platinum it was difficult to determine the susceptibility

	Susceptibility × 10^6		
Observer	Pt	Pd	Rh
Finke (1910)	1·054	5·478	1·031
Honda (1910)	1·097 (18° c.)	5·79 (18° c.)	1·14 (18° c.)
	(1·096)	(5·77)	(1·14)
Owen (1912)	0·80* (18° c.)	5·20 (18° c.)	1·08 (18° c.)
	(0·80)	(5·18)	(1·08)
Onnes and Oosterhuis (1913 and 1914)	0·973 (17·2° c.)	5·3 (18° c.)	—
	(0·971)	(5·28)	—
Föex (1921)	1·035 (17·1° c.)	5·264 (18·5° c.)	—
	(1·031)	(5·249)	—
Guthrie and Bourland (1931)	0·982 (25° c.)	5·15 (25° c.)	1·08* (25° c.)
	(0·986)	(5·20)	(1·08)
Wucher (1950)	—	5·338† (14·5° c.)	—
	—	(5·283)	—
	—	5·334 (13·6° c.)	—
	—	(5·270)	—
Hoare and Walling (1950)	0·971 (20° c.)	5·23$_1$ (20° c.)	0·990 (20° c.)

* Extrapolated to infinite field. † Specimen from Marret-Bonnin.

accurately owing to its small value, and for palladium the curve of temperature variation showed more irregularities than would have been expected considering the accuracy of the experiments.

Föex and Wucher each used a translational balance and standardized in terms of the susceptibility of solid manganese pyrophosphate which in turn was determined by comparison with solutions of manganese chloride of which the susceptibility was found by the ascension method. Whilst the two specimens of palladium used by Wucher gave values in satisfactory agreement at 20° c., the values differed by some 2% at 500° c. suggesting a physical or chemical difference in the specimens.

It is remarkable that for the specimens used in the above investigations, excluding the present work, in all but four cases the source of supply was the firm of Heraeus. The exceptions are one of Wucher's specimens, supplied by Marret-Bonnin, and those of Guthrie and Bourland which were supplied by the Bureau of Standards. The specimens used by Föex are stated to have been specially purified and free from iron. In the majority of the cases the susceptibility was investigated with various field strengths and the results of Owen (Pt) and Guthrie and Bourland (Rh) corrected to infinite field; no variation with field strength is noted in any other case where such an investigation is specifically mentioned. In no case is a spectrographic examination of the materials mentioned. Whilst it is not thought that the divergence in the results of later investigations is wholly attributable to impurities, it is considered that in work of this kind a spectrographic examination of the specimens used is well worth while.

ACKNOWLEDGMENTS

Our thanks are due to Professor R. Whiddington for his interest and for providing the facilities for this work, and Professor E. C. Stoner for useful discussion. Messrs. Johnson, Matthey undertook the special preparation of the small specimens and we are much indebted to them for their co-operation. One of us (J. C. W.) is in receipt of a grant from the Department of Scientific and Industrial Research which he wishes to acknowledge.

APPENDIX

Purity of Specimens used

The following abstract of reports and private communications on the spectrographically standardized material used lists only those impurities whose spectrum lines are clearly visible.

Tantalum. Columbium: 4100·923, 4079·729, 4058·938; nickel: all sensitive lines; tungsten: 4294·614, 4008·753. Columbium is the principal impurity. Tests on tantalum having the same source of origin might reasonably be quoted as indicating a typical and very approximate columbium content of 0·05%.

Platinum. No clearly visible lines. A quantitative assessment of some elements is given as follows: iron $<0{\cdot}001\%$, lead $<0{\cdot}001\%$, gold $\leqslant 0{\cdot}001\%$, palladium $\leqslant 0{\cdot}001\%$.

Palladium. Silver: 3382·891, 3280·683, strong lines. Total impurities not more than 0·002%.

Rhodium. Magnesium: 2852·129, 2802·695, 2795·53, copper: 3273·962, 3247·540. Total impurities not more than 0·002%.

REFERENCES

FINKE, W., 1910, *Ann. Phys., Lpz.*, **31,** 149.
FÖEX, G., 1921, *Ann. Phys., Paris*, **16,** 174.
GUTHRIE, A. N., and BOURLAND, L. T., 1931, *Phys. Rev.*, **37,** 303.
HONDA, K., 1910, *Ann. Phys., Lpz.*, **32,** 1027.
International Critical Tables, 1926, **2,** 456.
KEESOM, W. H., and DESIRANT, M., 1941, *Physica, s'Grav.*, **8,** 273.
NETTLETON, H. R., and SUGDEN, S., 1939, *Proc. Roy. Soc.* A, **173,** 313.
ONNES, K., and OOSTERHUIS, E., 1913, *Commun. Phys. Lab. Univ. Leiden*, **12,** No. 132e; 1914, *Ibid.*, **13,** No. 139e.
OWEN, M., 1912, *Ann. Phys., Lpz.*, **37,** 657.
WUCHER, J., 1950, *Thesis*, Strasbourg.

Thermal Instability of Contact Rectifiers: The Effect of the Constituent Materials on the Efficiency of a Rectifying Junction

By E. BILLIG

Research Laboratory, Associated Electrical Industries Ltd.,
Aldermaston, Berkshire

MS. received 17th October 1950, *and in amended form 14th January* 1951

ABSTRACT. If due allowance is made for the lowering by the image force of the height of the potential barrier in contact rectifiers, current–voltage characteristics can be calculated which are in good agreement with observed characteristics. On application of a voltage in the blocking direction, electrons (or holes) pass over the barrier owing to their thermal energy, the number of successful passes, i.e. the leakage current, being exponentially dependent on temperature. As the applied voltage is increased and the barrier lowered, the power loss corresponding to the increased leakage current will eventually raise the temperature in the thin barrier layer sufficiently to increase the current in turn until the cooling arrangement provided cannot cope with the increased power loss and the rectifier becomes thermally unstable. The conditions for this instability to arise are investigated quantitatively. Amongst other parameters such as mode of operation, cooling, etc., the conductivity of the semiconductor, and in particular the height of the potential barrier, have a paramount effect on the maximum voltage that can be withstood. The simultaneous requirements for large resistivity and barrier height severely restrict the choice of materials which can be used for efficient rectifiers.

IN the present development of contact rectifiers considerable efforts are being spent on purifying the semiconductor material used. The physical properties of semiconductors are rather sensitive to traces of impurities, but particularly so are the properties of the barrier layer which fundamentally affect the characteristics of a rectifying junction. Germanium as used for transistors or for high-back-voltage rectifiers is a case in point. This need for high-purity materials has long been felt but has not so far been substantiated by any theoretical argument.

According to the band theory of solids a potential barrier is set up at the junction of any n-type semiconductor* in contact with any metal of higher work function, and at the junction of any p-type semiconductor* in contact with any metal of lower work function (Angello 1949). In spite of the large number of metal–semiconductor combinations which should thus produce a barrier, practical contact rectifiers capable of rectifying reasonably large currents are confined to very few types; a somewhat larger number of metal–semiconductor combinations shows a certain amount of rectification when contact is made over a rather small area (point contact rectifiers).

With the recent development of the theory of rectification it has become possible to discuss this problem quantitatively. It has been shown in the diffusion theory of rectification (Billig 1951) that the height of the potential barrier V_d at the rectifying junction is reduced by the image force on the application of an inverse voltage $-U$ to a value

---

* An n-type semiconductor has 'donor levels' (easily ionized impurity centres) slightly below the conduction band, and conducts by free electrons, whilst a p-type semiconductor, with 'acceptor levels' above the full band, conducts by 'holes'.

$$\overline{V}=V_{\mathrm{d}}[1-\{(V_{\mathrm{d}}-U)/U_{\mathrm{c}}\}^{1/4}] \qquad \ldots\ldots(1)$$

where

$$U_{\mathrm{c}}=(\kappa/\mathbf{e})^{3}V_{d}^{4}/8\pi N \qquad \ldots\ldots(2)$$

is the critical voltage, application of which would reduce the barrier completely. Here, $\mathbf{e}$ is the electronic charge, κ the permittivity of the semiconductor and N the volume density of fixed space charges in the barrier region which is assumed to be uniform. Equation (2) holds for a space charge determined barrier (Schottky) to which the quantitative discussion below has been limited. Very similar results have been derived for a fully insulating (Mott) type of barrier.

The power lost per unit area by the flow of leakage current on application of the inverse voltage is

$$P=JU(U/V_{\mathrm{d}})^{3/8}\exp(-\overline{V}/W) \qquad \ldots\ldots(3)$$

where

$$J=\frac{\sigma\kappa}{\mathbf{e}}V_{\mathrm{d}}^{2}\left(\frac{2}{\pi}\frac{W}{V_{\mathrm{d}}-U_{\mathrm{c}}}\right)^{1/2}\left(\frac{V_{\mathrm{d}}-U_{\mathrm{c}}}{V_{\mathrm{d}}}\right)^{1/8} \qquad \ldots\ldots(4)$$

and the 'equivalent temperature potential' $W=\boldsymbol{k}T/\mathbf{e}$. The power loss heats the rectifier and the leakage current rises correspondingly. This process continues and may lead to one of two results: (i) The cooling provided is sufficient to dissipate the heat generated and the rectifier reaches a certain steady temperature at which it may continue to operate indefinitely. (ii) The power lost at any temperature exceeds the heat that can be dissipated at that temperature; leakage current and temperature rise in turn until they become excessive and permanent damage is done to the semiconductor or the counter electrode. For a circuit element such as a contact rectifier, in which the power loss varies exponentially with the temperature, the criterion for thermal stability sets a limit to the maximum permissible ***temperature***, the ***losses*** that can be dissipated at that temperature depending on the cooling arrangement.

The highest inverse voltage $-U_0$ that can be sustained indefinitely is obviously of great importance and the effects of various parameters on its magnitude are discussed below. For a particular, fairly representative, type of selenium plate rectifier operating under A.C., a maximum voltage $-U_0 \simeq 40$ volts was calculated (Billig 1951) which is in good agreement with practical experience. This value U_0 depends on various parameters, such as the operating conditions, type of load, ambient temperature, cooling arrangement, etc. In order not to confuse the issue we shall vary only one parameter at a time, for example when discussing the effect of the electrical conductivity of the semiconductor we maintain all other parameters entering the equations constant, in particular the height of the potential barrier, volume density of fixed space charges, heat dissipation, etc. This procedure is reasonable: potential barriers found at the junction of various combinations of semiconductors and metal electrodes are all of the same order of magnitude, say approximately 0·5 volt, and similarly space charge densities are of the order of 10^{17} to 10^{18} cm^{-3}.

We thus compare two rectifiers of identical size and construction, say of the plate type, but using different semiconductor materials: the electron mobility and hence the electrical conductivity σ_1 of one, say selenium, is low, about

2×10^{-5} ohm^{-1} cm^{-1}, and that, σ, of the other, say germanium, rather high*, about 2 ohm^{-1} cm^{-1}. According to equations (3) and (4) the power lost in the germanium plate rectifier under the same voltage would be proportionately higher, by a factor 10^5. If the selenium rectifier were stressed up to its limit ($-U_1 = 40$ volts, $-j_1 = 23$ ma/cm^2), the germanium rectifier under the same voltage, but with a leakage current 10^5 times higher, would immediately break down. To determine the maximum voltage U which the germanium rectifier could sustain indefinitely we maintain the critical temperature and thus the power loss fixed (at 0·92 watt/cm^2). This leads to the transcendental equation

$$(U/U_1)^{11/8} \exp[\alpha(U^{1/4} - U_1^{1/4})] = \sigma_1/\sigma, \quad \text{where} \quad \alpha = V_d/WU_c^{1/4}. \quad \ldots\ldots(5)$$

This has been solved for the type of rectifier considered above†, and the result is plotted in Figure 1 for a range of σ from 2 to 2×10^{-6} ohm^{-1}cm^{-1}. The voltage of the germanium plate rectifier would have to be reduced to 1·73 volts for continued safe operation.

Change in the type of metal used as counter electrode would affect the height of the barrier V_d. Again maintaining the power loss as well as all other parameters constant, we have this time to solve

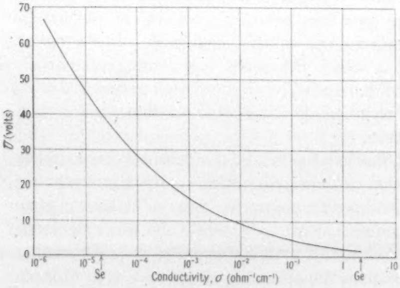

Figure 1. Effect of conductivity on limiting voltage.

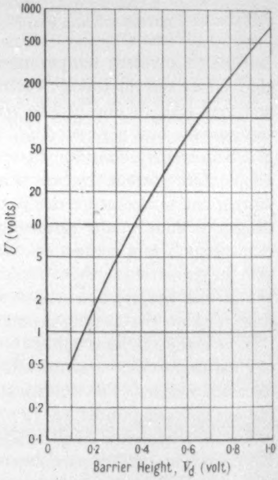

Figure 2. Effect of barrier height on limiting voltage.

$$(U/U_1)^{11/8} \exp[\beta(U^{1/4} - U_1^{1/4})] = (V_{d1}/V_d)^{3/2} \exp[(V_d - V_{d1})/W] \quad \ldots\ldots(6)$$

where $\beta = V_d/U_c^{1/4} = (\mathbf{e}/\kappa)^{3/4}(8\pi N)^{1/4}$. This has again been done for the selenium rectifier considered ($\sigma_1 = 2 \times 10^{-5}$ ohm^{-1} cm^{-1}) and the result is plotted in Figure 2 showing how strongly the limiting voltage is affected by a change in the height of the barrier. Actually the maximum temperature at which the rectifier can operate continuously is not independent of the barrier height, hence W in equation (6) is not quite constant; allowance for the corresponding change in the permissible power loss could easily be made, but the effect on the limiting voltage is relatively unimportant and has been neglected here.

---

* The large increase in conductivity is mainly due to the much higher mobility of the current carriers in germanium rather than to any large increase in their volume density.

† The values of the various parameters are $\sigma_1 = 2 \times 10^5$ ohm^{-1} cm^{-1}, $V_d = 0{\cdot}527$ volt, $U_c = 268$ volts, $U_1 = 40{\cdot}2$ volts, $\alpha = 5{\cdot}21$.

The way to overcome the difficulty of low stability inherent in the use of rather low resistivity semiconductors is to increase the effectiveness of the cooling arrangement. In practice this is done by reducing the contact area so that the power loss per unit *contact area* which can be dissipated by the rectifier is greatly increased. In the standard design of point contact rectifiers the cooling is in effect improved to such an extent that in spite of the greatly reduced contact area ($\sim 10^{-5}$ cm^2) a leakage current of about the same magnitude as in a selenium rectifier of 1 cm^2 contact area can be tolerated, the area being reduced in abtou the same ratio as the conductivity of the germanium is increased. The maximum voltage that can be withstood before instability sets in is even higher in some germanium point rectifiers than in selenium plate rectifiers. Turn-over voltages exceeding 100 v. have been obtained.

REFERENCES

ANGELLO, S. J., 1949, *Elect. Engng., N.Y.*, **68**, 865.
BILLIG, E., 1951, *Proc. Roy. Soc.* A, in the press.

The Role of the Self Magnetic Field in High Current Gas Discharges

BY P. C. THONEMANN AND W. T. COWHIG
Clarendon Laboratory, Oxford

MS. received 16*th October* 1950

ABSTRACT. It is shown that the self magnetic field of a high current discharge plays an important part in determining the radial electron density distribution. The effect of this magnetic field can be treated by adding a 'magnetic potential' term $V_{\mathrm{m}}=\int_0^r \bar{w}H\,dr$ to the electrostatic potential V_s in the Boltzmann equation for the radial electron density distribution, $\bar{w}$ being the longitudinal electron drift velocity. The drift of electrons and ions to the tube walls is equalized at low arc currents by a radial electric field. Since the magnetic field reduces the drift of electrons to the wall whilst having little influence upon the ions, increasing the arc current leads to a progressive reduction of the radial electric field. Probe measurements in an arc at low pressures show that at currents over 50 amperes, the radial electric field is zero except for a narrow sheath at the wall. The axial density is then mainly determined by the self magnetic field. A theoretical expression is derived for the equilibrium density distribution assuming a balance between the diffusion rates due to the concentration gradient and the magnetic forces. Experiments in a mercury vapour arc at high currents support this theory.

§1. INTRODUCTION

SYMBOLS USED: Suffix 1 refers to the electron, suffix 2 to the positive ion with m denoting mass, e charge, n number density, T temperature, V temperature in equivalent units of potential; $\boldsymbol{k}$ is Boltzmann's constant, $\bar{w}_1$ longitudinal electron drift velocity, V_s space potential, H_φ azimuthal magnetic field, V_{m} magnetic potential $\int_0^r \bar{w}_1 H_\varphi\,dr$, E radial electric field $-(dV_s/dr)$, F_1 radial force on an electron, V_w potential difference across wall sheath, p_0, p_1, p_2 neutral gas, electron and positive ion pressure, J_a total arc current, I_{2w} positive ion current density at the walls, $\bar{A}$ total cross-sectional area in unit volume of normal atoms obstructing diffusion. Unless otherwise stated all equations are in electromagnetic units. The temperature of the ions and the electrons will be defined by $\frac{1}{2}m\bar{c^2}=3\boldsymbol{k}T/2$, where $\bar{c^2}$ is the mean square random velocity. This kinetic theory definition of temperature is applicable whether or not the gas is in a steady state (Chapman and Cowling 1939), but coincides with the thermodynamic definition when the gas is in equilibrium.

Previous experimental investigations (Killian 1930) on the radial electron density and potential distribution in the positive column of an arc discharge have been confined to currents of less than 10 amperes. Tonks (1939) has attempted to calculate the density distribution in high current arcs using methods of conventional diffusion theory. However, at low pressures (i.e. less than 0·1 mm.Hg) where the positive ions fall radially towards the wall without making more than a few collisions with gas molecules, it is scarcely legitimate to assume that the ions have a Maxwellian velocity distribution. With increasing current, a diminution in the radial electric field may be expected, but until the energy gained per free path in this field is comparable with the thermal energies of the positive ions, diffusion methods are not applicable.

Because the electron drift velocity to the walls is at least an order of magnitude less than the thermal velocity it is possible to assume that the approach to the equilibrium density distribution is very close, and therefore Boltzmann's equation may be used to assess the importance of different potential fields, e.g. electrostatic, magnetic, gravitational, etc., in determining the electron density distribution.

The general equilibrium radial charge density distribution follows from the equation

$$\frac{d}{dr}(n_1\boldsymbol{k}T_1)+\left(\frac{dp_1}{dr}\right)_{\text{field}}=0. \qquad \ldots\ldots(1)$$

For example, at low pressures and currents, the only significant contribution to the $(dp/dr)_{\text{field}}$ term is that of the radial electric field. For T_1 constant, equation (1) then becomes

$$\boldsymbol{k}T_1\,dn/dr-n_1e_1E=0. \qquad \ldots\ldots(2)$$

Integration leads immediately to the Boltzmann relation:

$$n_1=n_{10}\exp(-e_1V_s/\boldsymbol{k}T_1) \qquad \ldots\ldots(3)$$

where V_s is the electrostatic potential difference between two regions of density n_1 and n_{10}.

Experimental results of Killian (1930) with a current of 5 amperes confirm this dependence of the charge density on the radial variation of potential. The correction introduced by considering the magnetic field of the arc current is negligible for this value of current. An example of the low current distribution is illustrated in the experimental section.

In this investigation it is assumed that the average potential energy of an electron increases towards the walls, due firstly to the electrostatic potential V_s, and secondly to a magnetic potential V_m. The magnetic potential arises from the interaction of the longitudinal flow of the electrons and the magnetic field of the arc current. At high currents it is shown experimentally that the variation of V_s across the greater part of the discharge cross section is negligible so that V_m is of major importance in controlling the density distribution.

§2. BOLTZMANN'S EQUATION WITH ELECTRIC AND MAGNETIC POTENTIALS

The contribution of the magnetic field to the $(dp/dr)_{\text{field}}$ term can be determined by considering the effective 'pressure' it exerts upon the electrons. In cylindrical coordinates with the current flow parallel to the axis, the radial force F_{1s} acting on a charge e_{1s} is

$$F_{1s} = +e_{1s}E - H_\varphi e_{1s} w_{1s}, \qquad \ldots\ldots(4)$$

where w_{1s} is its longitudinal component of velocity, E the radial electric field, H_φ the azimuthal magnetic field. The pressure dp_1 on an element of volume of thickness dr distant r from the axis containing n_1 charges per unit volume is

$$dp_1 = F_1\,dr = +n_1 E e_1 - n_1 e_1 H_\varphi \bar{w}_1, \qquad \ldots\ldots(5)$$

where $\bar{w}_1$ is now the average longitudinal drift velocity of the electrons at radius r. This is equivalent to defining $\bar{w}_1$ by the equation $I_1 = n_1 e_1 \bar{w}_1$ where I_1 is the drift current density in the discharge. Equation (1) now becomes:

$$-\frac{1}{n_1}\frac{dn_1}{dr} - \frac{1}{T_1}\frac{dT_1}{dr} + \frac{e_1 E}{\boldsymbol{k}T_1} - \frac{e_1 H_\varphi \bar{w}_1}{\boldsymbol{k}T_1} = 0. \qquad \ldots\ldots(6)$$

This mathematical procedure, though convenient, tends to obscure the fundamental processes. The equilibrium state is attained when the net rate of flow across any surface due to diffusion is zero. Thus the terms in equation (6) may be interpreted as follows: the first two terms are proportional to the velocity of diffusion of charges due to a concentration gradient dn_1/dr and a temperature gradient dT_1/dr and the third and fourth terms to the rate of transport of charges in the electric and magnetic fields. Integration of (6) leads to

$$\ln\frac{n_1}{n_{10}} + \ln\frac{T_1}{T_{10}} = \int_0^r \frac{e_1 E\,dr}{\boldsymbol{k}T_1} - \int_0^r \frac{e_1 H_\varphi \bar{w}_1\,dr}{\boldsymbol{k}T_1}, \qquad \ldots\ldots(7)$$

where $n_1 = n_{10}$ when V_s, $H_\varphi = 0$, and $T_1 = T_{10}$. The 'magnetic potential' is defined by

$$V_m = \int_0^r H_\varphi \bar{w}_1\,dr. \qquad \ldots\ldots(8)$$

When $T_1 = T_{10}$ everywhere (7) becomes

$$\ln\frac{n_1}{n_{10}} = -(V_s + V_m)\frac{e_1}{\boldsymbol{k}T_1}. \qquad \ldots\ldots(9)$$

Equation (9) can be written:

$$\frac{n_1}{n_{10}} = \exp\left[-\frac{e_1}{\boldsymbol{k}T_1}(V_s + V_m)\right]. \qquad \ldots\ldots(10)$$

Equation (10) has been formulated without any reference to either the positive ions or the neutral gas atoms and it is necessary to enquire under what conditions it is valid.

If the positive ions and the gas molecules are both in equilibrium under any potential fields which may be acting, the rate of flow of momentum across unit area is the same in opposite directions for each component. Thus no net momentum can be communicated to the electrons and no additional pressure gradient can arise. However, in most practical discharge tubes, ions are flowing to the walls, and neutral gas returning from the walls into the discharge space.

Since a neutral gas atom usually makes many collisions with the wall before it collides with an electron, it is just as likely to deliver momentum to an electron in one direction as in any other. It follows therefore that, unless the mean free path of a gas atom for collision with an electron is of the order of the tube radius, this factor may be ignored. The same argument applies to the positive ions drifting to the walls, viz. the free path for collision of a positive ion with an electron must be of the order of the tube radius before there is any tendency to deliver radial momentum to the electrons. At very high electron densities such as occur in the cathode spot of an arc or in a spark discharge, these factors may be important.

§3. EQUILIBRIUM ELECTRON DENSITY DISTRIBUTION AT HIGH CURRENTS

An equilibrium density distribution would result if there were no generation of charges and the boundaries were perfectly reflecting for both electrons and positive ions. If the net flux of particles is small compared with the random flux, the density distribution is, to a first approximation, an equilibrium one. This assumption is indeed made in the treatment of diffusion problems. A second approximation can be carried out to take into account a net flow of particles. In this section the equilibrium density distribution will be calculated assuming only a magnetic potential, as it is shown experimentally that the radial electric field is negligible across a large part of the discharge cross section.

The equations to be solved are

$$n_1 = n_{10}\exp(-e_1 V_{\mathrm{m}}/\boldsymbol{k}T_1), \qquad \ldots\ldots(11)$$

$$V_{\mathrm{m}} = \int_0^r \bar{w}_1 H_\varphi\,dr, \qquad \ldots\ldots(12)$$

$$H_\varphi = \frac{2J}{r} = \frac{4\pi}{r}\int_0^r n_1 e_1 \bar{w}_1 r\,dr. \qquad \ldots\ldots(13)$$

Measurements (to be published) on the axial electron drift velocity in a mercury arc as a function of the distance from the tube axis show that at pressures below 10^{-2} mm.Hg and currents up to 150 amperes (the highest used) the drift velocity and electron temperature are independent of radius. This result is to be expected when the mean free path for electron scattering is greater than the tube radius.

By differentiating (12) and (13), it is possible to eliminate H and to obtain a relation between n and r. This is:

$$\frac{d}{dr}\left(\frac{r}{n_1}\frac{dn_1}{dr}\right) + qn_1 r = 0, \qquad \ldots\ldots(14)$$

where $q = (4\pi e_1{}^2\bar{w}_1{}^2/\boldsymbol{k}T_1)$. Writing $x = \ln r/r_0$, and $y = n_1 r^2$ in (14) and integrating we obtain

$$\left(\frac{1}{y}\frac{dy}{dx}\right)^2 + 2qy = \text{constant}.$$

When $r = 0$, $y = 0$ and $(1/y)(dy/dx) = 2$, so that the value of the constant is 4. Separation of variables and integration then gives

$$\ln\frac{(1-\tfrac{1}{2}qy)^{1/2}-1}{(1-\tfrac{1}{2}qy)^{1/2}+1} = \ln p\frac{r^2}{r_0{}^2}, \qquad \ldots\ldots(15)$$

where p is a constant. With $n_1 = n_{10}$ at $r = 0$ this becomes $n_1 = n_{10}/(1 + pr^2/r_0{}^2)^2$ where

$$p = qn_{10}r_0{}^2/8 = \pi e_1{}^2\bar{w}_1{}^2 n_{10} r_0{}^2/2\boldsymbol{k}T_1. \qquad \ldots\ldots(16)$$

The total arc current J_a is

$$J_a = 2\pi \int_0^{r_0} n_1 e_1 \bar{w}_1 r \, dr = \pi e_1 \bar{w}_1 n_{10} r_0^2/(1+p).$$

Thus the axial electron density expressed in terms of the arc current is

$$n_{10} = \frac{J_a}{\pi e_1 \bar{w}_1 r_0^2 - \frac{1}{2}\pi J_a r_0^2 e_1^2 \bar{w}_1^2/\boldsymbol{k}T_1}. \qquad \ldots\ldots(17)$$

Eliminating n_{10} from p in equation (16) yields the final solution:

$$\frac{n_1}{n_{10}} = \left[1 + \left(\frac{\frac{1}{2}J_a e_1 \bar{w}_1}{\boldsymbol{k}T_1 - \frac{1}{2}J_a e_1 \bar{w}_1}\right)\frac{r^2}{r_0^2}\right]^{-2}. \qquad \ldots\ldots(18)$$

The average electron density $\bar{n}_1$ is simply $n_{10}/(1+A)$ where

$$A = \tfrac{1}{2}J_a e_1 \bar{w}_1/(\boldsymbol{k}T_1 - \tfrac{1}{2}J_a e_1 \bar{w}_1).$$

In practical units, equation (18) is:

$$\frac{n_1}{n_{10}} = \left[1 + \left(\frac{J_a \bar{w}_1}{2 \times 10^9 V_1 - J_a \bar{w}_1}\right)\frac{r^2}{r_0^2}\right]^{-2}, \qquad \ldots\ldots(19)$$

where J_a is in amperes, $\bar{w}_1$ in cm/sec., V_1 in volts, and r in centimetres. n_1/n_{10} is plotted as a function of r for various values of the parameter A in Figure 1.

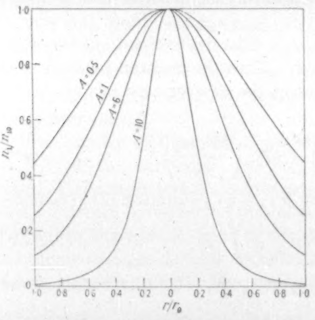

Figure 1.

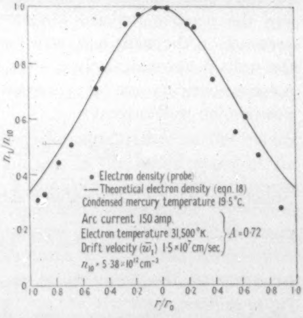

Figure 2.

A comparison between the theoretical and experimentally determined electron density distribution is shown in Figure 2. The scales have been adjusted so that $(n_{10})_{\text{exp}} = (n_{10})_{\text{theor}}$. Equation (17) in practical units is

$$n_{10} = \frac{1{\cdot}99 \times 10^{18} J_a}{\bar{w}_1 r_0^2(1 - 5 \times 10^{-10} J_a \bar{w}_1/V_1)}. \qquad \ldots\ldots(20)$$

It is interesting to note that as $J_a\bar{w}_1 \to 2 \times 10^9 V_1$, $n_{10} \to \infty$ implying that the arc tends to contract into a narrow streamer at the tube axis. This behaviour may be compared with that termed by Tonks the 'pinch effect'. With increasing arc current, T_1 is generally observed to decrease whilst $\bar{w}_1$ remains constant. If the discharge is to remain stable, this tendency must change in the neighbourhood of the critical current. If the degree of ionization approaches 100% the drift velocity is determined mainly by the positive ion scattering and both T_1 and $\bar{w}_1$

increase with increasing current (Mohler 1938) and it is not possible to decide whether the discharge will remain stable without a more detailed analysis.

§ 4. THE RADIAL STEADY STATE MOMENTUM BALANCE

In a strictly equilibrium state the net rate of flow of momentum across any area is zero. In a plasma, however, ions and electrons are continuously generated and, in the absence of appreciable volume recombination, recombine on the tube walls. Consequently, in the steady state there is a radial flow of momentum. The ratio of the momentum carried by the positive ions to that carried by the electrons is m_2/m_1, since the drift velocities are equal (ambipolar drift). The contribution of the electrons will therefore be neglected.

The potential difference across the space charge sheath at the walls is $V_w = \frac{1}{2}V_1 \ln(m_2V_1/m_1V_2)$. Thus even if $V_2 = V_1$, the ions gain a greater part of their radial momentum in the wall sheath ($V_w \simeq 6V_1$ for mercury ions).

At gas pressures where the free path for ion–gas atom collisions is small compared with the tube radius, the ions transfer their momentum to the neutral gas and set up a radial gas pressure gradient. The momentum gained by the positive ions is then transferred to the walls by the neutral atoms. In this case it has been shown (Steenbeck 1939) that the difference in gas pressure between the walls and the tube axis is given by $p_0(\text{walls}) - p_0(\text{axis}) = n_{10}\boldsymbol{k}T_1$. In the low pressure case, the rate of transfer of momentum by the positive ions is $n_2m_2\bar{v}_2^2$, and the positive ion wall current density is $I_{2w} = n_2e_2\bar{v}_2$. Thus the resultant pressure on the walls is $p_2(\text{walls}) = m_2I_{2w}\bar{v}_2/e_2$. The drift velocity of the ions at the walls is approximately $\bar{v}_2 = (2e_2V_w/m_2)^{1/2}$. Thus the electron pressure at the plasma boundary can be expressed in terms of the electron temperature and the positive ion wall current:

$$n_{1w}\boldsymbol{k}T_1 = \frac{m_2I_{2w}}{e_2}\left(\frac{2e_2V_w}{m_2}\right)^{1/2} = I_{2w}\left(\frac{2V_wm_2}{e_2}\right)^{1/2}. \qquad \ldots\ldots(21)$$

Substituting for V_w from above and writing $\boldsymbol{k}T_1 = e_1V_1$ equation (21) becomes

$$n_{1w} = \frac{I_{2w}}{V_1^{1/2}}\frac{1}{e_2}\left(\frac{m_2}{e_2}\ln\frac{m_2V_1}{m_1V_2}\right)^{1/2}. \qquad \ldots\ldots(22)$$

Inserting the constants for mercury and putting $V_1 = V_2$ this becomes, with I_{2w} in milliamps,

$$n_{1w} = 3{\cdot}2\times10^{11}I_{2w}/V_1^{1/2}. \qquad \ldots\ldots(22a)$$

At high currents, the electrons experience an inward force due to the self-magnetic field whereas the ions are little affected, and the axial electron pressure is greater than that given by equation (21). With $n_1 = n_{1w}$ at $r = r_0$ equation (18) gives

$$\begin{aligned} n_{10} &= I_{2w}\left(\frac{m_2\ln(m_2V_1/m_1V_2)}{e_2V_1}\right)^{1/2}\left[1 + \frac{\frac{1}{2}J_a\bar{w}_1}{V_1 - \frac{1}{2}J_a\bar{w}_1}\right]^2 \\ &= 3{\cdot}21\times10^{11}\frac{I_{2w}}{V_1^{1/2}}\left[\frac{2\times10^9V_1}{2\times10^9V_1 - J_a\bar{w}_1}\right]^2, \qquad \ldots\ldots(23) \end{aligned}$$

for mercury ions, and with I_{2w} in milliamps, J_a in amperes, V_1 in volts, and $\bar{w}_1$ in cm.sec^{-1}.

§ 5. APPARATUS

Measurements were carried out in a Pyrex tube about one metre long and 54 mm. internal diameter (Figure 3). A hollow graphite anode about 4 in. long and $1\frac{1}{2}$ in. diameter was used in most of the experiments, but it was later replaced by a water-cooled nickel-plated copper anode A to enable the tube to be run at higher arc currents. A′ is a small nickel anode used as 'keep alive', through which a constant current of about 2 amp. is passed. The cathode C consists of a mercury pool through the surface of which projects a $\frac{3}{4}$-in. diameter nickel cylinder used to fix the cathode spot. Probe readings are found to vary erratically when the spot is allowed to wander. A conical nickel shield B prevents direct streams of mercury vapour from the cathode spot entering the main length of the tube. The arc is started by applying a Tesla coil to a tungsten wire sealed through the tube T.

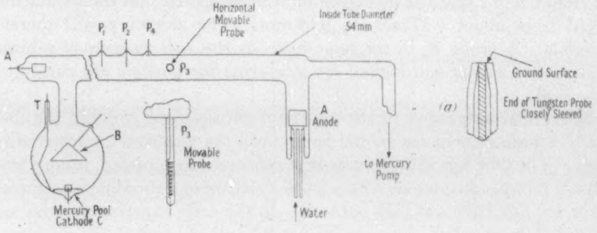

Figure 3.

The spherical cathode compartment and half the neck are immersed in a vessel of water which is continuously stirred. The temperature of the water can be adjusted to any value in the range 0 to 40° c. by means of a copper cooling coil through which refrigerant liquid is passed from a thermostatically controlled refrigerator unit.

The density of the neutral gas in the tube was calculated from the vapour pressure of the condensed mercury corresponding to the temperature of the water. If the mean free path of the neutral gas is small compared with the diameter of the aperture between the cathode compartment and the tube, the pressure at the wall in the tube is equal to the vapour pressure of the condensed mercury, and the neutral gas density at the wall near the probe is T_B/T_W multiplied by the density corresponding to the condensed mercury temperature. If, however, this mean free path is comparable with or greater than the diameter of the aperture, thermal effusion will lead to a difference of pressure in the two regions and the pressure in the tube will be a factor $(T_W/T_B)^{1/2}$ higher than that in the bulb, and the density therefore a factor $(T_B/T_W)^{1/2}$ lower than that in the bulb. A heater wire is wound around the side arm P_3 so that when necessary its temperature can be raised above room temperature to prevent mercury from condensing in it. The electric field in the column is calculated from the difference in the floating potentials of the two probes P_1 and P_2 which are spaced a known distance (11·85 mm.) apart. The plane collecting surfaces of the two probes are on the axis of the tube. A simple arrangement can be used for backing off the difference between their floating potentials against the voltage across a potentiometer, with a galvanometer to show equality. The electric field can therefore be obtained at any moment from the reading of the voltmeter across the potentiometer. This was checked by taking the complete probe characteristics of P_1 and P_2 and deriving the difference in space potentials at the two points in the usual manner. A movable probe P_3 is used to measure electron densities and space potentials at any point in the cross section of the column. The collecting surface of P_3 is plane. The probe is made by sleeving a $1\frac{1}{2}$ mm. tungsten rod with vitreous silica tubing, the end of which was drawn down so that, with the rod in position, the end could be carefully ground plane with carborundum powder (Figure 3 (*a*)). In this manner, the collecting area of the probe is accurately defined except for a small error arising from the finite thickness of the positive ion sheath on the glass wall which tends to screen the probe from electrons approaching at small angles to the plane of the probe. Over the range of conditions used in these experiments, the positive ion wall currents were of the order 0·5 to 5·0 ma/cm², and from Child's space charge equation it is calculated that the sheath thickness ranged from about 0·17 mm. to 0·04 mm. The shielding will therefore be negligible. A probe P_4 in the same plane as the wall consists of a nickel disc 0·95 cm. in diameter and is used for measuring the positive ion current density at the wall.

The initial outgassing of the apparatus consisted of running the discharge tube at a high current for several hours until the electrical characteristics were steady. The tube was subsequently kept continuously pumped, using a two-stage mercury pump. Inspection with a small spectroscope showed no impurity lines except sodium vapour at high currents. In the early experiments, the tube was pumped through a $\frac{3}{4}$-in. diameter tube at the cathode end of the discharge tube and the rate of pumping limited the attainable arc current. Moreover, it was found that impurities tended to accumulate at the anode region due to the pumping action of the longitudinal electron drift current. The pumping tube was therefore removed to the anode end of the discharge tube (see Figure 3) and its diameter increased to $1\frac{1}{4}$ in.

§ 6. MEASUREMENTS

It will be seen from equations (12) and (13) that the magnetic potential V_m is directly proportional to the square of the axial drift velocity $\bar{w}_1$ and it is therefore important to evaluate this parameter as accurately as possible, if a reasonable agreement with theory is to be expected. The most direct method would appear to be the use of the equation (11) for the total arc current J_a in terms of the electron density distribution across the arc and the drift velocity $\bar{w}_1$ although this is dependent upon the accuracy of the absolute value of peak electron density. Complete probe characteristics of voltage and current were taken at about ten positions traversing the arc. Correction for positive ion current was made when necessary and the plots on semi-logarithmic graph paper were linear over a wide range. Values of electron density n_1 and space potential V_s were obtained in the usual manner from these curves. The drift velocity could then be obtained from these data by graphical integration. These values of drift velocity were found to be in reasonable agreement with values obtained using the Langevin mobility expression

$$\bar{w}_1 = \tfrac{3}{8}\pi^{1/2} \frac{e_1 X}{(2m_1 \boldsymbol{k} T_1)^{1/2}} \frac{1}{\bar{A}},$$

where $\bar{A}$ is the averaged cross section for electron collision assuming a Maxwellian velocity distribution corresponding to an electron temperature T_1, and X is the longitudinal electric field. This averaged cross section was computed using data from Brode (1929) for the variation of the cross section of electrons of uniform energy and by integrating over the Maxwellian velocity distribution as described by Killian (1930).

The results of the probe characteristics taken at arc currents of 5 amp. and 50 amp. are shown in Figures 4 and 5 respectively. It will be seen from Figure 4 that, the space potential V_s, plotted in units of V_1 where $V_1 = \boldsymbol{k}T_1/e_1$, is of the expected parabolic shape, whereas in Figure 5, for the high arc current, the space potential has become uniform over the arc except at the walls. The lack of symmetry in the curves about the axis is probably due to the self-shielding of the probe as it approaches the far wall of the tube. Equation (9) may be written $\ln(n_1/n_{10}) = |(V_s + V_m)/V_1|$. When the magnetic term is zero, the space potential curve should be coincident with a curve of $\ln(n_1/n_{10})$. This is shown with good agreement in Figure 4 for an arc current of 5 amperes where the magnetic potential term is very small (two points at the walls with the computed magnetic correction are shown). In Figure 5 (50 amperes arc current) there is a wide deviation in the $\ln(n_1/n_{10})$ plots, but a plot of $(V_s + V_m)/V_1$ brings the agreement considerably closer. If a slightly higher drift velocity had been assumed, an even better agreement with the theory would have been attained.

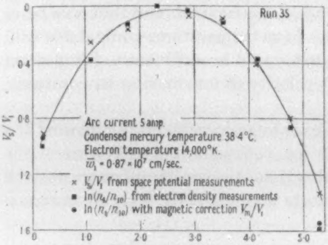

Figure 4. Radial variation of electrostatic potential compared with that computed from electron density distribution at low arc current.

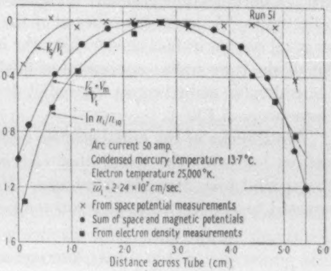

Figure 5. Radial variation of electrostatic and magnetic potentials compared with that computed from density distribution at high arc current.

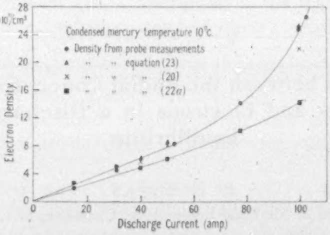

Figure 6. Comparison of measured axial electron density with that computed from equations (20), (22 *a*) and (23).

In Figure 6 the variation of axial electron density as measured by a probe is shown as a function of arc current. It departs considerably from the linear relation predicted by low current theory (Tonks and Langmuir 1929). Much better agreement is obtained on the basis of the magnetic potential theory using equation (20), and this is further improved by using equation (23) which incorporates a value of electron density at the wall deduced from radial momentum considerations. Figure 6 also includes a plot of the electron density at the plasma boundary (equation (22 *a*)) for reference.

§7. DISCUSSION

As the arc current increases, the magnetic field becomes more and more important in reducing the radial drift of electrons and the radial electric field which maintains ambipolar drift at low currents decreases until it is effectively zero. Concentration gradient diffusion is then responsible for ambipolar drift to the walls. A detectable reversal of the radial electric field (and thus a negative arc core) cannot in fact occur whilst the ions have temperatures comparable with that of the tube walls: a reversal of 0·04 volt would be sufficient to bring about a considerable reduction in the radial drift velocity of ions having an equivalent temperature of 100° c.

The absence of the radial electric field leads to an increase in the lifetime of a positive ion with the result that electron–ion collisions and collisions of the second kind may increase its energy. If this is so, the ion temperature may be expected to approach the electron temperature at sufficiently high arc currents.

ACKNOWLEDGMENT

The authors are grateful to Professor Lord Cherwell for his interest and encouragement.

REFERENCES

Brode, W. R., 1929, *Proc. Roy. Soc.* A, **125**, 134.

Chapman, S., and Cowling, T. G., 1939, *Mathematical Theory of Non-uniform Gases* (Cambridge : University Press).

Killian, J., 1930, *Phys. Rev.*, **35**, 1238.

Mohler, F. L., 1938, *J. Res. Nat. Bur. Stand., Wash.*, **21**, 873.

Rompe, R., and Steenbeck, M., 1939, *Ergebn. Exakt. Naturw.*, **18**, 270.

Steenbeck, M., 1939, *Z. Phys.*, **113**, 526.

Tonks, L., 1939, *Phys. Rev.*, **56**, 360.

Tonks, L., and Langmuir, I., 1929, *Phys. Rev.*, **34**, 876.

The Relationship between the Radial Concentration Variations of excited Atoms and Electrons in a Discharge in Thermal Equilibrium

By H. EDELS

Department of Electrical Engineering, University of Liverpool

Communicated by J. D. Craggs; MS. received 3rd November 1950

ABSTRACT. The excitation and Saha equations applicable to gaseous electrical discharges in thermal equilibrium are used to obtain convenient expressions for calculating the radial concentration variations of electrons and excited atoms when the radial intensity variation of one spectral line is known, and when the temperature on the axis of the discharge can be estimated.

§ 1. INTRODUCTION

In most cases electron concentrations in gaseous electrical discharges are obtained as mean values of the whole of the discharge cross section. For a more detailed study of such problems as Stark effect, the effect of positive ions on electron mobility, and current densities, or self absorption, a knowledge of the spatial variation of electron concentration is required (see for example Schulz 1947, Edels to be published). The measurement of such a spatial variation is by no means simple, although it may be obtained for example from Stark effect investigations on radially symmetric discharges if the radial intensity variation of the spectral line under investigation is known (Grimley and Saxe, to be published, Hopwood, Craig and Craggs, to be published). However, if such an intensity variation has been obtained it is a relatively simple matter to derive either the radial intensity variation of another spectral line, or the radial variation of electron concentration if the discharge is assumed to exist in thermal equilibrium.

The assumption of thermal equilibrium in a gaseous electrical discharge in effect postulates that the energy gained by the charge carriers from the electrostatic field between the electrodes is passed on by collision to the neutral particles in the discharge to such an extent that the energy of all types of particle is distributed according to the Maxwell–Boltzmann law with the same temperature, that is with the same mean kinetic energy. Since energy transport is continually taking place in the discharge, thermal equilibrium cannot be complete, and in effect a difference between the temperature of the electrons and ions and the other particles must exist. However, for many discharges with a high gas density there is considerable theoretical and experimental evidence to show that this temperature difference is small, and in such cases thermal equilibrium may be assumed as a close approximation. With such a discharge the radial energy transport can also be assumed to have only a small effect on the energy distribution of the particles, so that in each small volume of the discharge the Maxwell–Boltzmann distribution is maintained at a temperature characteristic of the spatial position of the considered volume. The radial energy transport is then associated with a radial temperature distribution to which the formulae of thermal equilibrium may be applied. For a further discussion of this problem and a description of the theory and experiments associated with the subject reference may be made to a report on the temperatures of an electrical discharge in a gas and to the references cited there (Edels 1950). In a discharge in which thermal equilibrium is assumed, both the radial spectral intensity and electron concentration variations are functions of the common radial temperature distribution, through which they may be related. The relationships so obtained are developed in the following section.

§ 2. RADIAL RELATIONSHIPS IN A DISCHARGE IN THERMAL EQUILIBRIUM

We consider an atom having energy levels s, t, i (the ionization level), such that the magnitudes of the energies to the ground state p are given by $\boldsymbol{h}\nu_{\mathrm{sp}} < \boldsymbol{h}\nu_{\mathrm{tp}} < \boldsymbol{h}\nu_{\mathrm{i}}$. We assume now that the intensity of radiation at a radius r obtained by transition from level s to some lower state is known as a fraction of its intensity at the discharge axis and is given by F. We wish then to obtain the radial variation of radiation intensity f of a transition from level t, and the electron concentration variation g as functions of F. It will be appreciated that the radial variation of the level populations will also be given by F and f.

For a discharge in thermal equilibrium the intensity of radiation of the frequency ν_{sp} at r is given by the excitation equation as

$$J_{\mathrm{sp}} = N_{\mathrm{p}} \frac{g_{\mathrm{s}}}{g_{\mathrm{p}}} \boldsymbol{h}\nu_{\mathrm{sp}} A_{\mathrm{sp}} \exp\left[\frac{-\boldsymbol{h}\nu_{\mathrm{sp}}}{\boldsymbol{k}T_r}\right] \qquad \ldots\ldots(1)$$

where N_{p} is the concentration of atoms in the ground state, g_{s} and g_{p} are the statistical weights of the states s and p, A_{sp} is Einstein's probability of spontaneous transition between the two states, and T_r is the temperature at r. Ornstein and Brinkman (1934) derive and discuss the validity of this equation and its applications to arc discharges.

If the temperature at the discharge axis is taken as T_0 from equation (1), then the radial variations of intensity are given by

$$F = \frac{T_0}{T_r}\left\{\exp\left[\frac{-\boldsymbol{h}\nu_{\mathrm{sp}}}{\boldsymbol{k}T_0}\left(\frac{T_0}{T_r}-1\right)\right]\right\}, \qquad \ldots\ldots(1\,a)$$

$$f = \frac{T_0}{T_r}\left\{\exp\left[\frac{-\boldsymbol{h}\nu_{\mathrm{tp}}}{\boldsymbol{k}T_0}\left(\frac{T_0}{T_r}-1\right)\right]\right\}. \qquad \ldots\ldots(1\,b)$$

Now Saha has shown (1920, 1921, 1923) that for a gaseous volume at r in thermal equilibrium, a relationship between the electron concentration N_{e}, concentrations of positive ions N_+ and neutral atoms N_{a} and the temperature may be obtained. This relationship, developed by Fowler (1929), is

$$\frac{N_{\mathrm{e}}N_+}{N_{\mathrm{a}}} = \frac{g_{\mathrm{e}}(2\pi \boldsymbol{m})^{3/2}}{\boldsymbol{h}^3}(\boldsymbol{k}T_r)^{3/2}\frac{U_{\mathrm{i}}(T)}{U_{\mathrm{a}}(T)}\exp\left[\frac{-\boldsymbol{h}\nu_{\mathrm{i}}}{\boldsymbol{k}T_r}\right], \qquad \ldots\ldots(2)$$

where g_{e} and $\boldsymbol{m}$ are the statistical weight and mass of the electron, and $U_{\mathrm{i}}(T)$ and $U_{\mathrm{a}}(T)$ are functions containing the statistical weights and partition terms of the energy states of the ions and atoms respectively. From this equation, assuming a neutral plasma ($N_{\mathrm{e}} = N_+$), we can derive the function g as

$$g = \left(\frac{T_r}{T_0}\right)^{1/4}\left\{\exp\left[\frac{-\boldsymbol{h}\nu_{\mathrm{i}}}{2\boldsymbol{k}T_0}\left(\frac{T_0}{T_r}-1\right)\right]\right\}. \qquad \ldots\ldots(2\,a)$$

The derivation and validity of equations (1) and (2) is given by Edels (1950).

The derivations of equations (1 *a*), (1 *b*) and (2 *a*) assume a constant pressure discharge which is applicable in the majority of cases. For the early period of a spark discharge or for other special sources in which constant density conditions may exist, the factor outside the exponential is different. However, as will be seen later, this term is not of primary importance and the main results will remain valid.

Thermal equilibrium, as stated previously, can normally only be obtained in high density discharges which have high temperatures associated with them. Under these conditions it is found experimentally (Brinkman 1937, Kruithof 1943) that the temperature falls a relatively small amount over the whole of the visible radius. This is indeed to be expected if $\boldsymbol{h}\nu/\boldsymbol{k}T_0 \sim 10$, since the exponential terms in (1 *a*), (1 *b*) and (2 *a*) control the functions. With this condition it is possible as a first approximation to take the functions F, f and g as solely proportional to the exponential terms. This gives

$$f_1 \text{ or } g_1 = (F)^{\alpha} \qquad \ldots\ldots(3)$$

where $\alpha = \nu_{\mathrm{tp}}/\nu_{\mathrm{sp}}$ or $\nu_{\mathrm{i}}/2\nu_{\mathrm{sp}}$ for f and g respectively. In such gases as hydrogen, helium, etc., the electron concentration variation will differ markedly from the intensity variation, since for these cases $\nu_{\mathrm{i}}/2\nu_{\mathrm{sp}} \sim \frac{1}{2}$, so that if the visible limit is taken as $F \sim 0{\cdot}01$ then $g \sim 0{\cdot}1$. This effect may appreciably affect measurements of average current densities if the temperature does not fall off rapidly beyond the visible radius.

Assuming always the validity of equations (1) and (2), the possibility of estimating the error in (3) and making more accurate calculations depends upon the value of $\boldsymbol{h}\nu_{sp}/\boldsymbol{k}T_0$, and for a given spectral line upon the accuracy of the knowledge of T_0. It is evident that if T_0 is known, equation (1) determines, at every value of F, the value of T_0/T_r and hence of f and g. We can improve upon the accuracy of the relationship (3) by making further approximations or by utilizing the exact relationships between the radial variations. These relationships are given by

$$f \text{ or } g = (F)^{\alpha}(T_r/T_0)^{\beta} \qquad \ldots\ldots(4)$$

where the values of α are as above and $\beta = \nu_{ts}/\nu_{sp}$ and $(\frac{1}{4} + \nu_i/2\nu_{sp})$ for f and g respectively.

Now the variations of F with T_r/T_0 for different values of $\boldsymbol{h}\nu_{sp}/\boldsymbol{k}T_0$ can be determined from equation (1a) and the results plotted in the form of curves as shown in the Figure. Thus if a function F has been obtained for a line of some value of $\boldsymbol{h}\nu_{sp}/\boldsymbol{k}T_0$, the curves can be used to obtain the corresponding values of T_r/T_0 and hence from equation (4) the functions f and g may be obtained.

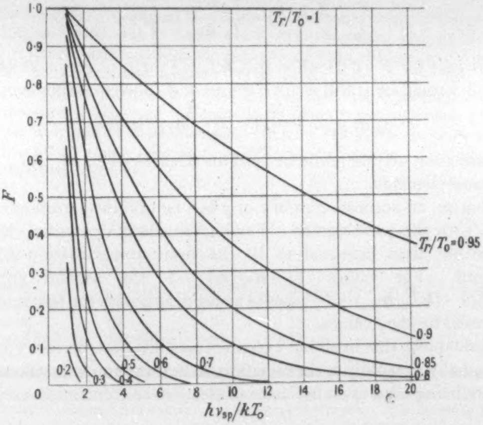

Now with $T_0 \sim 5{,}000$ °K., $\boldsymbol{k}T_0 \sim 0{\cdot}5$ ev., so that for the high ionization potential elements $\boldsymbol{h}\nu_{sp}/\boldsymbol{k}T_0 \sim 20$. An examination of the Figure shows that for this case the intensity has dropped to 1 % when T_r/T_0 has reached only 0·8. Since also $\beta = \nu_{ts}/\nu_{sp} \sim 0{\cdot}2$ it is clear that for these elements equation (3) for f is applicable. For the electron concentration case $\beta \sim 0{\cdot}9$ and an error is introduced if equation (3) is used. The error is not great since it is a percentage error of g and reduces as g increases. Thus with $g \sim 50\,\%$ the value given by equation (3) will be $\sim 52\,\%$. For the low ionization potential elements however $\boldsymbol{h}\nu_{sp}/\boldsymbol{k}T_0$ may approach the value 5. In this case the curves show $T_r/T_0 \sim 0{\cdot}6$ when $F = 5\,\%$. In this case $\beta = \nu_{ts}/\nu_{sp}$ may still be small, in which case the approximation for f, given by equation (3), may be used.

For the function g however the true relationship given by (4) must be used. In general it may be stated that with values of $\boldsymbol{h}\nu_{\mathrm{sp}}/\boldsymbol{k}T_0$ greater than or equal to 10 the simple relationship given in equation (3) may be used without undue error.

More accurate approximations to the true relationship can be obtained by determining T_r/T_0 in terms of F from equation (1 a) by the method of iteration and substituting the resulting approximations in equation (4).

Putting $T_0/T_r = \mathscr{T}$ and the first approximation $\mathscr{T}_1 = 1$ we obtain for subsequent approximations

$$\begin{array}{c} \mathscr{T}_2 = (1 - \xi \ln F) = x \\ \vdots \qquad\quad \vdots \\ \mathscr{T}_n = x + \xi \ln \mathscr{T}_{n-1} \end{array} \qquad \ldots\ldots(5)$$

where $\xi = \boldsymbol{k}T_0/\boldsymbol{h}\nu_{\mathrm{sp}}$. This gives the general nth approximation as

$$f_n \text{ or } g_n = (F)^\alpha/\{x + \xi \ln \mathscr{T}_{n-1}\}^\beta \quad \text{and} \quad f/f_2 \text{ or } g/g_2 = \{T_r/T_0(1 - \xi \ln F)\}^\beta.$$

From equation (1 a) we find also that

$$(1 - \xi \ln F) = (T_0/T_r)\{1 - (\boldsymbol{k}T_r/\boldsymbol{h}\nu_{\mathrm{sp}}) \ln (T_0/T_r)\},$$

so that

$$\frac{f}{f_2} \text{ or } \frac{g}{g_2} = \left\{1 - \frac{T_r}{T_0} \frac{\boldsymbol{k}T_0}{\boldsymbol{h}\nu_{\mathrm{sp}}} \ln \frac{T_0}{T_r}\right\}^\beta. \qquad \ldots\ldots(6)$$

Now for this case for $F = 0{\cdot}05$ when $\boldsymbol{h}\nu_{\mathrm{sp}}/\boldsymbol{k}T_0 = 5$; f/f_2 or $g/g_2 = \{0{\cdot}94\}^\beta$, and it is clear that only a small error will result if the second approximation is used, and this gives

$$f_2 \text{ or } g_2 = (F)^\alpha/\{1 - (\boldsymbol{k}T_0/\boldsymbol{h}\nu_{\mathrm{sp}}) \ln F\}^\beta. \qquad \ldots\ldots(7)$$

This approximation may therefore be used for all cases when $\boldsymbol{h}\nu_{\mathrm{sp}}/\boldsymbol{k}T_0 \geqslant 5$, and will thus cover most elements.

To summarize, an accurate plot of f or g can be obtained from equation (4) in conjunction with the curves given. For high ionization potential elements with $\boldsymbol{h}\nu_{\mathrm{sp}}/\boldsymbol{k}T_0$ greater than or equal to 10 the first approximation f or $g = (F)^\alpha$ may be used. For values $10 > \boldsymbol{h}\nu_{\mathrm{sp}}/\boldsymbol{k}T_0 > 5$ the second approximation f or $g = (F)^\alpha/\{1 - (\boldsymbol{k}T_0/\boldsymbol{h}\nu_{\mathrm{sp}}) \ln F\}^\beta$ should be used, although the first approximation may still be used for the f values.

The analysis shows that in all but extreme cases the electron concentration does not fall off radially as rapidly as the radiation, so that care must be taken if intensity variations are being used as an indicator of electron concentration variations.

ACKNOWLEDGMENTS

The author wishes to record his appreciation of the interest shown by Professors F. J. Teago and J. M. Meek and of the helpful discussions he has had with Dr. J. D. Craggs.

REFERENCES

Brinkman, H., 1937, *Optical Studies of Electric Arcs*, Dissertation (Utrecht).

Edels, H., 1950, *E.R.A. Report* L/T 230.

Fowler, R. H., 1929, *Statistical Mechanics* (Cambridge : University Press), p. 370.

Kruithof, A. M., 1943, *Investigation into the Applicability of the Saha Formula to the Electric Arc*, Thesis (Utrecht).

Ornstein, L. S., and Brinkman, H., 1934, *Physica*, **1**, 797.

Saha, M. N., 1920, *Phil. Mag.*, **40**, 472; 1921, *Ibid.*, **41**, 267; 1923, *Ibid.*, **46**, 534.

Schulz, P., 1947, *Ann. Phys., Lpz.*, **6**, 318, *Z. Naturforsch.*, **2a**, 662.

LETTERS TO THE EDITOR

The Interpretation of Radiosonde Data in Relation to Cosmic-Ray Intensity Variation

Nicolson and Sarabhai (1948) have recently discussed difficulties in interpreting quantitatively the semi-diurnal variation of cosmic-ray intensity in terms of the theories of atmospheric oscillations. Duperier (1948) has also discussed the possibility of relating vertical movements of the higher levels of the atmosphere to the 'temperature effect' in cosmic-ray intensity in particular.

One major difficulty in this latter study lies in correct interpretation of the radiosonde results. It is difficult to disentangle true heating and resulting expansion of the free air from any positive temperature error due to insolation of the thermometer element itself when the ascents take place in daylight.

The ascents from two radiosonde stations, Downham Market ($52\frac{1}{3}$° N., $\frac{1}{2}$° E.) and Larkhill ($51\frac{1}{2}$° N., 2° W.) are here analysed for the year 1948. The ascents take place at 03, 09, 15 and 21 hours G.M.T. daily. The ascents at 03 and 21 hours occur in darkness and the 09 and 15 hours in sunlight throughout the year. The two latter are liable to thermometer error.

The data are taken from the Daily Weather Reports (Upper Air Section) issued by the Meteorological Office. The heights at fixed pressure levels are computed from temperatures and pressures measured by the Kew radiosonde (Dymond 1947).

In the Table are given : Column (1). H, the seasonal mean height of the pressure levels 300 mb. and 100 mb. at 03 and 21 hours G.M.T. (The nocturnal change in height from 21 to 03 hours is small compared with the apparent daylight changes, and it is convenient to consider the former ascents together. The height given in the first column will approximate to conditions at midnight.) Column (2). ΔH_1, the apparent increase in height of these two pressure levels since midnight at 09 hours G.M.T. Column (3). ΔH_2, the apparent increase in height at 15 hours G.M.T. Column (4). f_1, the percentage of the total apparent height change which occurs *above* 300 mb. at 09 hours. Column (5). f_2, the corresponding value at 15 hours.

	(1)	(2)	(3)	(4)	(5)	(6)
Season	H (km.)	ΔH_1 (m.)	ΔH_2 (m.)	f_1 (%)	f_2 (%)	Pressure level (mb.)
Spring	$9{\cdot}11_5$	+3	+13	90	78	300
(Feb., Mar., Apr.)	$16{\cdot}16_2$	+29	+58			100
Summer	$9{\cdot}23_3$	+17	+20	75	77	300
(May, June, July)	$16{\cdot}17_2$	+68	+85			100
Autumn	$9{\cdot}31_8$	+14	+23	78	69	300
(Aug., Sep., Oct.)	$16{\cdot}38_7$	+64	+73			100
Winter	$9{\cdot}07_0$	+9	+ 9	72	56	300
(Nov., Dec., Jan.)	$16{\cdot}03_7$	+32	+27			100

Standard deviation of ΔH values: *c.* ±60 metres at 300 mb. ; ±120 metres at 100 mb.
Probable error of seasonal ΔH values: *c.* ±4 metres at 300 mb. ; ±8 metres at 100 mb.

It will be noticed that the major part, 75% on the average, of the apparent daylight increase in height of the 100 mb. pressure level takes place *above* the 300 mb. pressure level. It is just in these higher levels that there is least certainty about the magnitude of whatever temperature error there may be due to insolation on the thermometer assembly of the radiosonde. If in daylight the thermometer were to read too high between 300 mb. and 100 mb., by about $\frac{3}{4}$° K. in winter, rising to about $1\frac{3}{4}$° K. in summer, then the values ΔH_1 and ΔH_2 for 100 mb. would be reduced to the values given for 300 mb. Insolation errors approaching this order of magnitude are not impossible. Furthermore, it would be extremely difficult to account for the measured daylight temperature increases. The flux of solar energy in the lower stratosphere is insufficient to provide the apparent diurnal heating by absorption of radiation, unless our knowledge of the composition of the atmosphere at these levels is very false, and the dynamic processes required to produce the observed diurnal changes would be extremely complex, when it is remembered that diurnal surface pressure changes must remain within the small limits observed in our latitudes. There is at the moment little direct evidence for the existence of such diurnal dynamic effects as are required, and also little experimental assessment of the magnitude of radiation errors in actual flights. (The meteorological problem is discussed in more detail in a paper to be published shortly in the *Quarterly Journal of the Royal Meteorological Society*.)

For ascents which take place symmetrically about local noon, and which have probably similar radiation errors, it appears that the differential heating, which ought to be real, is a slowly increasing function of height. $((\Delta H_2 - \Delta H_1)$ has an average for the whole year in this analysis of 4 metres at 300 mb. and 10 metres at 100 mb.) If these figures should correspond more closely to the real variation in ΔH with height than do the measured ΔH values, then correlations of ΔH with simultaneous ground temperature changes will necessitate the choice of higher levels of the atmosphere to attain the coefficient of 18 metres per centigrade degree arrived at by Duperier (1948) from discussion of diurnal changes.

It should be noticed also that, whereas the apparent diurnal temperature changes in the lower stratosphere are rather closely symmetrical about local noon, the maximum of the ground level diurnal temperature change is shifted to about 15 hours at all seasons.

Conclusions.

(1) In the absence of evidence concerning the reality of the apparent *diurnal* changes in height of the isobaric levels in the lower stratosphere, it is best to disregard these changes in correlating H with ground temperature to arrive at a value for the 'temperature effect' in cosmic-ray intensity.

(2) Correlation of annual variation in the monthly mean value of the height of the 100 mb. pressure level with ground temperature would seem to be fully justified. The radiosonde ascents which have taken place since 1938 bear out as substantially correct Blackett's assumption (1938) of a *seasonal* change in the monthly mean value of the height of this pressure level of the order of 500 metres, accompanying the mean summer–winter variation in ground level temperature of about 10° C.

(3) Since day-to-day changes of the height of the 100 mb. pressure level can be of the order of 300 metres (i.e. approaching the magnitude of the seasonal change in monthly mean height), it would seem worth while to correlate these directly with changes in cosmic-ray intensity.

(4) The meteorological data are now so abundant—four ascents daily from six stations in the British Isles—that there is no difficulty in synchronizing cosmic-ray observations with meteorological ascents. Since ground level temperature changes are so closely dependent upon local conditions, it is perhaps better to refer the 'temperature effect' to larger fractions of the atmosphere (see Millican and Loughridge 1948). Data are given by the Meteorological Office at intervals of 50 mb. from ground level to 200 mb. (approximately 14 km.) at 20 mb. intervals to 100 mb. (16 km.), and thereafter at 10 mb. intervals to the top of the ascent.

(5) The measured apparent *diurnal* changes in the height of the 100 mb. pressure level do not explain either the magnitude or phase of the *diurnal* variation in cosmic-ray intensity.

The Clarendon Laboratory,
Oxford.
R. H. Kay.

3rd February 1951.

Blackett, P. M. S., 1938, *Phys. Rev.*, **54**, 973.
Duperier, A., 1948, *Proc. Phys. Soc.*, **61**, 34.
Dymond, E. G., 1947, *Proc. Phys. Soc.*, **59**, 645.
Millican, F. M., and Loughridge, D. H., 1948, *Phys. Rev.*, **74**, 66.
Nicolson, P., and Sarabhai, V., 1948, *Proc. Phys. Soc.*, **60**, 509.

Properties of Amorphous Selenium in the Infra-Red

The optical constants of amorphous selenium in the visible region are well known (Barnard 1930, Becker and Schaper 1944), but only qualitative results in the infra-red seem to have been recorded (Becker and Schaper 1944, Elliott, Ambrose and Temple 1948). The purpose of this note is to give some results of recent measurements. Specimens of amorphous selenium in the form of prisms and parallel-sided slabs were made by allowing pure melted selenium to solidify rapidly between two optically worked glass plates. The Figure shows the transmission T of a typical parallel-sided specimen as a function of wavelength. On the long-wave side of $0{\cdot}7\mu$ transmission is high and is determined in this thickness (0·162 cm.) almost entirely by the reflection at the two surfaces.

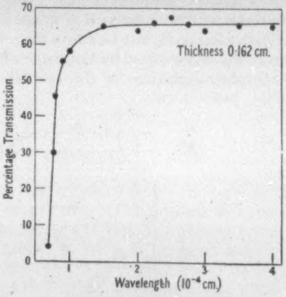

Amorphous selenium.

The absorption coefficient α at any one wavelength may be determined from the slope of the ($\log T$, thickness) curve, the error due to multiple reflections being small. The lowest values of α found in measurements of a number of prisms are :

λ (μ)	0·8	1·0	2·0	4·0
α (cm^{-1})	3·3	1·9	0·55	0·52

Some specimens gave higher values, probably owing to partial crystallization.

Refractive indices for prisms were obtained by measuring the angle of minimum deviation at $0{\cdot}819\mu$ and $1{\cdot}014\mu$ using an infra-red image convertor tube. The mean values obtained from prisms of angles between 5° and 15° are for $\lambda = 0{\cdot}819\mu$, $n = 2{\cdot}589 \pm 0{\cdot}005$, and for $\lambda = 1{\cdot}014\mu$, $n = 2{\cdot}520 \pm 0{\cdot}005$. The index values were extended to longer wavelengths by an interference method using thin films. At wavelengths beyond 2μ the index attains a nearly constant value of about 2·45. The low value of absorption suggests the use of amorphous selenium as an optical material for infra-red wavelengths. It has the advantage of ease of preparation and is stable in the atmosphere.

Thanks are due to Prof. R. W. Ditchburn for helpful advice and to Messrs. Standard Telecommunication Laboratories, Ltd., for a grant (E. W. S.). One of us is a member of the Royal Naval Scientific Service (H. A. G.). We also wish to thank Prof. Lark Horovitz and Dr. K. Frank, with whom we had discussions during the 1950 Reading Conference on the Properties of Semiconducting Materials.

Physics Department,
The University, Reading.
23rd January 1951.

H. A. Gebbie.
E. W. Saker.

Barnard, G. P., 1930, *The Selenium Cell* (London : Constable).
Becker, A., and Schaper, J., 1944, *Z. Phys.*, **122**, 49.
Elliott, A., Ambrose, E. J., and Temple, R. B., 1948, *J. Opt. Soc. Amer.*, **38**, 212.

A Note on the Dielectric Dispersion in Polycrystalline Materials

Dielectric dispersion has recently been observed in certain polycrystalline solids, particularly semiconductors, due to their inhomogeneous structure. Thus, Chasmar (1948) has observed a large decrease in the resistance of PbS and PbSe films with increasing frequency, and interpreted this as a bridging of the high resistance between the intergranular boundaries by their capacitive reactance. Similarly, Volger (1951) has explained the decrease of both capacitance and resistance of certain ceramic materials by their grain structure. German work along similar lines on selenium has been reported (*F.I.A.T. Report* 1946).

To explain such results, a model is assumed (Figure 1 (*a*)) consisting of low-resistance grains G (resistance R_g) in series with boundaries B of much higher resistance R_b shunted by a capacitance C_b. The high value of R_b may be due to the presence of an air gap reducing the area of contact between grains as postulated by Volger, or of a layer of material of higher resistivity, for instance amorphous selenium in the case of microcrystalline selenium.

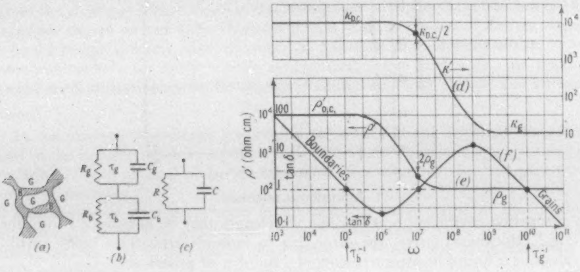

Figure 1.

At high frequencies the boundary resistance is shunted by its capacitance so that only the grain resistance is measured, whilst at low frequencies resistance and capacitance of the boundaries are measured. It is clear that an abnormally high permittivity is obtained if the large capacitance value measured at low frequencies is referred to the total thickness of the sample.

The model can be elaborated (Figure 1 (*b*)) by including the capacitance C_g of the grains, which becomes important at higher frequencies ($C_g \ll C_b$, owing to the much smaller thickness of the boundaries). It can then be shown that the apparent permittivity and loss angle vary with the frequency in a similar way as in the case of Debye dispersion.

The expressions resulting for the equivalent capacitance C and shunt resistance R of the model circuit shown in Figure 1 (*b*) are

$$R = R_b \frac{1+\omega^2 R_g^2 C_b^2}{1+\omega^2 R_g R_b C_b^2}\,; \qquad C = C_b \frac{1+\omega^2 R_g^2 C_g C_b}{1+\omega^2 R_g^2 C_b^2}\,;$$

$$\tan\delta = \frac{1}{RC\omega} = \frac{1}{R_b C_b \omega}\,\frac{1+\omega^2 R_g R_b C_b^2}{1+\omega^2 R_g^2 C_g C_b}$$

under the simplifying assumptions $R_b \gg R_g$ and $C_b \gg C_g$.

Owing to the power loss component $(\omega C R_b)^{-1}$ due to the D.C. conductivity, the value of $\tan\delta$ first drops as the frequency is increased, goes through a minimum

$$\tan\delta_{\min} = 2(R_g/R_b)^{1/2} \quad \text{at} \quad \omega_{\min} = 1/C_b(R_b R_g)^{1/2},$$

and then passes through a maximum value

$$\tan\delta_{\max} = \tfrac{1}{2}(C_b/C_g)^{1/2} \quad \text{at} \quad \omega_{\max} = 1/R_g(C_g C_b)^{1/2}.$$

The 'A.C. component' of $\tan\delta$, i.e.

$$\frac{1}{RC\omega} - \frac{1}{R_b C\omega} = \frac{\omega R_g C_b}{1+\omega^2 R_g^2 C_g C_b},$$

is of the standard Debye form.

Figure 1 (*e*), (*d*), (*f*) illustrate the variation with frequency of apparent resistivity ρ', permittivity κ' and power factor $\tan\delta$ for a typical polycrystalline semiconductor with parameters assumed as given in the Table.*

---

* These values correspond in order of magnitude to standard selenium rectifiers.

Polycrystalline Se per cm^2 area

		Crystalline grains	Amorphous boundaries
Permittivity	κ	10	10
Resistivity	ρ (ohm cm.)	10^2	10^7
Total thickness	t (cm.)	10^{-2}	10^{-5}
Resistance	R (ohms)	1	$\leqslant 10^2$
Capacitance	C (pF.)	10^2	$\leqslant 10^5$
Time constant	τ (sec.)	10^{-10}	$\leqslant 10^{-5}$
		High frequencies	Low frequencies
Apparent permittivity	κ'	10	10^4
Apparent resistivity	ρ' (ohm cm.)	10^2	10^4

Another case of abnormally high dielectric constant has recently been reported (Laurila 1950) for thin 'sputtered' layers of CaF_2. The apparent dielectric constant when measured shortly after deposition of the layers was very high (550 to 4,400) but, within a day or so, dropped to more normal values (5 to 10). At the same time, however, the A.C. and D.C. resistance of the samples *increased* by a factor varying from 15 to over 700 for different samples. Such behaviour might be explained by assuming single crystallites of high resistivity embedded in a matrix of comparatively low resistivity which practically short-circuits the gaps between individual crystallites. Such a low-resistivity matrix may simply consist of condensed moisture or of some other conducting impurity deposited between the grains. As this is driven off or is replaced by continued growth of the crystallites the overall resistance would be expected to rise and the capacitance to drop to more normal values.

It should be mentioned that the model of an inhomogeneous semiconductor differs only in some detail from the model of an inhomogeneous dielectric (the Maxwell–Wagner mechanism of dielectric loss), which also gives rise to a set of Debye equations.

Thus from dielectric measurements alone it cannot be decided what mechanism is causing dielectric dispersion, but often the magnitudes involved will point to the above model as the most likely explanation of a particularly high dielectric constant. The true electrical parameters of the grain material are then measured only at high frequencies; but useful information on the relative thickness and resistance of the boundaries may also be deduced from the extreme values of the tan δ curve over the significant range of frequencies.

Research Laboratory,
Associated Electrical Industries Ltd.,
Aldermaston Court,
Aldermaston, Berks.
19th January 1951.

E. Billig.
K. W. Plessner.

Chasmar, R. P., 1948, *Nature, Lond.*, **161**, 281.
F.I.A.T., 1946, *Final Report* No. 706, 38.
Laurila, E. A., 1950, *Phys. Rev.*, **77**, 405.
Volger, J., 1951, *Proceedings of the Conference on the Properties of Semiconducting Materials* (London: Butterworth's Scientific Publications).

A Surface Effect in the Creep Behaviour of Polycrystalline Lead

There is much experimental evidence to show that the mechanical properties of metal single crystals are influenced by the condition of the surface, in particular by its freedom or otherwise from oxide layers (Andrade 1949, Andrade and Randall 1948). In polycrystalline wires a surface effect of a somewhat different kind is to be anticipated. It is tolerably clear now that the β, or transient, flow and the κ, or permanent, flow are, in the main, due to two different physical processes, although they are not independent phenomena (Andrade 1948), the β being particularly associated with glide within the crystal grains and the κ flow with intergranular movement. Now glide within the grains is, of course, influenced by surface conditions, and in a polycrystalline material the grains at the free metal surface are in a privileged position, in that one boundary is free, while those in the neighbourhood of the surface are somewhat less constrained than those well in the interior of the metal. Hence a surface effect on creep is to be anticipated in the sense that the surface layers should offer relatively small resistance to creep. Such an effect has been established.

The effect will clearly be easier to detect if only transient flow is present. The creep of commercial lead at room temperature is closely represented by the equation

$$l=l_0(1+\beta t^{1/3})\exp(\kappa t) \qquad \ldots\ldots (1)$$

with finite values of κ, and so is the creep of the purest lead, but here recrystallization under stress takes place (Andrade 1948 b). It has been found that the addition of 0·05% tellurium to pure lead gives a metal which, at room temperature, shows no permanent flow except at the highest stresses, the creep being, in general, accurately represented by (1) with $\kappa=0$. The present experiments have been carried out with such lead. Certain pecularities have been observed at very low stresses, and at the highest stresses κ has a finite value. The following results refer to a range of stresses (about 50 to 95 kg/cm²) within which β varies with stress in the sigmoid way described in the early papers (Andrade 1910, 1914) and since confirmed by Sinclair and by Jolliffe working in the Carey Foster Laboratory (to be published shortly).

Experiments were carried out with wires of four different diameters, viz. 1, 2, 3 and 5 mm. approximately, the grain diameter being very nearly the same, 0·2 mm., in each case. Figure 1 (*a*) shows the values of β at different stresses for the four wires at a temperature of 31·5° C. : the discussion of the peculiar behaviour at low stresses we reserve for later full publication. The stresses are, of course, the average longitudinal stresses for the whole cross section. It will be seen that to produce the same transient creep in different wires requires an average stress which is higher the thicker the wire, which is what we should expect if there were a relatively weak boundary layer.

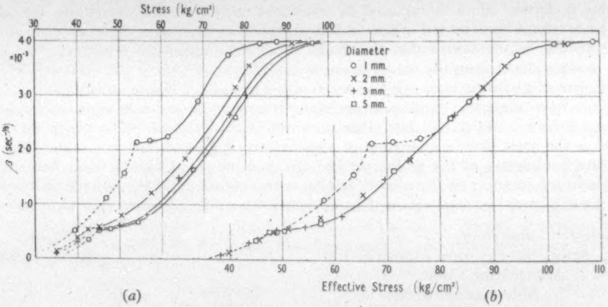

(*a*) (*b*)

Figure 1. (*a*) β against stress for different diameters; (*b*) β against effective stress, according to formula (2), for different diameters.

The results can be represented by assuming that the average stress S required to give a chosen value of β, i.e. a chosen transient creep, is given by

$$S=S_0\, r^2/(r-na)^2, \qquad \ldots\ldots (2)$$

where a is the average grain diameter, r the radius of the wire, S_0 the value of S for very large values of r, when the surface effect is negligible, and n is a constant to be found, na representing in an arbitrary way the equivalent thickness of the weak boundary layer. Taking $\beta=2{\cdot}50\times10^{-3}\,\mathrm{sec}^{-1/3}$, for example, for which, from low to high diameter, the corresponding measured stresses are 66·0, 72·25, 75·20 and 77·3 kg/cm², the value $n=0{\cdot}301$ gives for S_0 in the four cases 82·13, 82·19, 81·81 and 81·74 kg/cm², which vary from the average by less than 0·3%, a constancy as satisfactory as can be expected.

Figure 1(*b*) shows the values of β for all the observations, for the four different diameters, plotted against the effective stress as deduced from (2) with $n=0{\cdot}301$. It will be seen that, neglecting the abnormality represented by the broken lines (which in the range of effective stress 47 to 110 kg/cm^2 applies to the 1 mm. diameter wire only and will, as has been said, be discussed in full publication) all the observations for effective stresses above 50 kg/cm^2 are very satisfactorily represented. The value of n is also a reasonable one : the surface effect can be represented by supposing that a layer of thickness about one-third of a grain diameter offers no resistance to creep. This is clearly an arbitrary way of representing the surface effect : n may be called 'the effective depth coefficient' of the surface layer. It remains to be tested whether n is constant with different grain size.

The non-uniformity of behaviour over the cross section has been established by x-ray examination, the method being to reduce the diameter of the strained wire by successive cold etching with 1 part hydrogen peroxide to 3 parts acetic acid (Worner and Worner's solution) and take back-reflection photographs at each stage with characteristic copper radiation. For a specimen of initial diameter 1·95 mm., subjected to slow creep at 65° c., in which a total strain of 6·5% was produced in 250 hours, two close well-resolved rings due to the copper Kα doublet are obtained at all depths, there being, however, a slight broadening of the lines in the case of the original surface. For a 3 mm. diam. specimen more rapidly extended at room temperature (final strain 10% attained in 10 minutes) the surface effect is the same, but the broadening of the lines increases progressively with increasing depth, the Kα doublet being resolvable at a depth of 0·16 mm. but not at a depth of 0·25 mm., the broadening being due, no doubt, to heavy internal stresses. At a depth of 0·78 mm. (final diameter 1 mm.) the smeared ring is very broad. With more rapid extension to 10% final strain the surface gives the same clearly resolvable rings as in the case of slow extension, but the interior exhibits recrystallization, evidenced by well-marked discrete spots in the rings. This recrystallization is accompanied by internal stresses, evidenced by the general broadening of the rings. At higher rates of extension, however (10% final strain attained in 15 seconds), the interior shows large-scale recrystallization and little evidence of internal stresses, as would be expected, the stresses being relieved by the adjustments involved in recrystallization. This is illustrated in the series of photographs shown in Figure 2.

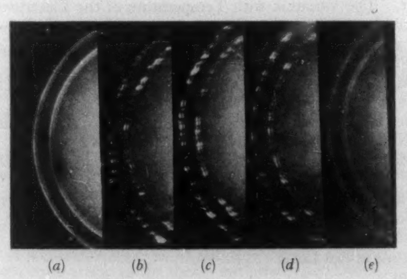

Figure 2. Back-reflection photographs of tellurium lead.
(*a*) Surface of wire, unetched, after 10% extension in 15 sec.: diameter 2·73 mm. (*b*) Specimen etched down to 1·75 mm. diameter. (*c*) Etched down to 1·40 mm. diameter. (*d*) Etched down to 1·0 mm. diameter. (*e*) Untreated surface of another part of the original specimen after the previous photographs had been taken, as control. Reflection from (220) and (311) planes.

That the difference between the internal photographs and the surface photographs is not due to general recrystallization taking place subsequent to the straining, and progressing during the time occupied in the preparation of the specimens by etching, is shown by the fact that surface photographs taken subsequent to the internal photographs with another—untreated—part of the specimen showed the same sharp rings as initially.

The slow extension at 65° means a small extension due to β flow, the rapid extension at room temperature a practically complete β flow (Kennedy 1949).

The x-ray work, which has established that a fairly sharp change in the type of structure takes place at a depth somewhere about 0·1 mm. below the surface, is continuing, with the object of establishing in more detail the nature of the transition. It is cited here to emphasize the real existence of a surface effect in the flow of polycrystalline metal.

We should like to acknowledge the valuable assistance of the British Non-Ferrous Metals Research Association and in particular of the Director, Mr. G. L. Bailey, in the preparation of the lead wires. Mr. H. Smith, of this laboratory, has given great help in the running of the x-ray equipment, for which our thanks are due.

Davy Faraday Research Laboratory,
The Royal Institution, London W.1.
14th February 1951.

E. N. da C. Andrade.
A. J. Kennedy.

Andrade, E. N. da C., 1910, *Proc. Roy. Soc.* A, **84**, 1; 1914, *Ibid.*, **90**, 329; 1948 a, *Report of 1947 Conference on the Strength of Solids* (London : Physical Society); 1948 b, *Nature, Lond.*, **162**, 410; 1949, *Ibid.*, **164**, 536.
Andrade, E. N. da C., and Randall, R. F. Y., 1948, *Nature, Lond.*, **162**, 890.
Kennedy, A. J., 1949, *Proc. Phys. Soc.* B, **62**, 501.

Note added in proof. In a paper which has just reached us, T. Nishishara and S. Taira (*Mem. Fac. Engng. Kyoto Univ.*, 1950, **12**, 90–118) report observations on the non-uniformity of stress across the cross section of steel and aluminium specimens deformed plastically in tension. As far as they go, their qualitative deductions are in agreement with what we here record.

CONTENTS FOR SECTION A

PAGE
Dr. H. Wilman. The Slip, Twinning, Cohesion, Growth and Boundaries of Crystals . . . 329
Dr. R. W. Wright. The Variation with Temperature of the Electrical Properties of a Degenerate Electronic Semiconductor as exemplified by Cadmium Oxide . 350
Dr. F. Ansbacher and Dr. W. Ehrenberg. Electron-Bombardment Conductivity of Dielectric Films . . . 362
Dr. R. A. Hull, Mr. K. R. Wilkinson and Dr. J. Wilks. The Specific Heat of Liquid Helium at Temperatures between 0·6° and 1·6° K. . . . 379
Dr. G. H. Stafford. The Total Cross Section of Beryllium, Aluminium, Sulphur and Lead for Neutrons of Energies from 2 Mev. to 6 Mev. . . . 388
Dr. F. D. S. Butement. New Radioactive Isotopes produced by Nuclear Photo-Disintegration . . . 395
Dr. M. G. Mylroi and Dr. J. G. Wilson. On the Proton Component of the Vertical Cosmic-Ray Beam at Sea Level . . . 404
Dr. B. G. Owen and Dr. J. G. Wilson. Further Measurements of the Charge Ratio of μ-Mesons at Sea Level . . . 417
Letters to the Editor :
    Dr. W. Ehrenberg, Mr. Chi-Shi Lang and Mr. R. West. The Electron Voltaic Effect . . . 424
    Dr. G. Stephenson. Calculation of Oscillator Strengths for certain Electronic Transitions in B_2 and Na_2 . . . 425
    Dr. Suraj N. Gupta. On the Elimination of Divergencies from Quantum Electrodynamics . . . 426
    Dr. J. W. Gardner. On the Elimination of Divergencies from Classical Electrodynamics . . . 427
    Dr. F. D. S. Butement. Radioactive ^{159}Dy . . . 428
    Dr. W. M. Vaidya. Isotope Effect in Hydrocarbon Flame Bands . . 428
    Mr. W. R. S. Garton. Emission Band of the Cd_2 Molecule at λ 2212 . . 430
    Dr. S. Levine and Mr. A. Suddaby. Free Energy of the Double Layers of Two Plates at Large Separations . . . 431
Reviews of Books . . . 433
Contents for Section B . . . 438
Abstracts for Section B . . . 438

ABSTRACTS FOR SECTION A

The Slip, Twinning, Cohesion, Growth and Boundaries of Crystals, by H. Wilman.

ABSTRACT. The nature and stability of intercrystalline boundaries are discussed and conclusions as to preferred relative orientations are illustrated by ball-bearing and bubble-raft models.

Electron-diffraction evidence from crystals of layer-lattice, ionic, metallic and van der Waals (organic molecular) types is presented, showing that crystal pairs and symmetrical or unsymmetrical triplet or multiplet crystal groupings occur, having a common lattice row, but in relative azimuthal orientations at intervals agreeing with the predictions. The component crystals were thus in coherent metastable contact of the type discussed, and in some cases strong secondary elastic scattering showed that the crystals were extensively superposed on the plane which was normal to the common row.

The seven types of electron-diffraction pattern observed from such groupings, and the nature of the specimen preparation, suggest that the origin of these groupings is a mechanical deformation of the crystals during or after growth, by a process of 'rotational slip' which has not hitherto been explored or defined in nature. Such slip is directly demonstrated macroscopically as a deformation process in potassium ferrocyanide trihydrate and gypsum, the slip being produced on the planes parallel to the highly perfect cleavage.

The relation between rotational slip and the known types of translational slip and dislocation theory is indicated, and in particular the 'deformation bands' investigated especially by Barrett and his collaborators are concluded to be essentially rotational slip bands initially at low deformation, though modified by translational types of slip at higher deformation.

A valuable new insight is also provided into many observations on crystal growth and properties, especially the nature, determining conditions, stability and disorientation of crystals growing epitaxially on single crystal substrates, and into the nature of the deformation caused by unidirectional abrasion of crystals.

The Variation with Temperature of the Electrical Properties of a Degenerate Electronic Semiconductor as exemplified by Cadmium Oxide, by R. W. Wright.

ABSTRACT. Strong strip specimens are prepared from CdO powder such that they possess an electrical conductivity of the order of 300 ohm^{-1} cm^{-1} at room temperature. Simultaneous measurements of the Hall constant R and the electrical conductivity σ are made throughout the temperature range 0–500° c., and the thermoelectric power dE/dT is measured immediately afterwards on the same specimen. The properties are found to resemble those of a metal: R is found to have a constant value independent of the temperature. dE/dT is approximately 60 μv/deg. c. at room temperatures, whilst σ decreases with temperature, its value at 500° c. being roughly half that at 0° c.

The theory of degenerate semiconductors is developed, and since the values of R indicate that there is a constant number of free electrons in each specimen, this result is incorporated into the comparison of the theory with the experimental results. Satisfactory agreement is obtained between theory and experiment. Agreement is also obtained when the theory is compared with results obtained by another investigator for the thermoelectric power of CdO. The approximate form of the theory predicts that the thermoelectric power and the resistivity should be directly proportional to the absolute temperature. The experimental results are found to confirm this. CdO behaves as an excess degenerate semiconductor, with properties strongly resembling those of a metal.

Electron-Bombardment Conductivity of Dielectric Films, by F. Ansbacher and W. Ehrenberg.

ABSTRACT. Films of some dielectrics become conductive under the influence of electron bombardment. This conductivity is investigated both for steady and for alternating bombardment in its dependence particularly on temperature, current density and the potential difference across the dielectric. The gain, i.e. the ratio of current through the film to the bombarding current increases strongly with temperature. On arsenic sulphide films, the gain reaches 40,000. The effect is discussed in the light of theories of conduction in dielectrics and of recent work on allied subjects.

The Specific Heat of Liquid Helium at Temperatures between 0·6° *and* 1·6°K., by R. A. HULL, K. R. WILKINSON AND J. WILKS.

ABSTRACT. A detailed account is given of experiments made to measure the specific heat of liquid helium between 0·6 and 1·6° K. Below 1·4° the specific heat may be expressed as $C=0{\cdot}024T^{6\cdot2}$ cal/gm/deg. Some implications of this result are briefly discussed.

The Total Cross Section of Beryllium, Aluminium, Sulphur and Lead for Neutrons of Energies from 2 *MeV. to* 6 *MeV.*, by G. H. STAFFORD.

ABSTRACT. The total neutron cross sections of beryllium, aluminium, sulphur and lead have been measured in the range of energies from 2 MeV. to 4 MeV. and from 5 MeV. to 6 MeV. by a transmission experiment. Resonances were observed in all four elements. The results obtained for lead and for beryllium are compared with those expected according to the one-body theory for light nuclei.

New Radioactive Isotopes produced by Nuclear Photo-Disintegration, by F. D. S. BUTEMENT.

ABSTRACT. Photonuclear (γ, n) and (γ, p) reactions produced by 23 MeV. X-rays from a synchrotron have been used to prepare new radioactive isotopes, the method being particularly advantageous for neutron-excess isotopes in the region $Z=63$ to 79. Whenever possible the isotopes were chemically identified. The following table summarizes the results.

Element Irradiated	Element Chemically Identified	Half-Life	Assignment
Se	As	9 minutes	^{79}As
Sm	Sm	8 minutes	^{143}Sm or ^{146}Sm
Eu	Eu	15 hours	^{150}Eu
Gd	—	20 minutes	^{159}Eu or Gd^{m}
Dy	—	14 minutes	^{162}Tb or ^{163}Tb
Er	—	96 minutes	^{163}Er, ^{167}Ho or ^{169}Ho
Yb	—	19 minutes	^{172}Tm, ^{173}Tm or ^{175}Tm
Hf	Lu	22 minutes	^{178}Lu or ^{179}Lu
W	Ta	48 minutes	^{185}Ta
W	Ta	116 hours	^{183}Ta
Os	Re	17 minutes	^{189}Re or ^{191}Re
Pt	Ir	66 minutes	^{195}Ir or ^{197}Ir
Hg	Au	27 minutes	^{201}Au or ^{203}Au

Definite mass assignments, hitherto uncertain, have been made for 18-hour ^{159}Gd and 48-minute ^{200}Au.

On the Proton Component of the Vertical Cosmic-Ray Beam at Sea Level, by M. G. MYLROI and J. G. WILSON.

ABSTRACT. Approximately 1% of the vertical cosmic-ray intensity at sea level is shown to consist of protons. These form a momentum spectrum of index −2·8 in the range 10^3 MeV/c $< p < 5\times10^3$ MeV/c. and have an absorption range in lead, 160 ± 40 gm.cm^{-2}. Using existing measurements at high altitude, the attenuation in the atmosphere of protons in the spectral region investigated is found to take place with a range 140 ± 10 gm.cm^{-2}.

There is no negatively charged component of strong nuclear interaction in the vertical beam of intensity as great as 0·1% of the whole beam.

Further Measurements of the Charge Ratio of μ-Mesons at Sea Level, by B. G. OWEN and J. G. WILSON

ABSTRACT. Extended measurements of the charge ratio (positive/negative) of near-vertical μ-mesons at sea level show that it increases with meson momentum from about 1·17 at 10^3 MeV/c. up to about 1·26 at 4×10^3 MeV/c. At higher momenta the statistical accuracy of the measured charge ratio is limited by the instrumental rate of collection, and it cannot yet be definitely decided whether the charge ratio decreases with increasing momentum, although the evidence now available favours a slow decrease.

The general implications of the form of variation of charge ratio with momentum are indicated.

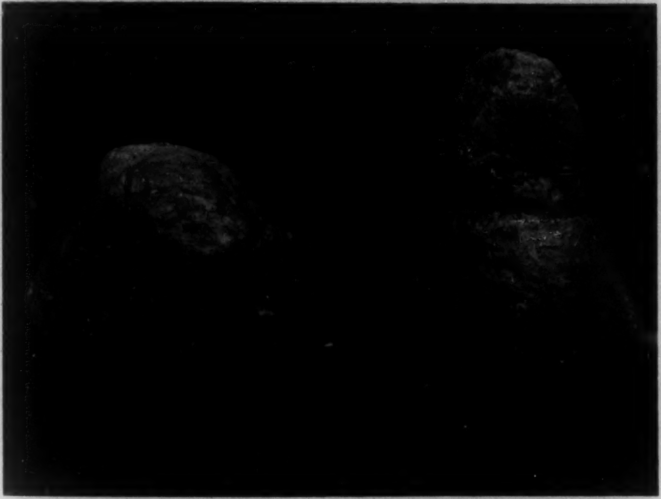

Figure 1.

(*a*) Wax impression of crater in lead block due to jet from tin cap.
(*b*) Wax impression of crater in lead block due to jet from steel cone.

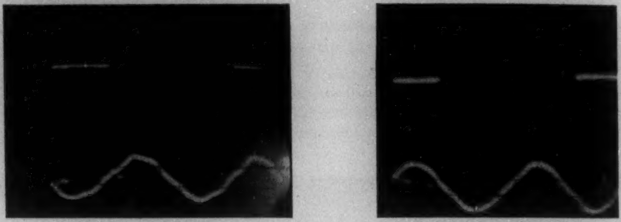

(*a*) 300 c/s. pulse.

(*b*) 1,000 c/s. pulse.

Figure 5. 20 msec. vibrator voltage pulse.

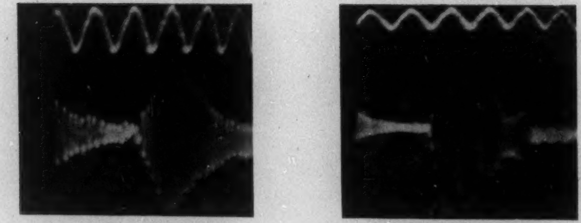

(*a*) 300 c/s., rod mountings.

(*b*) 600 c/s., rod mountings.

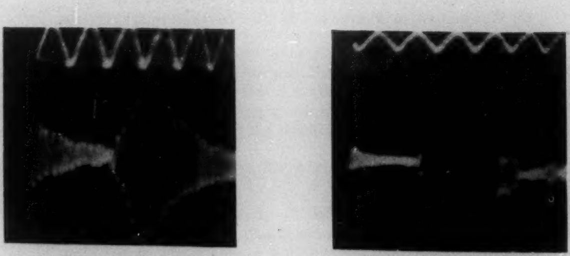

(*c*) 300 c/s., spring mountings

(*d*) 600 c/s., spring mountings

Figure 7. Vibrations recorded at 130 ft., with the vibrator in various conditions.

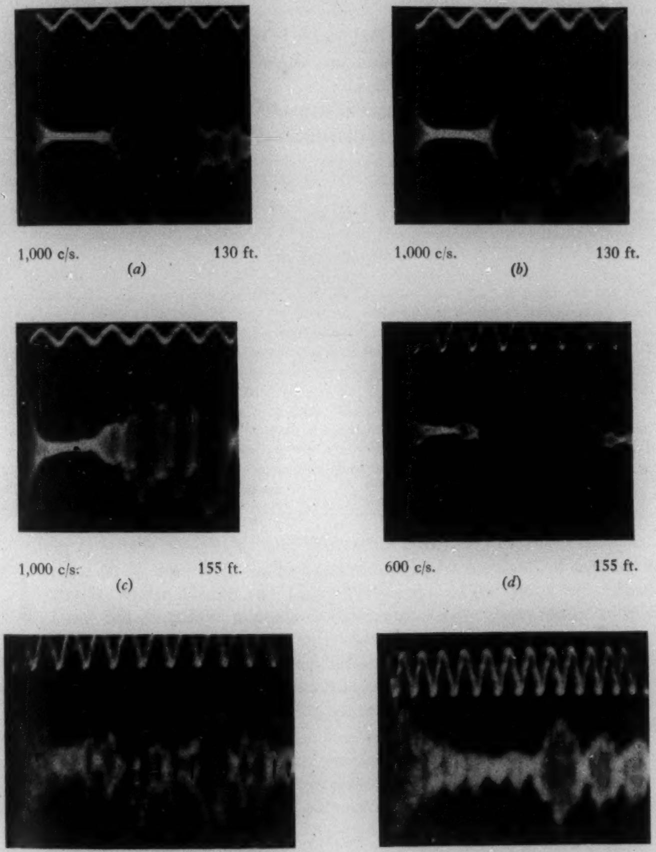

1,000 c/s. 130 ft.
(*a*)

1,000 c/s. 130 ft.
(*b*)

1,000 c/s. 155 ft.
(*c*)

600 c/s. 155 ft.
(*d*)

600 c/s. 450 ft.
(*e*)

300 c/s. 450 ft.
(*f*)

Figure 6. Vibrations recorded at various frequencies and distances.